

The Pennsylvania State University

The Graduate School

College of Engineering

**UNDERSTANDING LITHIUM PLATING IN LITHIUM-ION BATTERIES AND
EXPLORING MITIGATION STRATEGIES BY SELF-HEATING**

A Dissertation in

Chemical Engineering

by

Daniel R. Marple

© 2017 Daniel R. Marple

Submitted in Partial Fulfillment
of the Requirements
for the Degree of

Doctor of Philosophy

December 2017

The dissertation of Daniel R. Marple was reviewed and approved* by the following:

Chao-Yang Wang
Professor and Diefenderfer Chair of Mechanical and Nuclear Engineering,
Chemical Engineering
Dissertation Advisor
Chair of Committee

Michael J. Janik
Professor and Chair of Brennan Clean Energy Early Career Professorship in
Chemical Engineering

Enrique D. Gomez
Associate Professor of Chemical Engineering

Christopher D. Rahn
Associate Dean for Innovation and Professor of Mechanical and Nuclear
Engineering

Kristen Fichthorn
Merrell Fenske Professor of Chemical Engineering
Ph.D. Program Coordinator

*Signatures are on file in the Graduate School

ABSTRACT

The integration of lithium ion batteries into the electric vehicle market is dependent on a few key issues. Two of these issues include cycle life and performance at low temperatures. Industrial lithium-ion batteries need to be able to withstand several thousand cycles and operate over a large temperature range so as not to induce range anxiety in drivers in colder climates. One of the major degradation mechanisms that can occur within a battery, especially in cold temperatures, is lithium plating on the graphite anode. Experiments in this dissertation show that the degradation mechanism of $\text{LiNi}_{0.6}\text{Mn}_{0.2}\text{Co}_{0.2}\text{O}_2$ /graphite high energy cells that causes a premature death is lithium plating.

Experiments utilizing specially fabricated research-type cells with forced lithium plating are used to better understand the important variables that drive lithium plating in graphite anodes. Results show that temperature plays a dominant role in the onset of lithium plating, which can even occur at temperatures above 0 °C. In order to mitigate lithium plating in Li-ion batteries, the internal temperature of the battery must be monitored and controlled. This can be obtained through self-heating quickly and efficiently while using a minimal amount of energy. Pulse heating of batteries from 0 °C is examined in order to decrease spatial temperature gradients, lower average activation current and minimize wasted energy due to temperature overshoot when compared to the current continuous heating protocol. The optimal pulse heating protocol is a 2 second on-pulse followed by a 2 second off-pulse. Mitigation of lithium plating in industrial electric vehicle batteries is attempted utilizing the self-heating technology. External heating is

unable to heat the battery from sub-zero temperatures while inducing a safety shut-off and large spatial temperature gradients. Conversely, internal heating is successful at heating the cell quickly and uniformly with minimal energy consumed.

TABLE OF CONTENTS

List of Figures	vii
List of Tables	xi
Acknowledgements.....	xii
Chapter 1 Introduction	1
1.1 Motivation.....	1
1.2 Background Literature	2
1.2.1 Aging Mechanisms.....	2
1.2.2. Low Temperature Performance of Lithium-Ion Batteries	7
1.3 References.....	8
Chapter 2 Electrochemical Cycle-Life Characterization of High Energy Lithium-ion Cells with Thick $\text{Li}(\text{Ni}_{0.6}\text{Mn}_{0.2}\text{Co}_{0.2})\text{O}_2$ and Graphite Electrodes.....	14
2.1 Introduction.....	14
2.2 Experimental	17
2.2.1 Cell Fabrication	17
2.2.2 Initial Screening	17
2.2.3 Cycle Aging Tests	18
2.2.4 Diagnostic Tests	19
2.3 Results and Discussion.....	21
2.3.1 Beginning-of-Life (BOL) Performance.....	21
2.3.2 Capacity Fade	26
2.3.4 Power Fade	29
2.3.5 Performance Fade at Low Temperature	38
2.3.6 A Comparison of Cell Performance Measured in Three- vs. Two- Electrode Cells	48
2.4 Conclusions.....	51
2.5 References.....	51
Chapter 3 Utilizing Research-Type Lithium-Ion Batteries to Gain a Better Understanding of Lithium Plating	55
3.1 Motivation.....	55
3.2 Introduction.....	55
3.3 Experimental Methods	57
3.3.1 Development of Pouch Cells.....	57
3.3.2 Development of Diagnostic Tools.....	59
3.4 Results and Discussion.....	62
3.5 Conclusions.....	70
3.6 References.....	71

Chapter 4 Pulse Self-Heating of a Self-Heating Lithium-Ion Battery	74
4.1 Motivation.....	74
4.2 Introduction.....	75
4.3 Experimental	76
4.4 Results and Discussion.....	79
4.5 Conclusions.....	89
4.6 References.....	90
Chapter 5 External vs. Internal Heating for Large-Format Automotive Lithium-Ion Batteries	92
5.1 Motivation.....	92
5.2 Introduction.....	93
5.3 Experimental	94
5.3.1 Fabrication of Pouch Cells	94
5.3.2 Experimental Set-up.....	94
5.3.3 Experimental Testing Protocol.....	96
5.4 Results and Discussion.....	97
5.5 Conclusions.....	110
5.6 References.....	110
Chapter 6 Conclusions and Future Work.....	112
6.1 Conclusions.....	112
6.2 Future Work	116
6.2.1 Further Diagnostic Studies for Understanding Lithium Plating.....	116
6.2.2 Mitigating Lithium Deposition.....	117

LIST OF FIGURES

- Figure 2-1. Beginning-of-Life (BOL) performance of a high energy NMC622/graphite cell with 200 Wh/kg: (a) discharge performance under different C-rate at room temperature ($\sim 23^{\circ}\text{C}$); (b) temperature effect on 1C discharge performance; (c) separation of positive and negative electrode potentials from full cell voltage in a three-electrode cell during 1C charge-C/3 discharge process at 25°C (Note: Capacity is normalized based on the C/3 discharge capacity measured in a three-electrode cell: 3.17 Ah); (d) separation of positive and negative electrode impedance from whole cell impedance in a 3-electrode cell at 25°C (Note: impedance has been normalized based on total positive electrode area of 1055 cm^2).24
- Figure 2-2. Effect of C-rate on (a) full cell voltage, (b) positive and (c) negative electrode potentials during 1C charge-C/3 discharge process for a fresh high energy NMC622/graphite cell at 25°C . (Note: Capacity is normalized based on the C/3 discharge capacity of 3.17 Ah measured in a three-electrode cell).25
- Figure 2-3. (a) 1C charge and C/3 discharge curves of aged cells (Note: Capacity is normalized based on the C/3 discharge capacity of 3.20 Ah for a fresh cell), and (b) C/3 capacity retention at room temperature ($\sim 23^{\circ}\text{C}$) as a function of cycle number for high energy NMC622/graphite cells. For a comparison, C/3 capacity retention at room temperature as a function of cycle number for high energy NMC111/graphite cells with similar electrode thickness, loading and cell size fabricated with the same procedure is also shown in Figure 2-3b.28
- Figure 2-4. 1C charge/1C discharge performance of aged cells measured in (a) a two-electrode cell at room temperature ($\sim 23^{\circ}\text{C}$) and (b, c, d) a three-electrode cell at 25°C . In three-electrode diagnostic test, (b) full cell voltage, (c) positive and (d) negative electrode potentials as a function of discharge capacity were measured simultaneously during the discharge process.33
- Figure 2-5. (a) Cell impedance of a fresh and selected aged cells measured at 90% SOC and room temperature using two-electrode cell (symbols: experimental data, lines: fitted), (b) An equivalent circuit used for fitting cell impedance spectra shown in Figure 2-5a (Note: Warburg diffusion impedance showing a inclined line in the low frequency range isn't included in the equivalent circuit), (c) Evolution of resistances related to different processes as a function of cycle number at room temperature for high energy NMC622/graphite cells. (Note: impedance has been normalized based on total positive electrode area of 1055 cm^2).35
- Figure 2-6. A comparison of (a) full cell, (b) positive electrode and (c) negative electrode impedance measured at 80% SOC and 25°C (symbols: experimental data, lines: fitted) in a 3-electrode cell among a fresh and two aged cells at 904 and 1500 cycles....36
- Figure 2-7. A comparison in the resistances related to different processes at 25°C between full cell (solid line + solid symbol) and positive electrode (dash line + open symbol) fitted from the impedance test data shown in Figure 2-6. (Note: impedance has been normalized based on total positive electrode area of 1055 cm^2).37

Figure 2-8. 1C charge curves at 25 °C and 1C discharge curves at required ambient temperature (a) 0 °C and (b) -10 °C, of aged cells, and (c) 1C discharge capacity as a function of cycle number at four different temperatures in the range from 40 to -10 °C for high energy NMC622/graphite cells.	41
Figure 2-9. A comparison of (a) full cell, (b) positive electrode, and (c) negative electrode impedance measured at 80% SOC and -10 °C (symbols: experimental data, lines: fitted) in a three-electrode cell among a fresh and two aged cells at 904 and 1500 cycles.....	42
Figure 2-10. Equivalent circuits for (a) cell and positive electrode, and (b) negative electrode used to fit cell impedance spectra shown in Figure 2-9. (Note: Warburg diffusion impedance showing a short inclined line in the low frequency range isn't included in the equivalent circuits).	43
Figure 2-11. A comparison in the resistances related to different processes at -10 °C between full cell (solid line + solid symbol) and positive electrode (dash line + open symbol) fitted from the impedance test data shown in Figure 2-9. (Note: impedance has been normalized based on total positive electrode area of 1055 cm ²).	46
Figure 2-12. A comparison in 1C charge-C/3 discharge performance of fresh and aged cells measured at room temperature (~23 °C) between in three-electrode (3E) (solid lines) and two-electrode (2E) (dash lines) cells.	50
Figure 3-1. Comparison of baseline and research-type cells voltage-capacity C/3 discharge curves at RT showing (a) initial high voltage plateau and subsequent voltage drop for Res cells and (b) stripping of plated lithium allowing for “extra” capacity above nominal capacity for Res cells.....	65
Figure 3-2. Results of three-electrode calibration for HE cells showing potentials of each electrode [26].	66
Figure 3-3. Discharge curves for first 5 cycles (2C discharge) for Res622 cells at (a) 5 °C, (b) 15 °C and (c) 35 °C.	67
Figure 3-4. Coulombic efficiencies of baseline (RT) and Res cells for the first 5 discharge cycles during aging tests at various temperatures.	68
Figure 3-5. The effect of temperature on the aging of Res cells cycled at various temperatures.	69
Figure 4-1. Working principle of a SHLB showing the cell structure including the embedded nickel foil and activation terminal [3].....	75
Figure 4-2. Electrical circuit showing the working principle of a self-heating lithium-ion battery.....	77
Figure 4-3. Performance of the continuous heating protocol showing (a) measured cell voltage and current (negative value means discharge) and (b) surface temperature	

measured by thermocouple and foil temperature measured by Ni foil as a resistance-temperature detector (RTD).	79
Figure 4-4. Measured activation current during self-heating comparing continuous heating and pulse heating cases (a) 1:1, (b) 1:2, (c) 2:1, (d) 2:2, (e) 2:3 and (f) 2:4.	81
Figure 4-5. Average current measured for 2 second on time tests showing average activation current during on-pulses only (black) and over the duration of the test (red).	82
Figure 4-6. Measured cell voltage during self-heating comparing continuous heating and pulse heating cases (a) 1:1, (b) 1:2, (c) 2:1, (d) 2:2, (e) 2:3 and (f) 2:4.	83
Figure 4-7. Evolution of surface and foil temperature during pulse self-heating cases (a) 1:1, (b) 1:2, (c) 2:1, (d) 2:2, (e) 2:3 and (f) 2:4.	85
Figure 4-8. Evolution of surface temperature comparing continuous heating and pulse self-heating protocols.	87
Figure 4-9. Effect of pulse rest time on (a) maximum foil temperature and (b) maximum spatial temperature gradient.	88
Figure 4-10. Self-heating time and capacity consumption for continuous and pulse self-heating.	89
Figure 5-1. Working principle of external and internal heating of a Li-ion battery. (a) Schematic of Ni foil location for external heating (arrows indicate heat flow), (b) Schematic of Ni foil location for internal heating using a self-heating Li-ion battery (arrows indicate heat flow) (c) Schematic of the experimental set-up using two 10 Ah Li-ion cells and symmetry to model a 40 Ah automotive cell.	95
Figure 5-2. Temperature evolution using thermocouples during heating for external heating from (a) -10 °C, (b) -20 °C, (c) -30 °C (d) -40 °C and internal heating from (e) -10 °C, (f) -20 °C, (g) -30 °C (h) -40 °C.	98
Figure 5-3. Spatial temperature evolution during external heating from (a) -10 °C, (b) -20 °C, (c) -30 °C and (d) -40 °C and internal heating from (e) -10 °C, (f) -20 °C, (g) -30 °C and (h) -40 °C.	101
Figure 5-4. . Effect of ambient temperature on (a) Temperatures at the end of heating for TC1 (red), TC2 (black) and TC3 (blue) for external (square data points) and internal (circle data points) heating and (b) Heating time and percentage of capacity consumed (in red).	102
Figure 5-5. Activation current during heating for (a) -10 °C, (c) -20 °C, (e) -30 °C and (g) -40 °C and individual cell activation currents (internal heating in black, external heating in red, cell 1 solid line, cell 2 dashed line) for (b) -10 °C, (d) -20 °C, (f) -30 °C and (h) -40 °C.	104

Figure 5-6. Measured cell voltage (V_{cell}) and estimated open circuit voltage (V_{oc}) for heating from (a) -10°C and (b) -40°C 105

Figure 5-7. Breakdown of heating power from the nickel foil and electrochemical reactions during internal heating from (a) -10°C , (c) -20°C , (e) -30°C and (g) -40°C and external heating from (b) -10°C , (d) -20°C , (f) -30°C and (h) -40°C 108

Figure 5-8. Breakdown of resistance from the nickel foil and electrochemical reactions during internal heating from (a) -10°C , (c) -20°C , (e) -30°C and (g) -40°C and external heating from (b) -10°C , (d) -20°C , (f) -30°C and (h) -40°C 109

LIST OF TABLES

Table 1-1. Main degradation processes of Li-ion batteries. [27]	5
Table 2-1. Average full cell voltage, positive and negative electrode potentials measured by a 3-electrode cell during 1C discharge of fresh and aged high energy NMC622/graphite cells at 25 °C.	33
Table 2-2. . Fitting parameter values for the impedance spectra (excluding diffusion line part) of a fresh and selected aged cells measured under 90% SOC at room temperature using two-electrode configuration shown in Figure 2-5a.....	34
Table 2-3. Fitting parameter values for the impedance spectra (excluding Warburg diffusion impedance) of a fresh and two aged cells (at 904 and 1500 cycles) measured at 80% SOC and room temperature in a three-electrode cell shown in Figures 2-6a and 6b.....	37
Table 2-4. Fitting parameter values for the impedance spectra (excluding Warburg diffusion impedance) of a fresh and two aged cells (at 904 and 1500 cycles) measured at 80% SOC and -10 °C in a three-electrode cell shown in Figure 2-9.	47
Table 3-1. The temperature can have a drastic effect on the cycle life of a lithium-ion battery.....	70

ACKNOWLEDGEMENTS

I would like to thank my advisor Dr. Chao-Yang Wang for giving me the opportunity to work under him and learn from him during my time in graduate school. His passion, knowledge, creativity, and enthusiasm for research and in particular, batteries, is inspiring and has allowed me to learn an unmeasurable amount and grow as a researcher. I appreciate everything he has done for me.

I would also like to thank my family for their never-ending support, from my grandparents and parents being there for me from day 1 and only wanting the best for me, to my wife, Kim, and son, Collin, for showing amazing patience and understanding as I pursued this continuing higher education. I would not have been able to come back to school without their continuing love and support.

Finally, I would like to thank all of my peers that have been there along the way. Special thanks go to Yongjun, Guangsheng and Xiao-Guang for their words of wisdom and discussion pertaining to my work. Each one was instrumental in helping me along the way. Thanks to the many members of the ECEC group including Shanhai, Yan, Wei, Tanvir, Gang, and Liang for all the support in the modeling group in USB and the friendships built over many lunches together. Thanks to Paul, Kam, Yubai, Teng, Jinyong, Lei and Mansu for comparing of notes and being there for each other as we go through this experience together. Also, thanks to my chemical engineering peers Maggie, Ian, Nick, Sneha, Mike and Charles for being there for me and for all the great times we had together outside of the lab. You have helped make my time here amazing as we gain friendships that will last a lifetime.

Chapter 1

Introduction

1.1 Motivation

Aging of lithium ion batteries is the typical restriction when expecting a 10+ year lifespan for the long life requirement of electric vehicle applications. Typical aging of the batteries includes loss of active material, loss of capacity, reduction of power and increasing of cell impedance. The formation and growth of the solid-electrolyte interface (SEI) is widely recognized as the dominant aging mechanism [1-7] though several other mechanisms have been explored in literature including loss of active material from the electrical network due to cracking and mechanical failure [8-10], loss of active material through dissolution of transition metals from the cathode [11-13], and deposition of metallic lithium on the graphite anode [14-16]. In order to be utilized in electric vehicles, a reliable life-prediction must be available for the battery managements system, which requires a fundamental understanding of these aging mechanisms.

Other concerns of the limitations of lithium ion batteries include poor low temperature performance and fast charging capability [17]. Lithium ion batteries suffer severe power loss at sub-zero temperatures. This poor performance is believed to be due to poor electrolyte conductivity, slow Li diffusion, increased resistance of the SEI, and increased resistance to the kinetics of charge transfer. Previous efforts to improve the performance at low temperatures include electrolyte additives [18-21], which usually have detrimental effects on cycle life and performance at high temperature, and on heating of the cell prior to use [22, 23]. Previous efforts to heat cells tend to have issues with long heating time, high energy consumption and low heating efficiency. In order to have widespread vehicle electrification, fast charging needs to obtainable

quickly (in minutes) and in all weather conditions. Current lithium ion batteries are unable to charge at sub-zero temperatures due to the propensity for lithium plating to occur [18, 20, 24-26]. Reduced intercalation kinetics of the anode leads to competition between lithium intercalation and lithium plating on the graphite particle. Being able to control the internal temperature of the battery would allow for increased cell performance and ability to fast charge while in sub-zero ambient conditions.

1.2 Background Literature

1.2.1 Aging Mechanisms

Inevitably, lithium ion batteries will not be able to last forever due to degradation processes that occur inside the cell. Identifying the major degradation processes is key to understanding what factors play dominant roles in the cycle life decay of lithium ion batteries and key to any attempt to extend the life and usefulness of these cells. Arora et al. presented an early review of degradation processes for lithium ion batteries. Table 1-I [27] shows a summary of the many degradation processes that may occur in these cells [3, 28]. In general, capacity loss is due to either consumption or isolation from the cycle network, which is mostly attributed to the loss of active lithium at the negative anode. Power fade, which is caused by impedance growth due to growth of solid layers depositing on the surface of the electrodes, results in increased internal resistance. Impedance growth can have contributions from both electrodes though it is usually a result of the positive electrode [29].

During the first several charge-discharge cycles of a fresh Li-ion cell, a passive SEI film forms due to the irreversible reaction between lithium ions and solvent at the surface of the carbon anode [30-32]. The SEI has been studied extensively in literature [4-7, 30, 31, 33-48].

This process consumes active lithium in the electrolyte; however, ideally, if a stable, protective SEI film is formed, the electrode material is isolated from the electrolyte, reducing the chance of further electrolyte reduction. The SEI also prevents self-discharge. Self-discharge can occur in one of two ways; deintercalation of Li-ions from the anode material or dissolution of the SEI and consequential reformation of the SEI layer. If SEI formation were sustained throughout battery operation, it would render Li-ion batteries unusable due to the continual loss of cyclable lithium. The reason that Li-ion batteries can operate is that the SEI does not conduct electrons well, and is almost impenetrable to electrolyte molecules. Once an initial SEI layer has formed, the inability of electrolyte molecules to travel through the SEI to the active material surface, where they could react with lithium ions and electrons, inhibits further SEI growth. Intercalation is inhibited far less, because lithium ions can easily pass through the SEI. Thus the battery is able to experience many charge-discharge cycles with little additional SEI buildup.

An ideal SEI film should have several features. The SEI needs to be stable both electrochemically and thermally. If small changes in temperature or potential causes the SEI to change or break apart, then open anode material site would allow for further solvent reduction and thus more capacity loss. The SEI also needs to be stable from a solubility perspective. If the SEI components formed are soluble in the electrolyte of the battery, then further reaction will proceed as well. Secondly, the SEI formation needs to be fast. Fast formation allows for less time for exposure of the lithiated anode to the electrolyte. An ideal SEI film should also permit free Li^+ transport. It is essential that the battery can still operate with Li^+ diffusing through the SEI but not electrolyte molecules. The SEI should have limitations on its electronic conductivity as well. A good SEI should not conduct electrons well, but cannot be such an insulator that it completely disconnects the anode material from the conducting matrix. Furthermore, it should be able to withstand the volume change due to Li^+ intercalation-deintercalation between the anode layers. Intercalation-deintercalation processes can cause volume changes up to 400% (silicon

anodes). The SEI needs to be able to withstand these changes to prevent cracking and thus exposure of active material surface. The transference number for unsolvated Li-ion may not be unity, and other charged and neutral species may be allowed to diffuse through, causing further film growth and irreversible capacity loss during subsequent cycling [3].

During the charge and discharge of a Li-ion cell the active Li in the cell is intercalated into and out of the negative electrode, respectively. During each cycle a small amount of that active Li reacts to thicken a passivating layer on the surface of the electrode. The exact nature of the SEI is dependent on a number of factors such as the active material in the electrodes, electrolyte composition, temperature of the cell, electrolyte additives, etc. Although the SEI can differ dramatically depending on the parameters of the cell, the Li used to form the SEI is always consumed irreversibly. Thus in order for an electrolyte molecule to react with a lithium ion, Li^+ , and an electron, e^- , it will have to come close enough to the Li_xC_6 to be within a tunneling range of an e^- . This presumably requires an electrolyte molecule to diffuse through the SEI to get within a required range, significantly reducing the SEI growth rate as the SEI thickens [34].

Huang et al. performed a study on how different formation conditions affected the aging performance of Li-ion cells [35]. Cells were fabricated then initial SEI formation was carried out at three different formation conditions, varying temperature and charge rate. The cells were then stored for 10 weeks at 60 °C conditions. The results showed comparable reversible capacities for all three groups, but showed a considerable difference in irreversible capacity loss. Cell resistances were also measured in this study. It was seen that both the bulk and film resistances for group C were higher than for those in Groups A and B, while the charge transfer resistances were similar for all groups. After storage, the cells were cycled for 300 cycles. Group A and B both retained around 96-97% of the original capacity while Group C retained only 89% of its capacity. From this study, it can be concluded that formation conditions for the SEI do have

consequences on the performance of the cell. Specifically, it seems higher formation temperature and lower formation charge currents are better for the initial formation of the SEI.

The effects of SEI porosity were modeled by Safari et al. [36]. The results of this study show that an SEI with a higher porosity will have higher capacity losses than those with a lower porosity. Upon storage for 300 days, the 1% porosity SEI cell retains over 90% of its SOC, while the 10% porosity SEI cell retains only 70% of its SOC. An ideal SEI would not let any electrolyte molecules diffuse through it, which is more likely to happen with a higher porosity.

As temperature decreases, approaching 0 °C and below, a different aging mechanism becomes dominant [15]. The mechanism believed to be dominant at sub-zero temperatures is lithium deposition on the surface of the graphite anode. Lithium plating can occur when the cell is charged at low temperature, using high currents, or overcharging [14-16, 18, 25, 26, 49-66]. The lithium involved in this may be lost due to its high reactivity with the electrolyte solvent and salt molecules. This reaction can produce Li_2CO_3 , LiF and other useless compounds, accelerating aging and deteriorating safety [67, 68]. Lithium plating will be discussed further in the introduction of Chapter 3.

Table 1-1. Main degradation processes of Li-ion batteries. [27]

<i>Degradation process</i>	<i>Consequences</i>	<i>Enhanced by</i>	<i>Typical reactions</i>
Negative electrode			
SEI forms due to electrolyte reduction during first few cycles	Irreversible capacity loss; Gas generation		$\text{PC} + 2e^- \rightarrow \text{propylene} + \text{CO}_3^{2-}$ [69] $\text{EC} + 2e^- \rightarrow \text{ethylene} + \text{CO}_3^{2-}$ *
Continuous electrolyte decomposition	Capacity fade (loss of lithium);	High temperatures; High SOC	$\text{EC} + 2e^- + 2\text{Li}^+ \rightarrow \text{LiCH}_2\text{CH}_2\text{OCO}_2\text{Li} \downarrow$ [30, 70]

Impedance growth			
Lithium deposition	Capacity fade; Impedance growth	Overcharge; High charge rate	$\text{Li}^+ + \text{e}^- = \text{Li(s)} [67]$
Positive electrode			
Structural disordering; Phase transitions	Capacity fade		$\text{LiNiO}_2 \leftrightarrow \{\text{Li}_{1-x}\text{Ni(II)}_{x/2}\}\text{Ni(III)}_{1-x}\text{O}_{2-x}$
			$+ \frac{x}{2}\text{Li}_2\text{O} + \frac{x}{4}\text{O}_2 [3]$
Surface film formation	Capacity fade; Impedance growth		
Others			
Electrolyte oxidation at positive electrode	Capacity fade; Impedance growth	Overcharge High temperature	solvent \rightarrow oxidized products (gases, solution, and solid species) + $\text{ne}^- [28]$
Self-discharge on positive oxidized electrode	Reversible and irreversible capacity loss	High temperature	$\text{El} \rightarrow \text{e}^- + \text{El}^+$ $y\text{Li}^+ + y\text{e}^- + \text{MO}_z \rightarrow \text{Li}_y\text{MO}_z [32]$
Current collector degradation	Capacity fade; Impedance growth	Overdischarge	

* PC = Propylene carbonate; EC = Ethylene carbonate.

1.2.2. Low Temperature Performance of Lithium-Ion Batteries

Lithium ion batteries suffer from poor performance at low temperature [24, 71-75]. This is associated with poor electrolyte conductivity, slow Li diffusion, increased resistance of the SEI, and increased resistance to the kinetics of charge transfer [76]. One strategy to combat this is to alter the internal chemistry of the battery via electrolyte composition [18, 77-80], electrolyte additives [18-21, 63], or increasing interfacial area by using electrode materials with different morphologies [81]. These strategies can work to improve low temperature performance but at the cost of high temperature performance and cycle life. Also, these only address the electrolyte related issues but do not mitigate solid-state diffusion in the electrodes.

In order to improve the low temperature performance, pre-heating of the cell has been explored. For most electric vehicles, there are two sources of heat: waste heat from the powertrain including motors, inverters and batteries or external resistive heaters [82]. This lends two strategies possible, internal heating via battery resistance or external heating through some fluid or resistors.

Internal strategies that have been evaluated consist of internal mutual pulse heating [23], internal resistive heating [23], internal heating with frequency based on polarization voltage [83], and core heating with alternating currents (AC) [22, 23, 84-86]. External heating strategies include using air, liquid or phase change materials for external convective heating [23, 82, 84] or external AC heating [22, 23]. Of these methods, it was found that for internal heating, convective heating was the quickest while mutual pulse heating consumed the lowest energy while providing uniform heating. For the external methods, AC heating was able to provide uniform heating and could utilize an external power source if available. These heating methods tend to be time and energy consuming and can require complicated heating circuits, reducing the energy density of the battery [22, 23, 84]. Recent work by Wang et al. has developed a novel internal heating

strategy utilizing a nickel foil embedded in the cell which acts as a resistive heater [87-91]. As shown in [87], heating from -20 to 0 °C requires only 20 seconds and consuming 3.8% of the battery's capacity. It was shown that this new technology provides excellent reliability and durability as these cells lasted 500 cycles at -30 °C, 2500 cycles at 25 °C, and 1000 cycles at 45 °C.

1.3 References

1. Liu, P., et al., *Aging Mechanisms of LiFePO₄ Batteries Deduced by Electrochemical and Structural Analyses*. Journal of the Electrochemical Society, 2010. **157**(4): p. A499-A507.
2. Barre, A., et al., *A review on lithium-ion battery ageing mechanisms and estimations for automotive applications*. Journal of Power Sources, 2013. **241**: p. 680-689.
3. Vetter, J., et al., *Ageing mechanisms in lithium-ion batteries*. Journal of Power Sources, 2005. **147**(1-2): p. 269-281.
4. Dubarry, M. and B.Y. Liaw, *Identify capacity fading mechanism in a commercial LiFePO₄ cell*. Journal of Power Sources, 2009. **194**(1): p. 541-549.
5. Dubarry, M., C. Truchot, and B.Y. Liaw, *Cell degradation in commercial LiFePO₄ cells with high-power and high-energy designs*. Journal of Power Sources, 2014. **258**: p. 408-419.
6. Wang, J., et al., *Degradation of lithium ion batteries employing graphite negatives and nickel-cobalt-manganese oxide plus spinel manganese oxide positives: Part 1, aging mechanisms and life estimation*. Journal of Power Sources, 2014. **269**: p. 937-948.
7. Yoshida, T., et al., *Degradation mechanism and life prediction of lithium-ion batteries*. Journal of the Electrochemical Society, 2006. **153**(3): p. A576-A582.
8. Yang, X.G., C. Bauer, and C.Y. Wang, *Sinusoidal current and stress evolutions in lithium-ion batteries*. Journal of Power Sources, 2016. **327**: p. 414-422.
9. Woodford, W.H., Y.M. Chiang, and W.C. Carter, *"Electrochemical Shock" of Intercalation Electrodes: A Fracture Mechanics Analysis*. Journal of the Electrochemical Society, 2010. **157**(10): p. A1052-A1059.
10. Zhang, J.Q., et al., *Diffusion induced stress in layered Li-ion battery electrode plates*. Journal of Power Sources, 2012. **209**: p. 220-227.
11. Zhang, Y.C. and C.Y. Wang, *Cycle-Life Characterization of Automotive Lithium-Ion Batteries with LiNiO₂ Cathode*. Journal of the Electrochemical Society, 2009. **156**(7): p. A527-A535.

12. Zhan, C., et al., *Mn(II) deposition on anodes and its effects on capacity fade in spinel lithium manganate-carbon systems*. Nature Communications, 2013. **4**.
13. Lu, J., et al., *Effectively suppressing dissolution of manganese from spinel lithium manganate via a nanoscale surface-doping approach*. Nature Communications, 2014. **5**.
14. Petzl, M., M. Kasper, and M.A. Danzer, *Lithium plating in a commercial lithium-ion battery A low-temperature aging study*. Journal of Power Sources, 2015. **275**: p. 799-807.
15. Waldmann, T., et al., *Temperature dependent ageing mechanisms in Lithium-ion batteries - A Post-Mortem study*. Journal of Power Sources, 2014. **262**: p. 129-135.
16. Li, Z., et al., *A review of lithium deposition in lithium-ion and lithium metal secondary batteries*. Journal of Power Sources, 2014. **254**: p. 168-182.
17. Gallagher, K.G., et al., *Optimizing Areal Capacities through Understanding the Limitations of Lithium-Ion Electrodes*. Journal of the Electrochemical Society, 2016. **163**(2): p. A138-A149.
18. Smart, M.C., et al., *Electrochemical performance and kinetics of $\text{Li}_{1+x}(\text{Co}_{1/3}\text{Ni}_{1/3}\text{Mn}_{1/3})(1-x)\text{O}_2$ cathodes and graphite anodes in low-temperature electrolytes*. Journal of Power Sources, 2007. **168**(2): p. 501-508.
19. Xu, K., *Electrolytes and Interphases in Li-Ion Batteries and Beyond*. Chemical Reviews, 2014. **114**(23): p. 11503-11618.
20. Zhang, S.S., K. Xu, and T.R. Jow, *A new approach toward improved low temperature performance of Li-ion battery*. Electrochemistry Communications, 2002. **4**(11): p. 928-932.
21. Yaakov, D., et al., *On the Study of Electrolyte Solutions for Li-Ion Batteries That Can Work Over a Wide Temperature Range*. Journal of the Electrochemical Society, 2010. **157**(12): p. A1383-A1391.
22. Stuart, T.A. and A. Hande, *HEV battery heating using AC currents*. Journal of Power Sources, 2004. **129**(2): p. 368-378.
23. Ji, Y. and C.Y. Wang, *Heating strategies for Li-ion batteries operated from subzero temperatures*. Electrochimica Acta, 2013. **107**: p. 664-674.
24. Ji, Y., Y.C. Zhang, and C.Y. Wang, *Li-Ion Cell Operation at Low Temperatures*. Journal of the Electrochemical Society, 2013. **160**(4): p. A636-A649.
25. Orsini, F., et al., *In situ Scanning Electron Microscopy (SEM) observation of interfaces within plastic lithium batteries*. Journal of Power Sources, 1998. **76**(1): p. 19-29.
26. Fan, J. and S. Tan, *Studies on charging lithium-ion cells at low temperatures*. Journal of the Electrochemical Society, 2006. **153**(6): p. A1081-A1092.
27. Wang, C.Y.F., W.; Marple, D.; Ji, Y.; Shaffer, C.E.; Sinha, P.K., *Li-Ion Battery Degradation Modeling: A Review*. 2013, Electrochemical Engine Center.
28. Arora, P., R.E. White, and M. Doyle, *Capacity fade mechanisms and side reactions in lithium-ion batteries*. Journal of the Electrochemical Society, 1998. **145**(10): p. 3647-3667.

29. Dey, A.N. and B.P. Sullivan, *Electrochemical Decomposition of Propylene Carbonate on Graphite*. Journal of the Electrochemical Society, 1970. **117**(2): p. 222-&.
30. Ramasamy, R.P., J.W. Lee, and B.N. Popov, *Simulation of capacity loss in carbon electrode for lithium-ion cells during storage*. Journal of Power Sources, 2007. **166**(1): p. 266-272.
31. Fong, R., U. Vonsacken, and J.R. Dahn, *Studies of Lithium Intercalation into Carbons Using Nonaqueous Electrochemical-Cells*. Journal of the Electrochemical Society, 1990. **137**(7): p. 2009-2013.
32. Guyomard, D. and J.M. Tarascon, *High-Voltage Stable Liquid Electrolytes for $\text{LiI}+\text{Xmn}_2\text{O}_4/\text{Carbon}$ Rocking-Chair Lithium Batteries*. Journal of Power Sources, 1995. **54**(1): p. 92-98.
33. Pinson, M.B. and M.Z. Bazant, *Theory of SEI Formation in Rechargeable Batteries: Capacity Fade, Accelerated Aging and Lifetime Prediction*. Journal of the Electrochemical Society, 2013. **160**(2): p. A243-A250.
34. Smith, A.J., et al., *Interpreting High Precision Coulometry Results on Li-ion Cells*. Journal of the Electrochemical Society, 2011. **158**(10): p. A1136-A1142.
35. Huang, C.H., et al., *The effect of solid electrolyte interface formation conditions on the aging performance of Li-ion cells*. Journal of Solid State Electrochemistry, 2011. **15**(9): p. 1987-1995.
36. Safari, M., et al., *Multimodal Physics-Based Aging Model for Life Prediction of Li-Ion Batteries*. Journal of the Electrochemical Society, 2009. **156**(3): p. A145-A153.
37. Peled, E., et al., *An advanced tool for the selection of electrolyte components for rechargeable lithium batteries*. Journal of the Electrochemical Society, 1998. **145**(10): p. 3482-3486.
38. Verma, P., P. Maire, and P. Novak, *A review of the features and analyses of the solid electrolyte interphase in Li-ion batteries*. Electrochimica Acta, 2010. **55**(22): p. 6332-6341.
39. Suthar, B., et al., *Effect of Porosity, Thickness and Tortuosity on Capacity Fade of Anode*. Journal of the Electrochemical Society, 2015. **162**(9): p. A1708-A1717.
40. Wang, H.Y. and F.M. Wang, *Electrochemical investigation of an artificial solid electrolyte interface for improving the cycle-ability of lithium ion batteries using an atomic layer deposition on a graphite electrode*. Journal of Power Sources, 2013. **233**: p. 1-5.
41. Park, I.J., T.H. Nam, and J.G. Kim, *Diphenyloctyl phosphate as a solid electrolyte interphase forming additive for Li-ion batteries*. Journal of Power Sources, 2013. **244**: p. 122-128.
42. Delacourt, C., et al., *Effect of Manganese Contamination on the Solid-Electrolyte-Interphase Properties in Li-Ion Batteries*. Journal of the Electrochemical Society, 2013. **160**(8): p. A1099-A1107.
43. Awarke, A., S. Pischinger, and J. Ogrzewalla, *Pseudo 3D Modeling and Analysis of the SEI Growth Distribution in Large Format Li-Ion Polymer Pouch Cells*. Journal of the Electrochemical Society, 2013. **160**(1): p. A172-A181.

44. Yeo, J.S., et al., *Solid electrolyte interphase formation behavior on well-defined carbon surfaces for Li-ion battery systems*. *Electrochimica Acta*, 2012. **77**: p. 111-120.
45. Kramer, E., et al., *SEI-forming mechanism of 1-Fluoropropane-2-one in lithium-ion batteries*. *Electrochimica Acta*, 2012. **81**: p. 161-165.
46. Colclasure, A.M., K.A. Smith, and R.J. Kee, *Modeling detailed chemistry and transport for solid-electrolyte-interface (SEI) films in Li-ion batteries*. *Electrochimica Acta*, 2011. **58**: p. 33-43.
47. Yan, J., et al., *A novel perspective on the formation of the solid electrolyte interphase on the graphite electrode for lithium-ion batteries*. *Electrochimica Acta*, 2010. **55**(5): p. 1785-1794.
48. Tasaki, K., et al., *Solubility of Lithium Salts Formed on the Lithium-Ion Battery Negative Electrode Surface in Organic Solvents*. *Journal of the Electrochemical Society*, 2009. **156**(12): p. A1019-A1027.
49. Liu, Q.Q., et al., *Effects of Electrolyte Additives and Solvents on Unwanted Lithium Plating in Lithium-Ion Cells*. *Journal of the Electrochemical Society*, 2017. **164**(6): p. A1173-A1183.
50. Bai, P., et al., *Transition of lithium growth mechanisms in liquid electrolytes*. *Energy & Environmental Science*, 2016. **9**(10): p. 3221-3229.
51. Waldmann, T., M. Kasper, and M. Wohlfahrt-Mehrens, *Optimization of Charging Strategy by Prevention of Lithium Deposition on Anodes in high-energy Lithium-ion Batteries - Electrochemical Experiments*. *Electrochimica Acta*, 2015. **178**: p. 525-532.
52. Love, C.T., O.A. Baturina, and K.E. Swider-Lyons, *Observation of Lithium Dendrites at Ambient Temperature and Below*. *Ecs Electrochemistry Letters*, 2015. **4**(2): p. A24-A27.
53. Kramer, Y., et al., *A New Method for Quantitative Marking of Deposited Lithium by Chemical Treatment on Graphite Anodes in Lithium-Ion Cells*. *Chemistry-a European Journal*, 2015. **21**(16): p. 6062-6065.
54. Fleischhammer, M., et al., *Interaction of cyclic ageing at high-rate and low temperatures and safety in lithium-ion batteries*. *Journal of Power Sources*, 2015. **274**: p. 432-439.
55. Birkenmaier, C., et al., *Lithium Plating on Graphite Negative Electrodes: Innovative Qualitative and Quantitative Investigation Methods*. *Journal of the Electrochemical Society*, 2015. **162**(14): p. A2646-A2650.
56. Akolkar, R., *Modeling dendrite growth during lithium electrodeposition at sub-ambient temperature*. *Journal of Power Sources*, 2014. **246**: p. 84-89.
57. Schmitz, R., et al., *SEI investigations on copper electrodes after lithium plating with Raman spectroscopy and mass spectrometry*. *Journal of Power Sources*, 2013. **233**: p. 110-114.
58. Downie, L.E., et al., *In Situ Detection of Lithium Plating on Graphite Electrodes by Electrochemical Calorimetry*. *Journal of the Electrochemical Society*, 2013. **160**(4): p. A588-A594.
59. Park, G., et al., *The study of electrochemical properties and lithium deposition of graphite at low temperature*. *Journal of Power Sources*, 2012. **199**: p. 293-299.

60. Lu, W.Q., et al., *Overcharge Effect on Morphology and Structure of Carbon Electrodes for Lithium-Ion Batteries*. Journal of the Electrochemical Society, 2012. **159**(5): p. A566-A570.
61. Smart, M.C. and B.V. Ratnakumar, *Effects of Electrolyte Composition on Lithium Plating in Lithium-Ion Cells*. Journal of the Electrochemical Society, 2011. **158**(4): p. A379-A389.
62. Gunawardhana, N., et al., *Suppression of lithium deposition at sub-zero temperatures on graphite by surface modification*. Electrochemistry Communications, 2011. **13**(10): p. 1116-1118.
63. Ratnakumar, B.V. and M.C. Smart, *Lithium Plating Behavior in Lithium-ion Cells*, in *Rechargeable Lithium-Ion Batteries*, M. Winter, et al., Editors. 2010, Electrochemical Soc Inc: Pennington. p. 241-252.
64. Eberman, K., et al., *Material and Design Options for Avoiding Lithium-Plating during Charging*, in *Battery/Energy Technology*, Z. Ogumi, N.J. Dudney, and S.R. Narayanan, Editors. 2010, Electrochemical Soc Inc: Pennington. p. 47-58.
65. Tang, M., P. Albertus, and J. Newman, *Two-Dimensional Modeling of Lithium Deposition during Cell Charging*. Journal of the Electrochemical Society, 2009. **156**(5): p. A390-A399.
66. Arora, P., M. Doyle, and R.E. White, *Mathematical modeling of the lithium deposition overcharge reaction in lithium-ion batteries using carbon-based negative electrodes*. Journal of the Electrochemical Society, 1999. **146**(10): p. 3543-3553.
67. Peled, E., *THE ELECTROCHEMICAL-BEHAVIOR OF ALKALI AND ALKALINE-EARTH METALS IN NON-AQUEOUS BATTERY SYSTEMS - THE SOLID ELECTROLYTE INTERPHASE MODEL*. Journal of the Electrochemical Society, 1979. **126**(12): p. 2047-2051.
68. Maleki, H., et al., *Thermal properties of lithium-ion battery and components*. Journal of the Electrochemical Society, 1999. **146**(3): p. 947-954.
69. Ning, G., R.E. White, and B.N. Popov, *A generalized cycle life model of rechargeable Li-ion batteries*. Electrochimica Acta, 2006. **51**(10): p. 2012-2022.
70. Ploehn, H.J., P. Ramadass, and R.E. White, *Solvent diffusion model for aging of lithium-ion battery cells*. Journal of the Electrochemical Society, 2004. **151**(3): p. A456-A462.
71. Lin, H.P., et al., *Low-temperature behavior of Li-ion cells*. Electrochemical and Solid State Letters, 2001. **4**(6): p. A71-A73.
72. Zhang, S.S., K. Xu, and T.R. Jow, *Low temperature performance of graphite electrode in Li-ion cells*. Electrochimica Acta, 2002. **48**(3): p. 241-246.
73. Zhang, S.S., K. Xu, and T.R. Jow, *The low temperature performance of Li-ion batteries*. Journal of Power Sources, 2003. **115**(1): p. 137-140.
74. Armand, M. and J.M. Tarascon, *Building better batteries*. Nature, 2008. **451**(7179): p. 652-657.
75. Etacheri, V., et al., *Challenges in the development of advanced Li-ion batteries: a review*. Energy & Environmental Science, 2011. **4**(9): p. 3243-3262.

76. Valoen, L.O. and J.N. Reimers, *Transport properties of LiPF₆-based Li-ion battery electrolytes*. Journal of the Electrochemical Society, 2005. **152**(5): p. A882-A891.
77. Smart, M.C., B.V. Ratnakumar, and S. Surampudi, *Electrolytes for low-temperature lithium batteries based on ternary mixtures of aliphatic carbonates*. Journal of the Electrochemical Society, 1999. **146**(2): p. 486-492.
78. Smart, M.C., B.V. Ratnakumar, and S. Surampudi, *Use of organic esters as cosolvents in electrolytes for lithium-ion batteries with improved low temperature performance*. Journal of the Electrochemical Society, 2002. **149**(4): p. A361-A370.
79. Smart, M.C., et al., *Lithium-Ion Electrolytes Containing Ester Cosolvents for Improved Low Temperature Performance*. Journal of the Electrochemical Society, 2010. **157**(12): p. A1361-A1374.
80. Ein-Eli, Y.T., S.R.; Chadha, R.; Blakley, T.J.; Koch, V.R., *Li-Ion Battery Electrolyte Formulated for Low-Temperature Applications*. Journal of the Electrochemical Society, 1997. **144**: p. 823-829.
81. Sides, C.R. and C.R. Martin, *Nanostructured electrodes and the low-temperature performance of Li-ion batteries*. Advanced Materials, 2005. **17**(1): p. 125-+.
82. Jaguemont, J., L. Boulon, and Y. Dube, *A comprehensive review of lithium-ion batteries used in hybrid and electric vehicles at cold temperatures*. Applied Energy, 2016. **164**: p. 99-114.
83. Ruan, H.J., et al., *A rapid low-temperature internal heating strategy with optimal frequency based on constant polarization voltage for lithium-ion batteries*. Applied Energy, 2016. **177**: p. 771-782.
84. Vlahinos, A.P., A.A., *Energy Efficient Battery Heating in Cold Climates*, in SAE Technical Paper. 2002.
85. Zhang, J.B., et al., *Internal heating of lithium-ion batteries using alternating current based on the heat generation model in frequency domain*. Journal of Power Sources, 2015. **273**: p. 1030-1037.
86. Zuniga, M., et al., *Heating Lithium-ion Batteries with Bidirectional Current Pulses*. 2015 Ieee Vehicle Power and Propulsion Conference (Vppc), 2015.
87. Wang, C.Y., et al., *Lithium-ion battery structure that self-heats at low temperatures*. Nature, 2016. **529**(7587): p. 515-8.
88. Yang, X.G., T. Liu, and C.Y. Wang, *Innovative heating of large-size automotive Li-ion cells*. Journal of Power Sources, 2017. **342**: p. 598-604.
89. Wang, C.Y., et al., *A Fast Rechargeable Lithium-Ion Battery at Subfreezing Temperatures*. Journal of the Electrochemical Society, 2016. **163**(9): p. A1944-A1950.
90. Yang, X.G., G.S. Zhang, and C.Y. Wang, *Computational design and refinement of self-heating lithium ion batteries*. Journal of Power Sources, 2016. **328**: p. 203-211.
91. Zhang, G.S., et al., *Rapid self-heating and internal temperature sensing of lithium-ion batteries at low temperatures*. Electrochimica Acta, 2016. **218**: p. 149-155.

Chapter 2

Electrochemical Cycle-Life Characterization of High Energy Lithium-ion Cells with Thick $\text{Li}(\text{Ni}_{0.6}\text{Mn}_{0.2}\text{Co}_{0.2})\text{O}_2$ and Graphite Electrodes

This chapter published as Y. Leng, S. Ge, D. Marple, X.G. Yang, C. Bauer, P. Lamp, and C.Y. Wang, "Electrochemical Cycle-Life Characterization of High Energy Lithium-ion Cells with Thick $\text{Li}(\text{Ni}_{0.6}\text{Mn}_{0.2}\text{Co}_{0.2})\text{O}_2$ and Graphite Electrodes," *Journal of the Electrochemical Society*, Vol. 164, pp. A1037-1049, 2017. YL and DM performed experimental studies and discussed contents, SG, DM and XGY fabricated the cells, YL drafted the manuscript and DM revised the manuscript.

2.1 Introduction

Li-ion batteries are considered one of the promising power systems for plug-in and pure electric vehicles (EV) due to their relatively high energy and high power densities.¹ In order to further increase the driving range of electric vehicles, it is desirable to improve the energy density of Li-ion batteries. There are two ways to improve the energy density of Li-ion batteries: improve and utilize high-capacity electrode materials, such as Ni-rich $\text{Li}(\text{Ni}_x\text{Mn}_y\text{Co}_z)\text{O}_2$ (NMC) ($x+y+z=1$, $x \geq 0.5$) layer oxides²⁻⁵ and Li-rich layered oxides^{6,7} used as positive electrode materials, Si-based composites^{4,6} and Li metal^{8,9} used as negative electrode materials; and increase the portion of active electrode materials contributing to the cell energy while minimizing the portion of non-active components, such as separators and current collecting foils, through optimization of cell design¹⁰⁻¹². In the latter category, high active material loading or thick electrode is a major direction. In the present paper, Li-ion batteries with thick graphite anodes and thick Ni-rich NMC cathodes will be explored for near-term EV batteries.

Cycle life is a major limitation for ultra-thick electrodes in high energy density batteries, among other concerns of power density, low temperature performance and fast-

charging capability.¹⁰ For EV applications, the battery should last for more than 10 years for customer acceptance. In the past two decades, extensive effort has been made to improve the cycle life of Li-ion batteries and understand their degradation mechanisms, especially for high power Li-ion batteries.¹³⁻¹⁸ Capacity fade and power fade have been reported to be two main types of degradation of Li-ion batteries.^{17, 18} There are several main factors associated with the capacity fade of Li-ion batteries including the formation/growth of SEI layer on the graphite anode/electrolyte interface^{13, 14, 19}, the loss of active electrode materials due to structural and chemical instability (e.g. volume change, phase transition, and dissolution)¹⁴, and Li plating at low temperature or over-charge conditions^{13, 14, 20, 21}. These processes lead to the consumption of cyclable Li, and thus a decrease in cell capacity. The power fade of Li-ion batteries is mainly associated with the internal impedance rise. A lot of factors are attributed to the cell impedance rise including the formation/growth of SEI layer on graphite anode/electrolyte interface^{13, 14, 19}, the formation/growth of passivation layers at cathode/electrolyte interface^{13, 14}, the loss of the contact between cell components¹⁴, the reduction of the conductivity of polyvinylidene fluoride (PVDF)-carbon composite binder²² and the reduction of electrolyte conductivity caused by the electrolyte decomposition¹⁴. Moreover, power fade of Li-ion batteries will lead to an additional capacity fade by lowering the operating voltage range. The degradation mechanisms of Li-ion batteries also depends on the cell chemistry^{17, 23}, electrode structure, and operating conditions^{20, 24, 25}. For example, high energy Li-ion batteries with thick electrodes may age differently than high power counterparts with thin electrodes. However, there are few reports on the investigation of degradation mechanisms for thick-electrode, high-energy Li-ion batteries in the literature.

$\text{Li}(\text{Ni}_{1/3} \text{Mn}_{1/3} \text{Co}_{1/3})\text{O}_2$ (NMC111) has already been commercialized for EV applications due to its relatively high capacity, low cost and excellent safety characteristics.³ However, its specific capacity is only 150~160 mAh/g, which is still not high enough for next-generation EV applications.³ Ni-rich NMC layered oxides can deliver higher capacity than NMC111 and potentially increase the energy density of lithium ion batteries. However, with increasing Ni content, Ni-rich NMC shows worse rate capability and poor stability. Great effort has been made to improve the stability and cycle life of Ni-rich NMC materials. For example, the stability and cycle life of Ni-rich NMC materials can be improved by surface modification/coating^{26, 27}, core-shell structure^{28, 29} and concentration-gradient structure^{5, 30, 31}. Most of the work on the evaluation of the cycle life of Ni-rich NMC materials has been done in either coin cells^{3, 5, 31} or small pouch cells⁵, and little work about the cycle life of Ni-rich NMC in large-format pouch cells has been reported in the literature¹⁰.

In this work, a set of high-energy pouch cells consisting of thick $\text{Li}(\text{Ni}_{0.6}\text{Mn}_{0.2}\text{Co}_{0.2})\text{O}_2$ (NMC622) cathodes and thick graphite anodes are cycled under 1C-rate charge and 2C-rate discharge at room temperature. A typical electrolyte solution such as 1.0 M lithium hexafluorophosphate (LiPF_6) in the mixture of ethylene carbonate (EC) and ethyl methyl carbonate (EMC) with a small amount of vinyl carbonate (VC) additive will be used since the cycle test will be performed under a typical voltage window of 2.8-4.2 V. Fresh and cycling aged cells at different cycle numbers will be diagnosed in two-electrode and *in-situ* three-electrode cells.

2.2 Experimental

2.2.1 Cell Fabrication

We fabricated ~3.3 Ah pouch cells using $\text{LiNi}_{0.6}\text{Mn}_{0.2}\text{Co}_{0.2}\text{O}_2$ (Umicore) as positive electrodes and graphite (Nippon Carbon) as negative electrodes with 1.0 M LiPF_6 dissolved in EC/EMC (3:7 by wt.) + 2 wt. % VC as electrolyte (BASF). The negative-to-positive (N/P) capacity ratio was designed at 1.2. The pouch cells contained 14 layers of negative electrodes and 13 layers of positive electrodes. A Celgard-2325 separator, 25 μm in thickness, was used. The negative and positive electrodes were fabricated using the same method as reported by our group before^{32, 33}. The loadings of NMC622 in the positive electrode and graphite in the negative electrode were ~19.4 and ~12.1 mg/cm^2 , respectively; and the total thickness of the double-sided positive and negative electrodes (including Cu or Al foil) was ~149 and ~175 μm , respectively. The designed reversible capacity based on the total positive electrode area was ~3.1 mAh/cm^2 . Each pouch cell had a 81 mm \times 55 mm footprint area, weighed 64.5 grams, and had a 3.3 Ah nominal capacity (related to which all C-rates in this work are given) with specific energy greater than 200 Wh/kg estimated at a size of 10 Ah or larger. In this work, all cells are high energy pouch cells with thick NMC622 and thick graphite electrodes except specifically stated.

2.2.2 Initial Screening

After a formation process, 20 pouch cells were screened. An initial rate capability test of all fresh pouch cells was performed at room temperature to examine the discharge capacity as a function of discharge C-rate. A multi-channel Arbin battery testing system (Model: BT 2000 with 32 channels, Arbin Instruments, USA) was used for the initial rate capability test. The initial rate

capability test included five charge/discharge cycles with the same charge process and five different discharge C-rates: C/3, 1C, 2C, 3C and 5C. First, the pouch cells were charged using a constant current/constant voltage (CC/CV) protocol, i.e. the cells were charged at 1C-rate current to 4.2 V, and then were held at 4.2 V until the measured current dropped below C/20-rate. After resting for 30 min, the cells were discharged until the cut-off voltage of 2.8 V was reached. After the initial performance check, 10 “very similar” cells were selected for cycle aging test. We assume that the cells with close discharge capacities under the same C-rate and similar high-frequency resistances (HFR) are “very similar”.

2.2.3 Cycle Aging Tests

Cycle aging tests of the 10 pouch cells were performed using a multi-channel LAND instrument battery testing system (Model CT2001B-5V-10A, Land Instruments, China) at room temperature. The cycle aging test protocol for each cycle included five steps: (1) a charge to 4.2 V at a 1C-rate, (2) a charge at a constant voltage of 4.2 V until the measured current dropped below C/10-rate, (3) a rest for 5 minutes, (4) a discharge to 2.8 V at a 2C-rate, and (5) a rest for another 5 minutes before going to the next cycle. When the cells reached a specific cycle number (for example, 300, 500, 1000 and 1500 cycles, etc.), the cycle aging test of one of the cells was stopped. Finally, 10 aged cells at varying cycle numbers were obtained. Please note that in this work, all aged cells refer to the cells that have been aged by cycling.

2.2.4 Diagnostic Tests

Two electrode and *in-situ* three-electrode diagnostic tests for the fresh and aged cells were performed to examine the cell performance decay and identify degradation mechanisms. In the literature, post-mortem analysis of aged Li-ion batteries as a very useful *ex-situ* method is often used to obtain chemical, structural and electrochemical change of electrode materials upon aging and identify the factors for the degradation.^{16, 20, 34-36} For electrochemical post-mortem analysis, re-constructed coin cells including half-cells and 3-electrode full cells with a Li reference electrode were fabricated from selected parts of aged electrodes. This kind of *ex-situ* electrochemical method allows us to obtain the electrochemical performance of the cell including remaining material capacity as well as impedance of aged positive and negative electrodes, respectively. However, during the reconstruction process, the interface between electrode and electrolyte and electrode microstructure may change. In this work, we will use an *in-situ* three-electrode method developed by our group¹⁷ to measure positive and negative electrode potentials along with full cell voltage during the charge/discharge performance test, and also measure the impedance of the individual electrodes and full cell. This *in-situ* three-electrode method does not change the interface between electrode and electrolyte and electrode microstructure, and also provides a way to obtain the electrochemical performance and impedance of individual electrodes for whole cells.

For the three-electrode diagnostic tests, a fully discharged cell (discharged to 2.7 V at 0.1C-rate) was partially opened along the edge of one side in an argon filled glove box and then assembled into a fabricated three-electrode cell holder with a lithium-metal reference electrode. The three-electrode cell holder was fabricated based on our previous design¹⁷, which was modified in order to fit the size and shape of the pouch cells used in this work. The pouch cell was placed in the three-electrode cell holder, which was filled with the same fresh electrolyte

solution as that for fresh cells. A copper wire with one end flattened was fitted in polyethylene tubing, and a piece of lithium metal was cold-welded to the flat surface to form a lithium reference electrode.¹⁷ The other end of the copper wire was used as an electrical contact with a cable. The lithium reference electrode was then inserted into the fitting in the cell holder. Two terminals were inserted into the fittings in the cell holder and tightly contacted the positive electrode tab as positive voltage and current probes, while another two terminals were inserted into the fittings in the cell holder and tightly contacted the negative electrode tab as negative voltage and current probes.

Two-electrode diagnostic tests included rate capability tests at room temperature, 1C discharge capacity tests at three different temperatures (40/0/-10 °C), and impedance tests at room temperature. A multi-channel Arbin battery test system (Model: BT 2000 with 6 channels, Arbin Instruments, USA) and a Modulab electrochemical test system (Solartron analytical, United Kingdom) were used for the capacity and impedance tests, respectively. An environmental chamber was used to control different ambient temperatures for the diagnostic test, except for room temperature. The test protocol for the capability test of aged cells was the same as that for initial rate capability test of fresh cells. For the capacity tests at different ambient temperatures, the cells were fully charged using CC (1C-rate)/CV (4.2 V) charging protocol at room temperature, and then the cells were discharged at required ambient temperature until a cut-off discharge voltage of 2.8 V was reached. For impedance tests at room temperature, the cells were fully charged and then discharged to ~90 % SOC at C/2-rate. After the cells were balanced for at least two hours at ~90 % SOC, impedance test was performed with an AC voltage amplitude of 5 mV in the frequency range of 50 kHz to 0.005 Hz.

Three-electrode diagnostic tests included rate capability test at 25 °C and impedance tests at two different ambient temperatures (25 and -10 °C). The three-electrode diagnostic tests were performed for a fresh and two selected aged cells. A multi-channel Arbin battery test system

(Model: BT 2000 with 6 channels, Arbin Instruments, USA) was used for the three-electrode rate capability tests at 25 °C. The test protocol for three-electrode rate capability tests was the same as for the two-electrode rate capability tests. During the three-electrode rate capability tests, two auxiliary channels were used to simultaneously record the positive and negative electrode potentials. A Modulab electrochemical test system combined with an environmental chamber was used to perform the impedance tests. For the impedance tests, the cells were fully charged using CC (C/2-rate)/CV (4.2 V) charging protocol, and then were discharged to ~80 % SOC using a C/2-rate at 25 °C. After the cells were balanced at ~80% SOC and required ambient temperature for at least four hours, impedance tests were performed for full cell, positive electrode and negative electrode in the frequency range of 50 kHz to 0.005 Hz.

2.3 Results and Discussion

2.3.1 Beginning-of-Life (BOL) Performance

Figure 2-1a shows the discharge performance as a function of C-rate for a fresh cell at room temperature. The cell can achieve a C/3 discharge capacity of 3.20 Ah and a C/3 discharge energy of 11.65 Wh, which corresponds to a Coulombic efficiency of ~ 99.3% (vs. a charge capacity of 3.22 Ah) and an energy efficiency of ~ 91.9% (vs. a charge energy of 12.67 Wh). If extrapolating the same electrodes and cell components to a 10 Ah or larger cell, the cell energy density can reach >200 Wh/kg. One can also find that the rate capability of the fresh cell is very poor, which is typical for a high energy cell. For example, at room temperature, the discharge capacities under 1C, 2C, 3C and 5C are 3.10, 2.07, 1.15 and 0.28 Ah, which are 96.9%, 64.7%, 35.9% and 8.8%, respectively, of the C/3 discharge capacity. It is believed that the poor rate capability for a high energy cell is related to high internal cell resistance due to large resistance

for Li ion transport within the thick electrodes. For a high energy cell, low temperature performance is also poor, as shown in Figure 2-1b. At 0, -10 and -25 °C, the cell can deliver 1C discharge capacities of 2.12, 1.35 and 0.35 Ah, which are corresponding to 68.4%, 43.5%, and 11.3% of the 1C discharge capacity at room temperature, respectively. The poor performance at low temperatures for a high energy cell is attributed to reduced conductivity of the electrolyte through the separator and inside the thick electrodes, limited lithium solid diffusivity in the electrode material particles and significantly increased charge-transfer resistance on the electrolyte-electrode interface.^{37, 38} In addition, with increasing temperature from room temperature (~23 °C) to 40 °C, 1C discharge performance improves slightly. In order to separate positive and negative electrode contributions from the full cell performance, the measurement of the capacity and impedance in a three-electrode cell was performed, as shown in Figures 2-1c and 2-1d, respectively. From Figure 2-1c, one can find that the difference between the positive and negative electrode potentials is almost the same as the full cell voltage at the same relative capacity (i.e. depth of discharge, DOD). In addition, the cell measured in a three-electrode cell can deliver a C/3 discharge capacity and energy of ~3.17 Ah and ~11.58 Wh, respectively, which are almost the same as those measured in a two-electrode cell (Figure 2-1a). Moreover, the profile of the positive and negative electrode potentials as functions of DOD is consistent with the results for either half-cells or full cells with Li reference electrodes as reported in the literature.^{17, 39, 40} The results shown in Figure 2-1c implies that our three-electrode method can be used to effectively separate the positive and negative electrode potentials from full cell voltage during charge-discharge cycle, and the installation of Li reference electrode has no negative effect on the measurement of full cell voltage or cell charge/discharge capacity and energy. Moreover, as evidenced by Figure 2-1d, the sum of the positive and negative electrode impedances is almost the same as full cell impedance in the frequency range from 10 kHz to 0.005 Hz. However, there is some deviation of the sum of the positive and negative electrode impedance from the full cell

impedance in the very high frequency range (>10 kHz), which is due to the different effects of inductance behavior on the positive/negative electrode and full cell impedances. In addition, at 25 °C, the cell impedance at 80% SOC is dominated by the positive electrode impedance, while the negative electrode impedance is quite small. This implies that the rate capability of a high energy cell mainly depends on the positive electrode.

Figure 2-2 shows the effect of C-rate on full cell voltage and positive and negative electrode potentials as functions of relative capacity measured in a three-electrode cell during 1C charge-C/3 discharge process for a fresh cell at 25 °C. Capacity was normalized based on the C/3 discharge capacity of 3.17 Ah measured in the three-electrode cell. It is confirmed that for a high energy cell, rate capability of the cell mainly depends on the positive electrode. At 25 °C, since the kinetics of graphite negative electrode are fast, the negative electrode potential changes slightly with increasing C-rate from C/3 to 3C. Moreover, due to the sluggish kinetics of the NMC622 positive electrode, the decrease in full cell voltage with increasing C-rate mainly comes from the decrease in the positive electrode potential. This result is consistent with the three-electrode impedance test shown in Figure 2-1d.

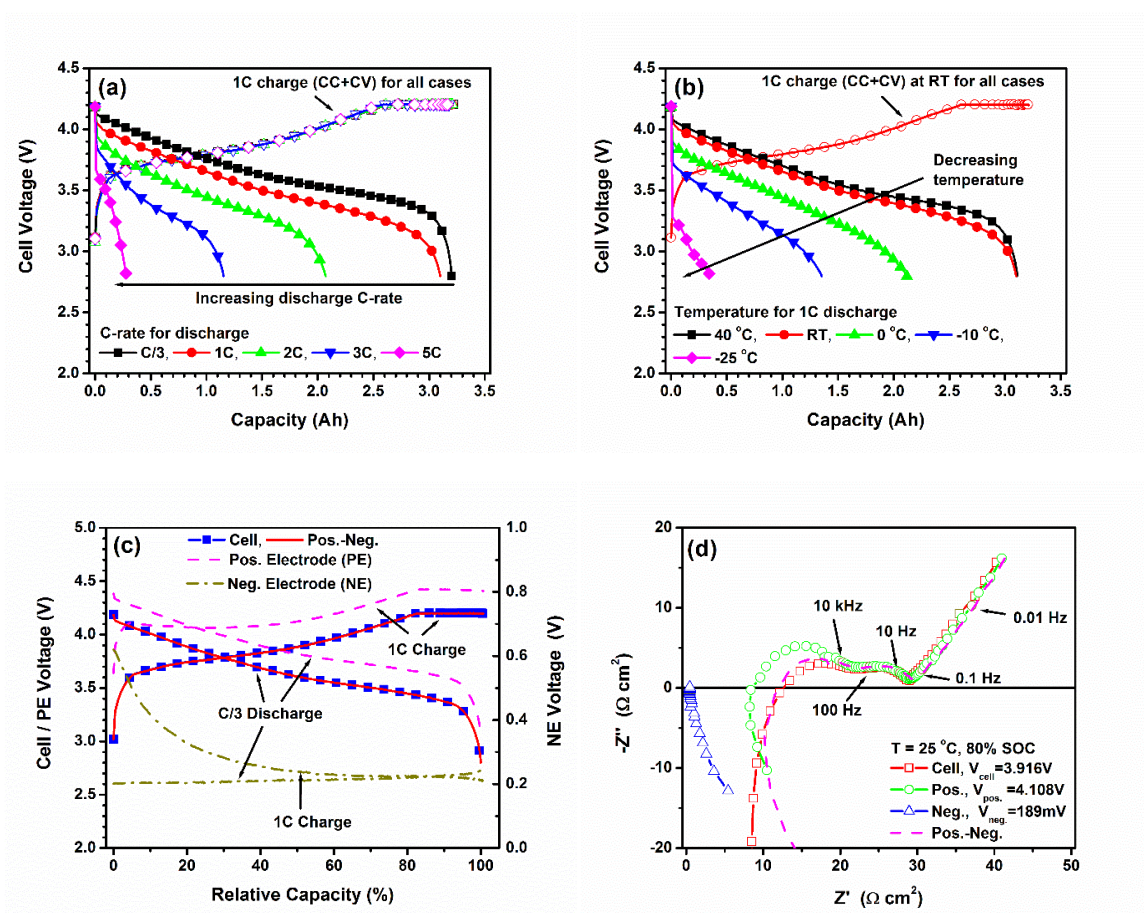


Figure 2-1. Beginning-of-Life (BOL) performance of a high energy NMC622/graphite cell with 200 Wh/kg: (a) discharge performance under different C-rate at room temperature (~23 °C) ; (b) temperature effect on 1C discharge performance; (c) separation of positive and negative electrode potentials from full cell voltage in a three-electrode cell during 1C charge-C/3 discharge process at 25 °C (Note: Capacity is normalized based on the C/3 discharge capacity measured in a three-electrode cell: 3.17 Ah); (d) separation of positive and negative electrode impedance from whole cell impedance in a 3-electrode cell at 25 °C (Note: impedance has been normalized based on total positive electrode area of 1055 cm²).

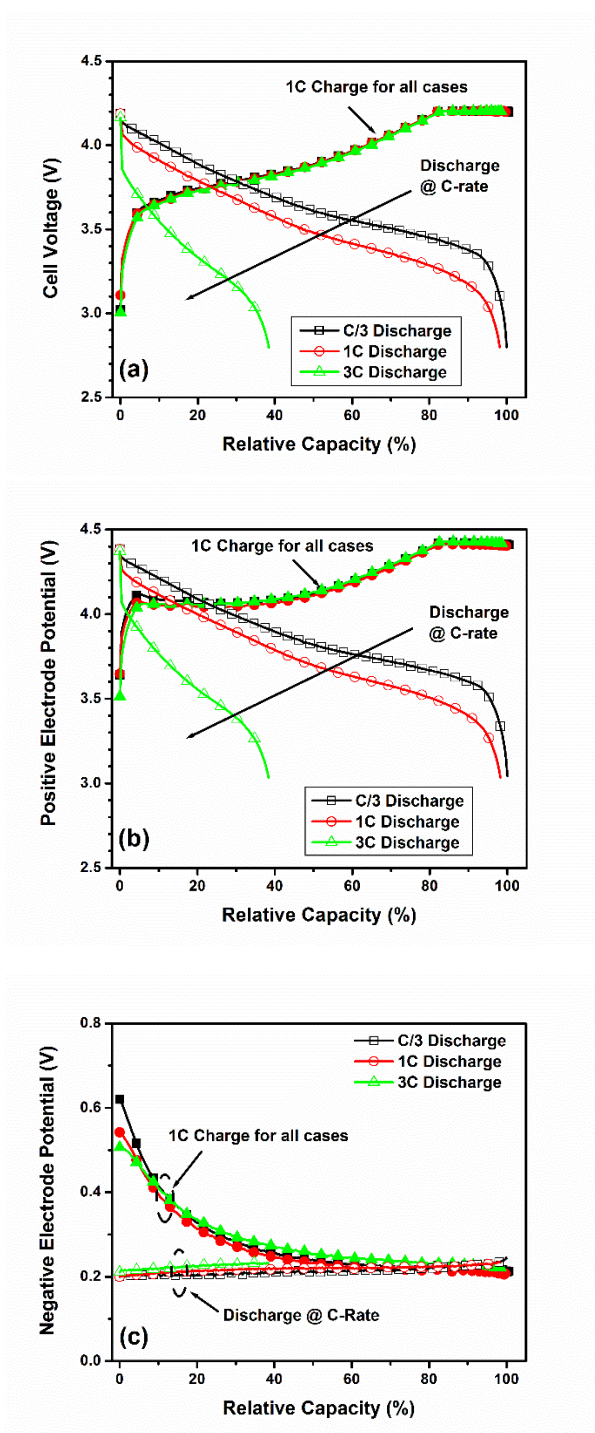


Figure 2-2. Effect of C-rate on (a) full cell voltage, (b) positive and (c) negative electrode potentials during 1C charge-C/3 discharge process for a fresh high energy NMC622/graphite cell at 25 °C. (Note: Capacity is normalized based on the C/3 discharge capacity of 3.17 Ah measured in a three-electrode cell).

2.3.2 Capacity Fade

The change of C/3 discharge capacity and capacity retention upon cycling is used to describe the capacity fade with cycle aging. Capacity retention is defined as the ratio of the discharge capacity of an aged cell at a certain cycle number to that of a fresh cell. Figure 2-3 shows 1C charge-C/3 discharge curves and C/3 capacity retention as a function of cycle number for the cells. During the initial stage (within 66 cycles), there is ~7.3% loss in the C/3 discharge capacity, while almost no power fade is observed. During the secondary stage (from 66 to 1000 cycles), there is gradual capacity loss and power fade with cycle number. The capacity retention drops by ~5% (from 92.7 to 87.7%) from 66 to 1000 cycles. However, after 1000 cycles (final stage), the capacity decay becomes fast and power fade becomes significant. The decay rate in the C/3 capacity retention during initial, secondary, and final stages is 11.06%, 0.54% and 3.46% per 100 cycles, respectively. In the case of C/3 discharge performance, there is almost no effect of power fade on the capacity fade since the aged cell capacity is still limited by a diffusion process. We will focus on capacity fade in this section and discuss power fade later.

For a comparison, another batch of high energy pouch cells with thick NMC111 (Umicore) cathodes and thick graphite anodes were fabricated with the same procedure. The NMC111/graphite cells have similar electrode thickness, loading and cell size to NMC622/graphite cells except for the cathode materials. C/3 capacity retention at room temperature as a function of cycle number of high energy NMC111/graphite cells is also shown in Figure 2-3b. The trend in the capacity decay with cycle number for the NMC111/graphite cells is similar to that for the NMC622/graphite cells. Since NMC622 materials are less stable than NMC111³, cycle life for the NMC622/graphite cells is shorter than that for the NMC111/graphite cells (1419 vs. 1860 cycles with capacity retention of 75%) as expected. This implies that the NMC622/graphite cells should have a similar degradation mechanism to the NMC111/graphite

cells. In the literature, the degradation mechanisms for lithium ion cells with NMC111⁴¹⁻⁴³, $\text{Li}(\text{Ni}_{0.5}\text{Mn}_{0.3}\text{Co}_{0.2})\text{O}_2$ (NMC532)⁴⁴, NMC111/ LiMn_2O_4 blend^{16, 20}, and NMC532/ LiMn_2O_4 blend⁴⁵ cathodes have been well documented. In these reported work, the capacity fade of these cells with NMC-based cathodes is mainly attributed to the loss of cyclable lithium caused by SEI layer formation/growth at the anode, and loss of active materials at the cathode. Similar degradation mechanism has also been proposed for lithium ion cells with other cathode materials^{14, 19, 34, 46}. For example, Snyder *et al.*¹⁹ found that the entirety of capacity loss up to 80 cycles in LiCoO_2 /graphite cells can be attributed to the loss of lithium inventory caused by SEI formation and repair. Therefore, for the NMC622/graphite cells studied in this work, the sharp decrease in C/3 capacity retention during the initial stage is considered to be due to the loss of cyclable lithium caused by the quick growth of solid-electrolyte interphase (SEI) layer on the graphite negative electrode. Gradual decrease in C/3 capacity retention during the secondary stage is attributed to continuously slow growth of the SEI layer at the surface of graphite negative electrode and loss of active materials on the positive electrode. During the final stage, significant drop in C/3 capacity retention is believed to be due to lithium plating. Lithium plating has been considered as one of the main reasons attributed to the abrupt capacity fade during the final stage in the literature.^{13, 23, 24, 34, 42} For example, Schuster *et al.*²⁴ reported that the abrupt capacity fade after the “turning point” from linear to non-linear aging characteristics is due to *aging induced lithium plating*, which may originate from reduced ionic kinetics of the graphite negative electrode as a result of SEI growth and the loss of graphite active materials. Burns *et al.*⁴² believed that electrolyte oxidation products are produced at the positive electrode and migrate to the negative electrode where they are reduced as a solid layer of unwanted materials on the front surface of the negative electrode; moreover, after a sufficient number of cycles the layer of unwanted materials becomes thick enough to significantly reduce ion transport to the bulk of the

negative electrode, which leads to large kinetic issues when trying to cycle the cell and subsequent lithium plating.

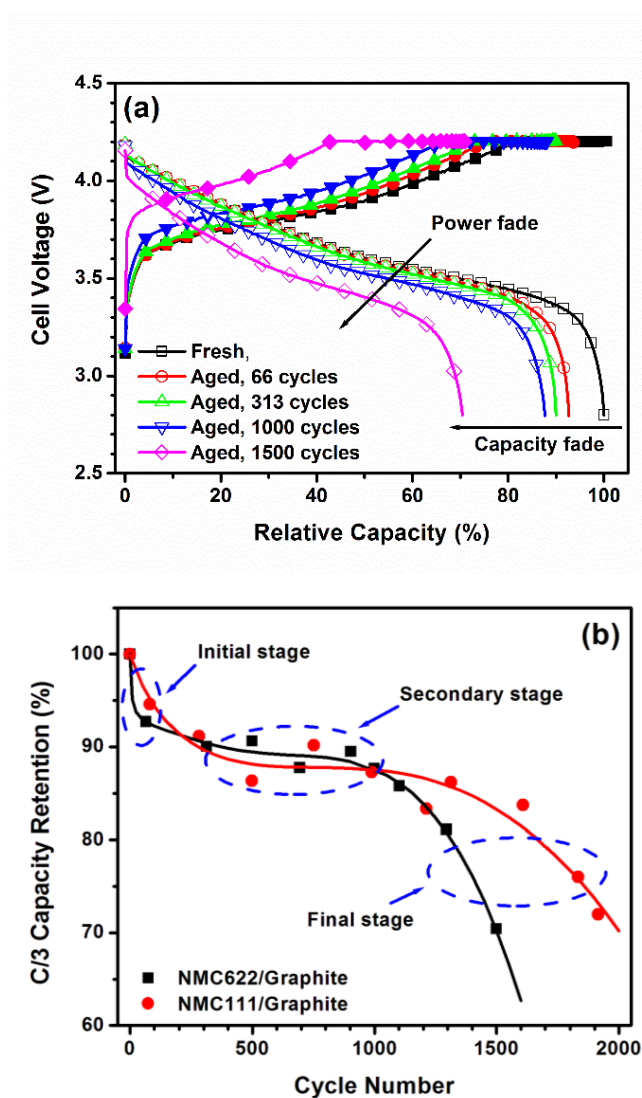


Figure 2-3. (a) 1C charge and C/3 discharge curves of aged cells (Note: Capacity is normalized based on the C/3 discharge capacity of 3.20 Ah for a fresh cell), and (b) C/3 capacity retention at room temperature ($\sim 23^{\circ}\text{C}$) as a function of cycle number for high energy NMC622/graphite cells. For a comparison, C/3 capacity retention at room temperature as a function of cycle number for high energy NMC111/graphite cells with similar electrode thickness, loading and cell size fabricated with the same procedure is also shown in Figure 2-3b.

2.3.4 Power Fade

Figure 2-4a shows 1C charge-1C discharge performance of fresh and aged cells at room temperature. One can find that within 313 cycles, there is almost no power fade in the case of 1C discharge and cell performance decay is mainly the capacity fade. However after 313 cycles, there is a significant power fade upon further cycle aging, especially from 904 to 1500 cycles. In order to identify whether the power fade comes from either the positive or negative electrode, three-electrode diagnostic tests were performed for a fresh and two aged cells with 904 and 1500 cycles. Figures 2-4b, 4c and 4d show full cell voltage, positive and negative electrode potentials, respectively, as a function of discharge capacity during the 1C discharge process for fresh and aged cells at 25 °C. It is noted that the performance of the aged cell at 1500 cycles improves when it was measured in a three-electrode cell, compared with a two-electrode cell. This kind of performance improvement is due to the reduction in contact resistance and the use of fresh electrolyte solution in the three-electrode cell. We will discuss this issue in detail later. Table 2-I summarizes the average full cell voltage and positive and negative electrode potentials measured in a three-electrode cell during 1C discharge step at 25 °C. In the case of 1C discharge, the power fade of the cell upon aging mainly comes from the positive electrode. For example, after cycle aging for 904 cycles, the average full cell voltage decreases by ~91 mV, which mainly comes from the decrease in the average positive electrode potential (~93 mV), while the average negative electrode potential changes minimally. After cycle aging for 1500 cycles, the average positive electrode potential decreases by ~180 mV, while the average negative electrode potential decreases by ~19 mV. This implies that the power performance of positive electrode is worsen, while that of negative electrode is improved. The improvement in the performance of negative electrode may be related to increased electrochemical reaction area of negative electrode materials caused by the dramatic crack propagation of graphite negative electrode materials, as to

be confirmed by three-electrode impedance tests at -10°C later. Therefore, the average full cell voltage decreases by ~162 mV, which also mainly comes from the positive electrode.

Generally, power fade of a Li-ion cell upon aging is directly related to the impedance rise of the cell. In order to identify the degradation mechanism for the cell power fade, the impedance of fresh and aged cells was measured at 90% SOC and room temperature in a two-electrode cell, as shown in Figure 2-5a. For most of the aged cells (at ≥ 313 cycles), there are two obvious arcs located in the high-frequency and medium-frequency regions, followed by a Warburg diffusion impedance (a straight line) located in low-frequency region. While for the fresh cell and aged cell at 66 cycles, the two arcs in the high- and medium- frequency regions are overlapped. From the impedance test of a fresh cell (Figure 2-1d) and that for aged cells at 904 and 1500 cycles in a three-electrode cell, Figure 2-6, it was confirmed that the full cell impedance mainly comes from the positive electrode. High-frequency arc is attributed to the migration of Li ion through the surface film formed/grown on the positive electrode active materials^{41, 47, 48} and/or electronic transport in the electrode^{49, 50}, while the medium-frequency arc is related to the charge-transfer reaction^{47, 48, 50}. The Warburg diffusion impedance in the low-frequency region is related to Li solid diffusion in the active materials and electrolyte salt diffusion process.^{17, 37, 51} An equivalent circuit with two time constants (Figure 2-5b) was proposed and used to fit the experimental impedance data in the high- and medium-frequency region. In the equivalent circuit, L is the high-frequency inductance due to cable wires; R_{ohm} is ohmic resistance from the electrodes, electrolyte, separator, current collector and the contact between cell components; CPE_1 and R_1 are constant-phase-element (CPE) and resistance related to the Li migration through the surface film and/or electronic transport in the positive electrode, respectively; and CPE_2 and R_2 are the CPE and charge-transfer resistance related to the charge-transfer reaction at the electrodes (the positive electrode mainly), respectively. The impedance of CPE is defined by the equation:

$Z_{CPE} = A/(j\omega)^n$, where j is the complex number, ω is the angular frequency, and A is the

coefficient of the impedance of CPE. The fitting parameter values for the cell impedance of fresh and aged cells at 90% SOC and room temperature are summarized in Table 2-II. The experimental impedance spectra of the cells and the fitted ones show good agreement for all fresh and aged cells, as illustrated in Figure 2-5a. Figure 2-5c shows the evolution of resistances related to different processes as a function of cycle number at room temperature for the cells. The ohmic resistance (R_{ohm}) and charge-transfer resistance (R_2) are both nearly constant within 1000 cycles, and they gradually increase with cycle number after 1000 cycles. The resistance related to Li ion migration through surface film/electronic transport (R_1) significantly increases with increasing cycle number from 0 to 1500 cycles, which is a result of the growth of surface film on the positive electrode active materials. After 313 cycles, the contribution of the resistances to the total cell resistance is in the order: resistance related to Li ion migration through surface film/electronic transport (R_1) > charge-transfer resistance (R_2) > ohmic resistance (R_{ohm}), and the contribution of R_1 becomes larger with more cycles. The total cell resistance (R_{total}), the sum of R_1 , R_2 and R_{ohm} , significantly increases with cycle number. For example, for an aged cell at 1500 cycles, the total cell resistance is $\sim 109 \Omega \text{ cm}^2$, more than three times that for a fresh cell ($\sim 30 \Omega \text{ cm}^2$). Great increase in the cell resistance upon aging leads to a significant power fade, as shown in Figure 2-4.

Three-electrode impedance tests for fresh and aged cells were performed in order to explore how the change of the positive and negative electrode impedance upon aging affects the cell impedance rise. Figure 2-6 shows a comparison of the full cell, positive electrode and negative electrode impedances at 80% SOC and 25 °C among fresh and two aged cells with 904 and 1500 cycles. One can find that the positive electrode dominates the full cell impedance, for both fresh and aged cells. Compared with the positive electrode impedance, the negative electrode impedance is small and can be neglected. The same equivalent circuit shown in Figure 2-5b was used to fit the cell and positive electrode impedance spectra (except for Warburg

diffusion impedance in the low-frequency region) measured in a three-electrode cell. Please note that in the case of positive electrode impedance, R_{ohm} is ohmic resistance of a half-cell consisting of positive electrode, CPE1 and R_1 are related to Li ion migration through surface film on the positive electrode active materials and/or electronic transport in the positive electrode, and CPE2 and R_2 are related to the charge-transfer reaction at the positive electrode. The experimental impedance spectra of the full cells and positive electrodes and the fitted ones show good agreement for the fresh and aged cells, as illustrated in Figure 2-6a and 6b. The fitting parameter values for the full cell and positive electrode impedance as a function of cycle number at 80% SOC and 25 °C are summarized in Table 2-III. Figure 2-7 shows a comparison in the resistance related to different processes fitted from the impedance test data (Figures 2-6a and 6b) between full cell and positive electrode at 25 °C. For fresh and aged cells, the resistance related to Li ion migration through the surface film/electronic transport (R_1) and the charge-transfer resistance (R_2) for the positive electrode are almost the same as those for the full cell. Moreover, with increasing cycle number, the increase in the resistance related to Li ion migration through the surface film/electronic transport (R_1) and charge-transfer resistance (R_2) for the positive electrode impedance followed almost the same trend as that for the full cell. In addition, the rise in cell impedance upon aging mainly comes from the increase in the positive electrode impedance. These results imply that the power fade of the cell upon aging is mainly due to the positive electrode including the increase in the resistance related to Li ion migration through the surface film/electronic transport, and the increase in its charge-transfer resistance, which is consistent with the discharge performance of the full cell and the positive electrode measured in a three-electrode cell (Figure 2-4).

Table 2-1. Average full cell voltage, positive and negative electrode potentials measured by a 3-electrode cell during 1C discharge of fresh and aged high energy NMC622/graphite cells at 25 °C.

Cycle number	Average full cell voltage (V)	Average positive electrode potential (V)	Average negative electrode potential (V)
fresh	3.527	3.754	0.229
904 cycles	3.436	3.661	0.227
1500 cycles	3.365	3.573	0.210

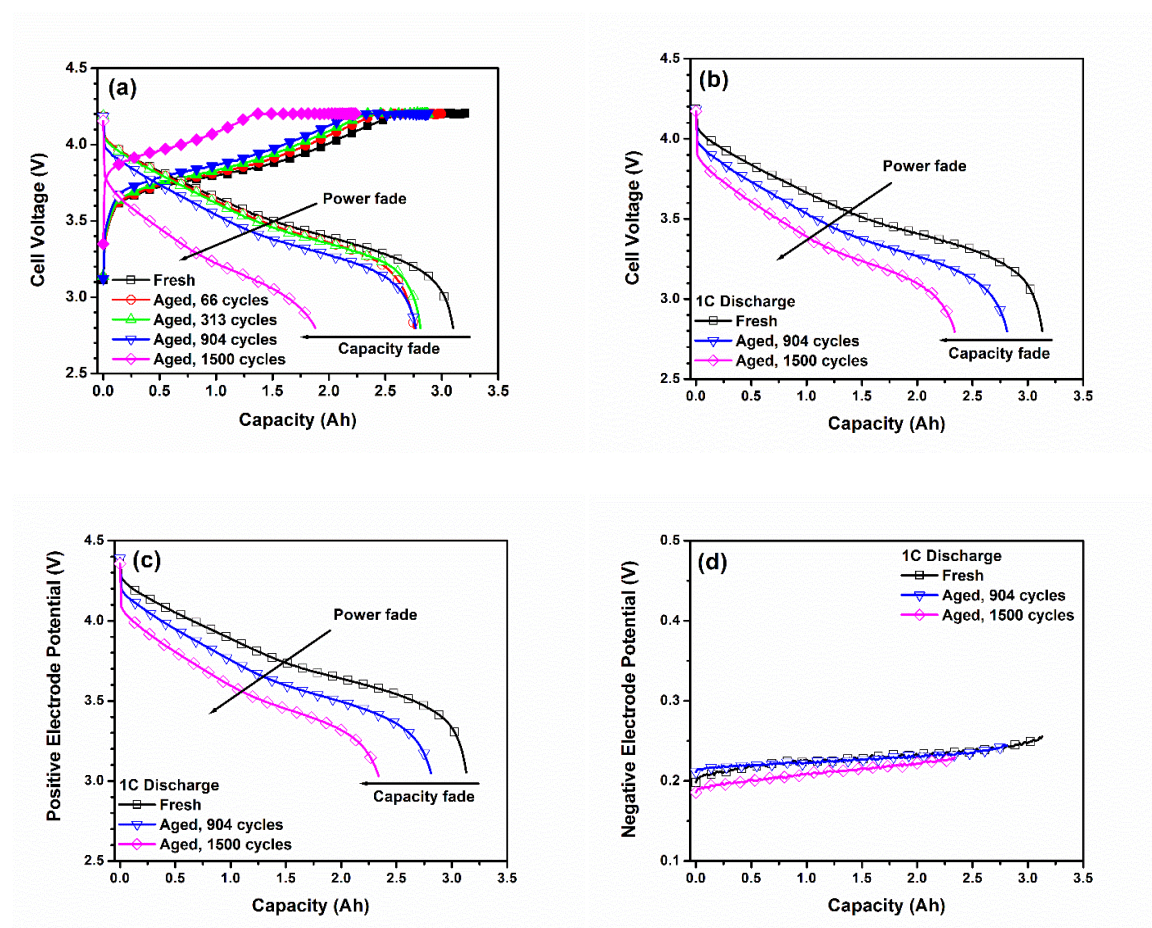
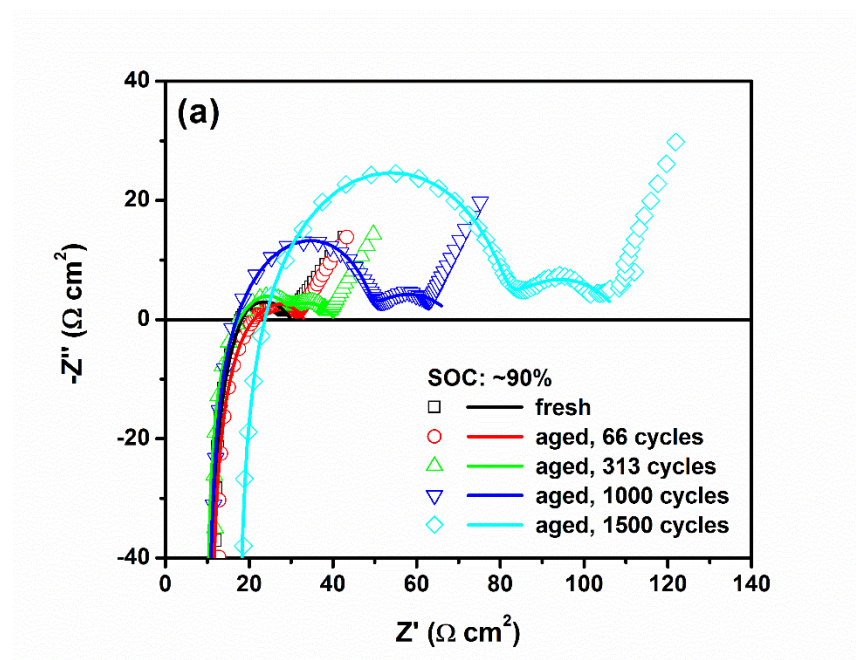


Figure 2-4. 1C charge/1C discharge performance of aged cells measured in (a) a two-electrode cell at room temperature (~23 °C) and (b, c, d) a three-electrode cell at 25 °C. In three-electrode diagnostic test, (b) full cell voltage, (c) positive and (d) negative electrode potentials as a function of discharge capacity were measured simultaneously during the discharge process.

Table 2-2. . Fitting parameter values for the impedance spectra (excluding diffusion line part) of a fresh and selected aged cells measured under 90% SOC at room temperature using two-electrode configuration shown in Figure 2-5a.

Cycle No.	fresh	66	313	1000	1500
L (mH cm^2)	0.315	0.341	0.243	0.305	0.293
Rohm ($\Omega \text{ cm}^2$)	9.17	9.97	9.30	9.54	16.4
R ₁ ($\Omega \text{ cm}^2$)	8.06	11.6	18.2	38.0	63.8
CPE ₁ A ₁ ($\mu\text{F cm}^2$)	5.96	4.18	2.78	1.99	2.09
n ₁	0.913	0.939	0.957	0.959	0.923
R ₂ ($\Omega \text{ cm}^2$)	12.7	11.6	13.0	21.6	29.2
CPE ₂ A ₂ (mF cm^2)	2.66	4.82	6.96	11.6	7.21
n ₂	0.561	0.526	0.504	0.472	0.541
R _{total} ($\Omega \text{ cm}^2$)	29.9	33.1	40.5	69.1	109.3



(b)

Li ion migration through surface film on positive electrode active materials and/or electronic transport in the positive electrode

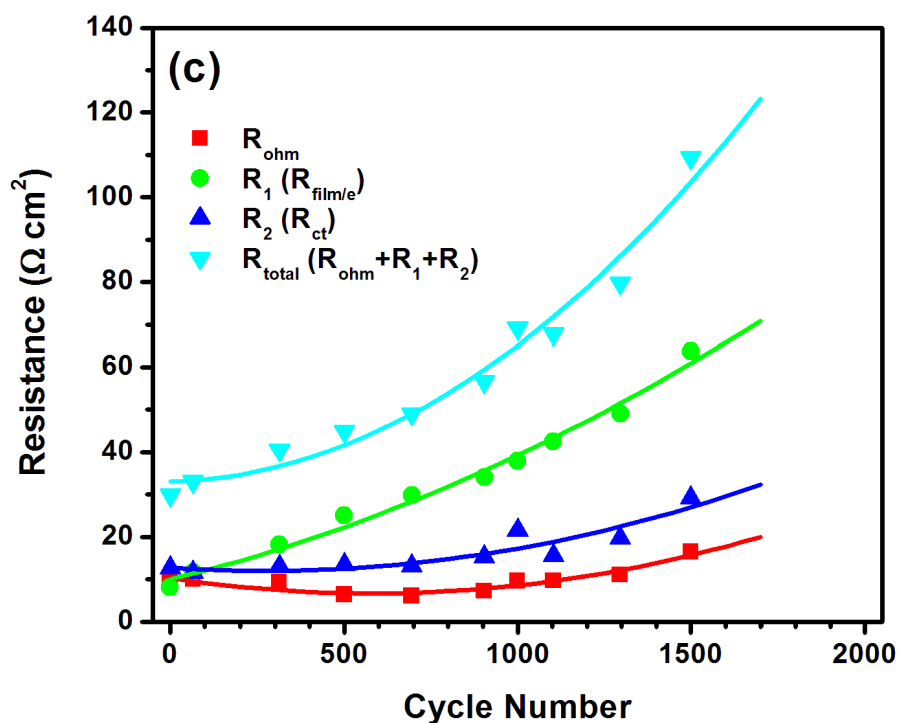
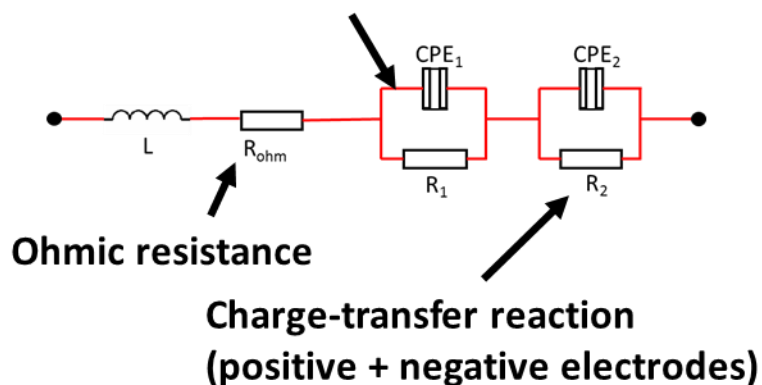


Figure 2-5. (a) Cell impedance of a fresh and selected aged cells measured at 90% SOC and room temperature using two-electrode cell (symbols: experimental data, lines: fitted), (b) An equivalent circuit used for fitting cell impedance spectra shown in Figure 2-5a (Note: Warburg diffusion impedance showing a inclined line in the low frequency range isn't included in the equivalent

circuit), (c) Evolution of resistances related to different processes as a function of cycle number at room temperature for high energy NMC622/graphite cells. (Note: impedance has been normalized based on total positive electrode area of 1055 cm^2).

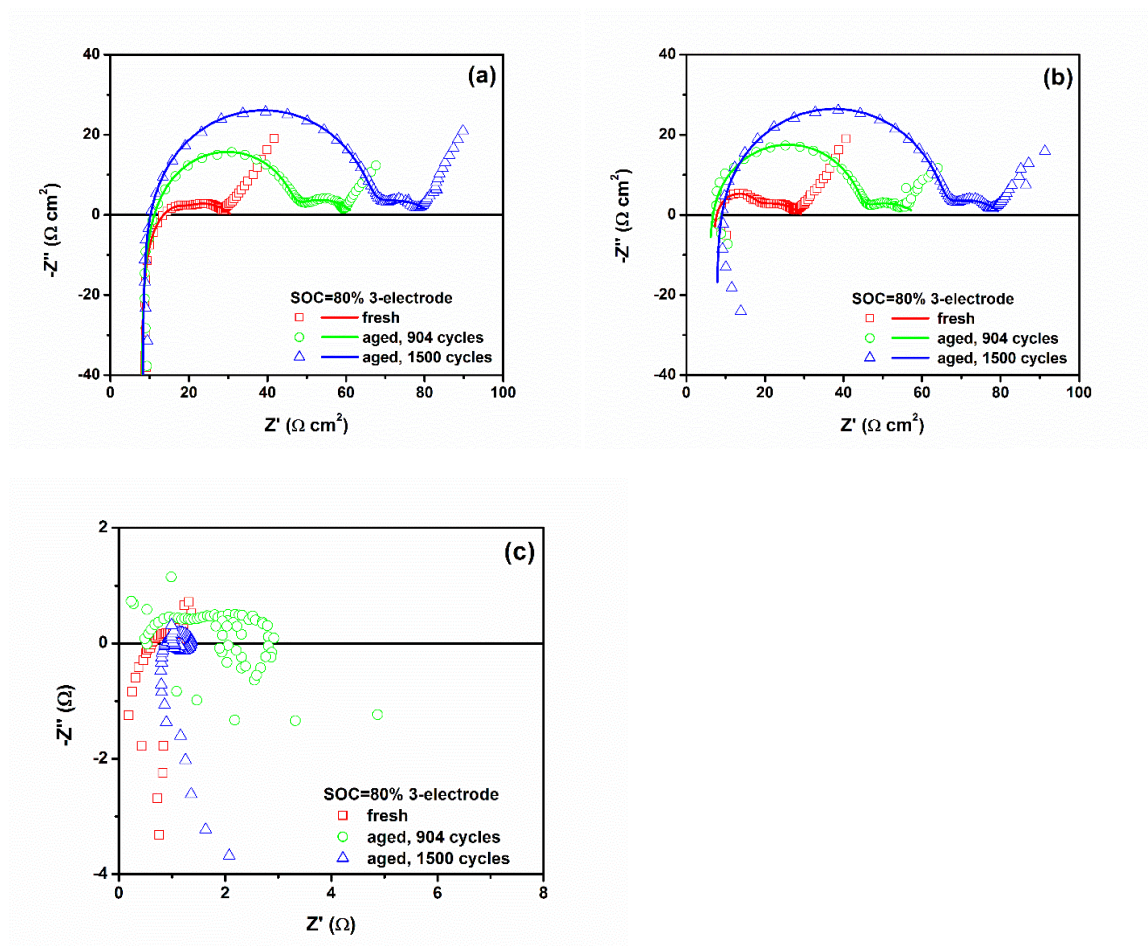


Figure 2-6. A comparison of (a) full cell, (b) positive electrode and (c) negative electrode impedance measured at 80% SOC and 25 °C (symbols: experimental data, lines: fitted) in a 3-electrode cell among a fresh and two aged cells at 904 and 1500 cycles.

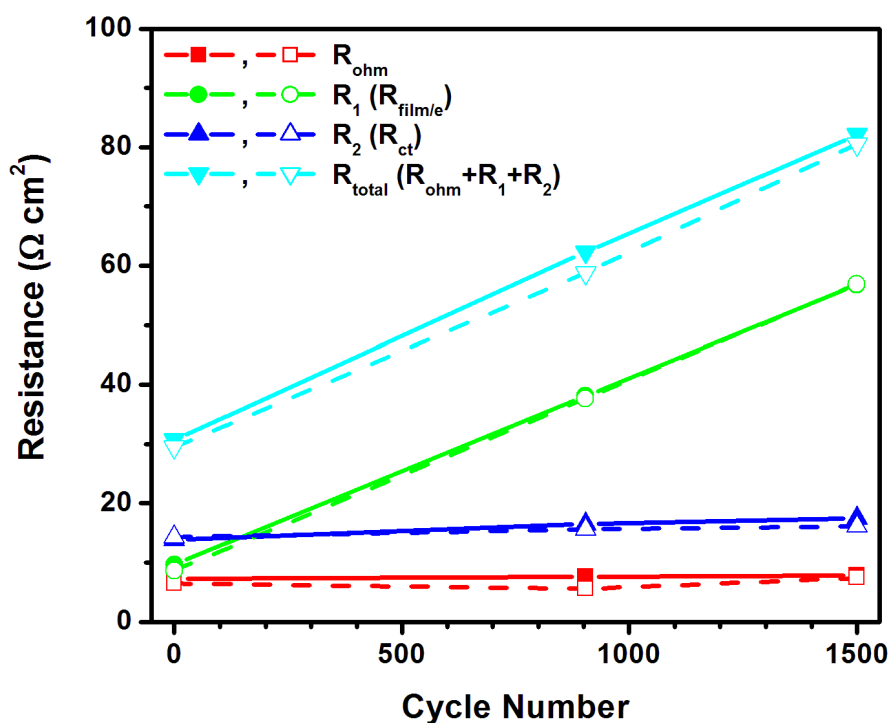


Figure 2-7. A comparison in the resistances related to different processes at 25 °C between full cell (solid line + solid symbol) and positive electrode (dash line + open symbol) fitted from the impedance test data shown in Figure 2-6. (Note: impedance has been normalized based on total positive electrode area of 1055 cm²).

Table 2-3. Fitting parameter values for the impedance spectra (excluding Warburg diffusion impedance) of a fresh and two aged cells (at 904 and 1500 cycles) measured at 80% SOC and room temperature in a three-electrode cell shown in Figures 2-6a and 6b.

Cycle No.	Fresh		Aged, 904 cycles		Aged, 1500 cycles	
	cell	positive	cell	positive	cell	positive
L (mH cm ²)	0.123	0.017	0.128	0.031	0.108	0.071
R _{ohm} (Ω cm ²)	7.26	6.47	7.62	5.57	7.86	7.41
R ₁ (Ω cm ²)	9.65	8.68	38.1	37.7	56.8	56.9
CPE ₁ A ₁ (μF cm ⁻²)	2.04	1.28	2.27	1.94	1.82	1.77
n ₁	1.002	1.061	0.949	0.960	0.965	0.966
R ₂ (Ω cm ²)	13.8	14.3	16.6	15.6	17.5	16.1
CPE ₂ A ₂ (mF cm ⁻²)	3.23	2.93	9.19	15.7	10.8	10.8
n ₂	0.485	0.465	0.526	0.444	0.466	0.512
R _{total} (Ω cm ²)	30.7	29.5	62.3	58.8	82.1	80.5

2.3.5 Performance Fade at Low Temperature

Figures 2-8a and 8b show 1C discharge performance of fresh and aged cells at 0 and -10 °C, respectively. Before the discharge, the cells are fully charged using CC (1C-rate) / CV (4.2 V) protocol at 25°C. At both 0 and -10 °C, there is not only a significant capacity fade, but also a great power fade upon aging, especially from 1000 to 1500 cycles. Compared with the power fade at room temperature, the power fade at low temperatures becomes more significant. Figure 2-8c shows 1C discharge capacities as a function of cycle number at four different temperatures in the range from 40 to -10 °C. Generally, the capacity decay at lower temperature becomes faster, which is due to stronger effect of power fade on the 1C discharge performance.

In order to identify the source of the significant power fade at low temperatures, impedance tests using the three-electrode configuration was performed at -10 °C for fresh and aged cells. Figure 2-9 shows a comparison of the full cell, positive electrode and negative electrode impedances at 80% SOC at -10 °C for a fresh and two aged cells at 904 and 1500 cycles. In the case of full cell impedance (Figure 2-9a), there is an arc, a diffusion line, another arc and a short inclined line related to Warburg diffusion impedance located in the high, medium, low and extra-low frequency regions, respectively. Compared with the full cell impedance at 25 °C (Figure 2-6a), an additional diffusion line appears in the medium-frequency region at -10 °C. Since full cell impedance (real part and imaginary part) is theoretically the sum of positive electrode impedance and negative electrode impedance at every frequency, based on the analysis of the characteristic frequencies of the arcs and additional diffusion line that appeared in impedance spectra, it can be found that the high-frequency arc and the medium-frequency diffusion line of the full cell come from the positive electrode only. For the low-frequency arc, it is contributed by both positive and negative electrodes in the case of the fresh cell; while it mainly comes from the positive electrode and the contribution of the negative electrode is small

in the case of two aged cells. When temperature is reduced from room temperature to $-10\text{ }^{\circ}\text{C}$, due to slow lithium solid diffusion process in the particles of the electrode active materials and sluggish electrolyte salt diffusion in the electrodes, Warburg diffusion impedance becomes very large and a line related to Warburg diffusion impedance needs to be captured in extremely low frequency region. In this work, Warburg diffusion impedance appears as a short inclined line at $-10\text{ }^{\circ}\text{C}$ when frequency is swept to the low frequency limit of 0.005 Hz . In the case of positive electrode impedance at $-10\text{ }^{\circ}\text{C}$, similar impedance pattern to full cell impedance is observed. Like that at $25\text{ }^{\circ}\text{C}$, the arcs in the high-frequency and the low-frequency region at $-10\text{ }^{\circ}\text{C}$ are attributed to the Li ion migration through surface film formed/grown on the positive electrode active materials and the charge-transfer reaction, respectively, while the additional diffusion line in the medium-frequency region at $-10\text{ }^{\circ}\text{C}$ may be due to the electronic transport in the positive electrode.⁵¹⁻⁵³ Sun *et al.*^{52, 53} investigated the impedance of LiMn_2O_4 and $\text{LiNi}_{1/3}\text{Co}_{1/3}\text{Mn}_{1/3}\text{O}_2$ cathodes and observed a similar phenomenon. In their work, the author also claimed that the high-frequency depressed arc at room temperature includes the contribution of electronic transport in the electrode⁵². In the case of negative electrode impedance at $-10\text{ }^{\circ}\text{C}$, for a fresh cell, there is a small arc and a large arc in the high and low-frequency region, respectively, and an inclined line related to Warburg diffusion impedance in the extra-low frequency region; while for the two aged cells, the short inclined line related to Warburg diffusion impedance disappears. The high and low frequency arcs are attributed to the growth of solid-electrolyte interphase (SEI) layer and charge-transfer reaction at the negative electrode, respectively. The short inclined line is due to slow lithium solid diffusion in graphite particles and electrolyte salt diffusion in the negative electrode.⁵⁴

Two different equivalent circuits, as shown in Figure 2-10, were proposed to fit the impedance data (except for the inclined line related to Warburg diffusion impedance), one for the

full cell and positive electrode and one for the negative electrode. The equivalent circuit for the impedance spectra in the case of full cell and positive electrode consists of three different time constants besides an inductor L and an ohmic resistance R_{ohm} . Specifically, a constant-phase element (CPE) (CPE_{MF}) parallel with a resistance (R_{MF}) was used to fit the additional diffusion line in the medium-frequency region for better fitting. R_1 and CPE_1 for high-frequency arc are the resistance and corresponding capacitance related to Li ion migration through surface film on the positive electrode active materials, R_{MF} and CPE_{MF} for the medium-frequency region are the resistance and corresponding capacitance related to electronic transport in the positive electrode, and R_2 and CPE_2 for the low-frequency arc are the charge-transfer resistance and double-layer capacitance. On the other hand, the equivalent circuit for the negative electrode impedance spectra consists of two different time constants besides an inductor L and an ohmic resistance R_{ohm} . R_1 and CPE_1 for high-frequency arc are the resistance and corresponding capacitance related to the growth of SEI layer on the negative electrode, while R_2 and CPE_2 for low-frequency arc are the charge-transfer resistance and double-layer capacitance. The impedance spectrum of the negative electrode was fitted for the fresh cell only. It is very difficult to fit the impedance spectra for the negative electrode in the aged cells due to the complexity of their impedance data. Instead, charge-transfer resistance and total polarization resistance for the negative electrode in the case of aged cells were estimated directly from the impedance spectra.

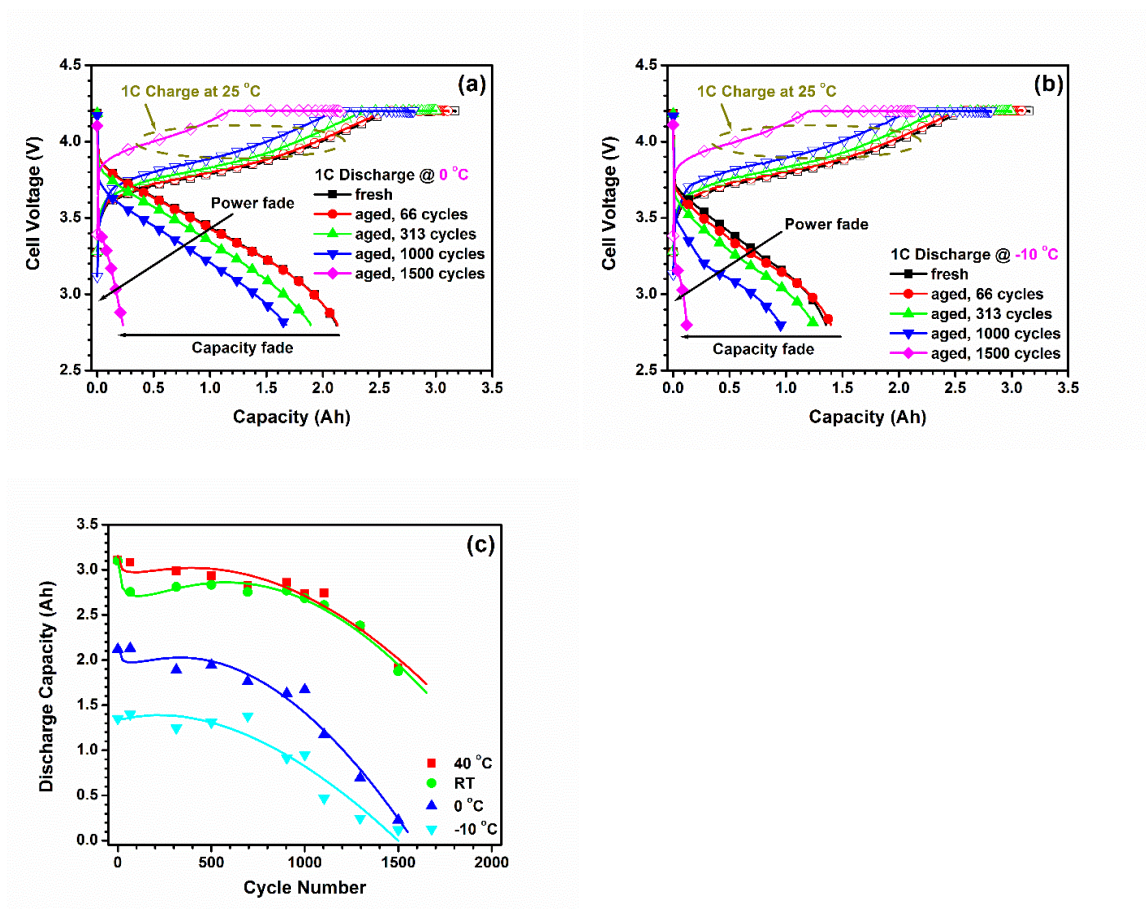


Figure 2-8. 1C charge curves at 25 °C and 1C discharge curves at required ambient temperature (a) 0 °C and (b) -10 °C, of aged cells, and (c) 1C discharge capacity as a function of cycle number at four different temperatures in the range from 40 to -10 °C for high energy NMC622/graphite cells.

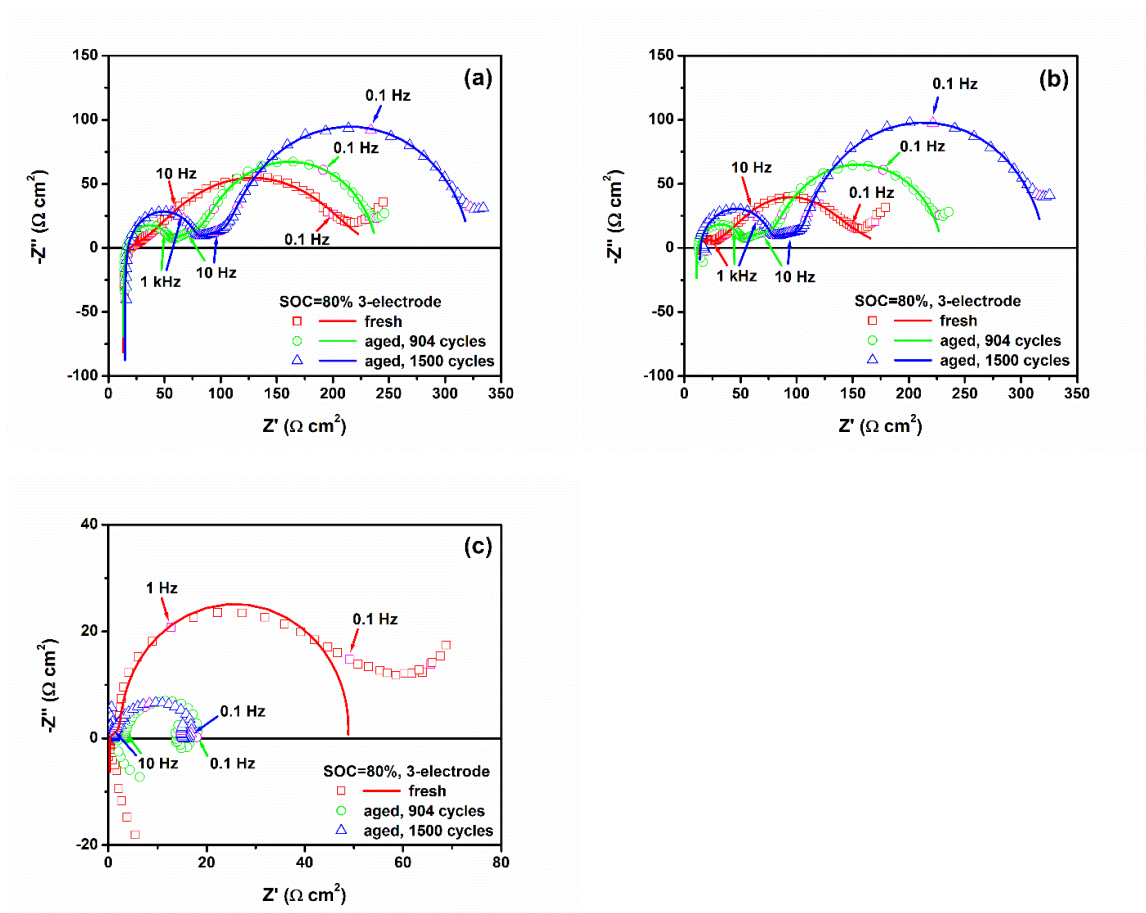
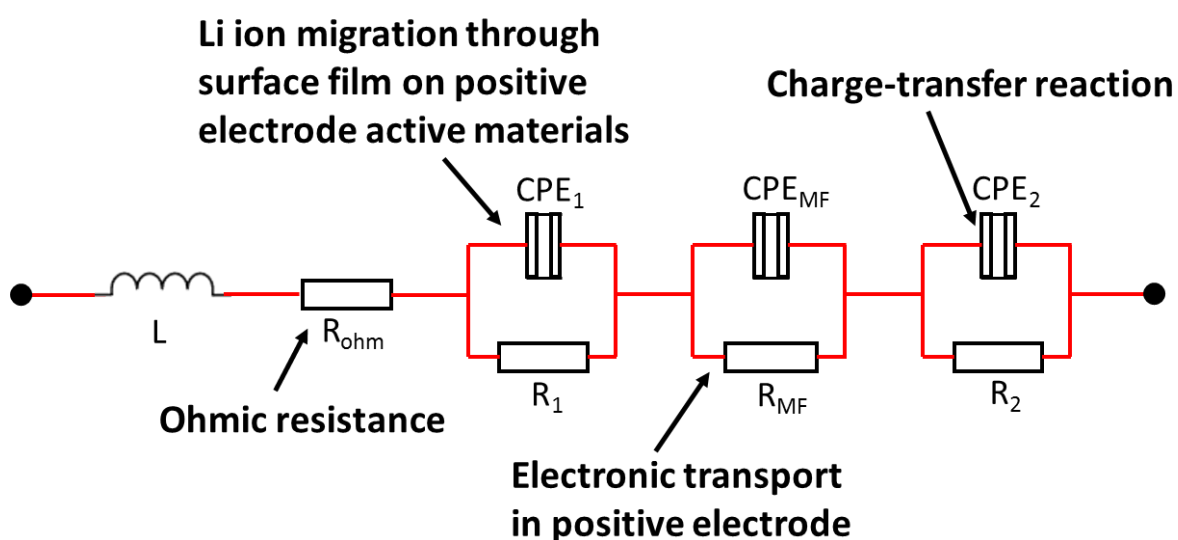


Figure 2-9. A comparison of (a) full cell, (b) positive electrode, and (c) negative electrode impedance measured at 80% SOC and -10 °C (symbols: experimental data, lines: fitted) in a three-electrode cell among a fresh and two aged cells at 904 and 1500 cycles.

(a) Cell and positive electrode



(b) Negative electrode

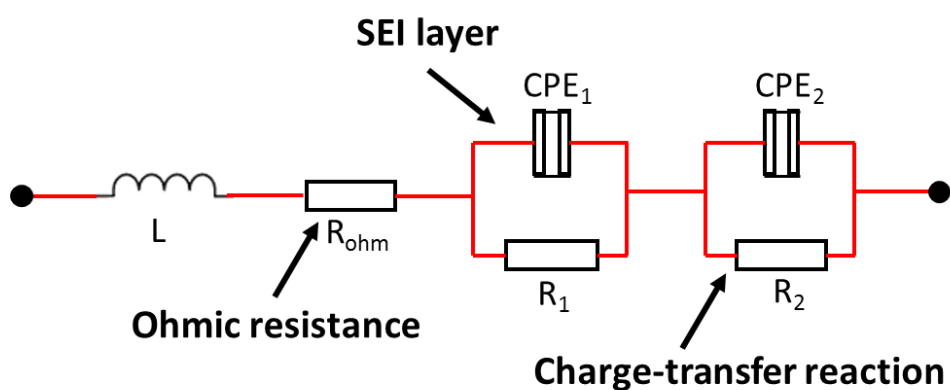


Figure 2-10. Equivalent circuits for (a) cell and positive electrode, and (b) negative electrode used to fit cell impedance spectra shown in Figure 2-9. (Note: Warburg diffusion impedance showing a short inclined line in the low frequency range isn't included in the equivalent circuits).

The impedance spectra of the full cell, positive and negative electrodes for a fresh and two aged cells at -10 °C (Figure 2-9) were fitted using above-mentioned equivalent circuits (Figure 2-10). The fitting parameter values are summarized in Table 2-IV. The total resistance of cell/positive electrode at -10 °C is dominated by charge-transfer resistance (R_2) rather than the resistance related to lithium ion migration through surface film (R_1), which is opposite to the case at 25 °C. At 25 °C (Figure 2-6 and Table 2-III), the resistance related to lithium ion migration through surface film/electronic transport dominates the total resistance, especially for aged cells. When temperature is lowered from 25 to -10 °C, the charge-transfer reaction kinetics at the electrodes becomes more sluggish, leading to a larger contribution of charge-transfer resistance to the total resistance of the cell/positive electrode. Moreover, for a fresh cell, the charge-transfer resistance of the full cell is much larger than that of positive electrode at -10 °C, which implies that both positive and negative electrode contribute the charge-transfer resistance of the full cell, which is also quite different from the case at 25 °C, in which the negative electrode shows little contribution to the charge-transfer resistance of the full cell (Figure 2-6). With lowering temperature from 25 to -10 °C, both of the charge-transfer resistances of the positive and negative electrodes significantly increase. However, due to their different activation energies related to charge-transfer process, the charge-transfer resistance of the negative electrode increases more significantly with decreasing temperature than that of the positive electrode, leading to higher contribution of the negative electrode to the charge-transfer resistance of the full cells at lower temperature.

Figure 2-11 shows the ohmic resistance R_{ohm} , the resistances (R_1 , R_{MF} and R_2) related to different processes, and total resistance of fresh and aged cells in the case of full cells and positive electrodes at -10 °C. In the case of positive electrode impedance at -10 °C, with

increasing cycle number from 0 to 1500 cycles, the total resistance of the positive electrode increased by $142 \Omega \text{ cm}^2$ (from 179 to $321 \Omega \text{ cm}^2$). With regard to the resistances related to difference processes on the positive electrode at -10°C , the effect of aging is different. For example, from 0 to 1500 cycles, charge-transfer resistance (R_2) increased $\sim 155 \Omega \text{ cm}^2$ (from 58.3 to $213.6 \Omega \text{ cm}^2$); and the resistance related to Li ion migration through the surface film (R_1) increased by $\sim 54 \Omega \text{ cm}^2$ (from 7.63 to $61.6 \Omega \text{ cm}^2$); while the electronic transport resistance (R_{MF}) decreased by $\sim 70 \Omega \text{ cm}^2$ (from 102.3 to $32.0 \Omega \text{ cm}^2$). The increase in the resistance related to Li ion migration through the surface film is a results of growth of the surface film on the positive electrode active materials. Clearly, the significant increase in both charge-transfer resistance and the resistance related to Li ion migration through the surface film on the positive electrode active materials are two main factors for the increase in total resistance of the positive electrode at -10°C . In the case of negative electrode impedance (Figure 2-9c and Table 2-IV), very surprisingly, the total resistance of the negative electrode at -10°C decreases by $\sim 32 \Omega \text{ cm}^2$ (from 48.8 to $16.9 \Omega \text{ cm}^2$) from 0 to 1500 cycles, which mainly comes from the decrease in its charge-transfer resistance. The decrease in the charge-transfer resistance on the negative electrode after aging may be related to the increase in electrochemical reaction area of negative electrode materials caused by the dramatic crack propagation of graphite negative electrode materials, which is consistent with the discharge performance of negative electrode in the three-electrode cell (Figure 2-4d and Table 2-I). At low temperatures such as -10°C , although the total resistance of the negative electrode decreases upon cycle aging, significant increase in the total resistance of the positive electrode upon aging leads to a great increase in the total resistance of the full cell. For example, from 0 to 1500 cycles, the total cell resistance at -10°C increased by $\sim 81 \Omega \text{ cm}^2$ (from 242.1 to $323.1 \Omega \text{ cm}^2$). Therefore, the power fade of the cell at low temperatures is mainly due to the impedance rise of positive electrode upon aging, especially the rising charge-transfer

resistance and the increasing resistance related to Li ion migration through the surface film on the positive electrode active materials. Zhang *et al.*¹⁷ investigated the aging behavior of Li-ion batteries with $\text{LiNi}_{0.8}\text{Co}_{0.15}\text{Al}_{0.05}\text{O}_2$ (NCA) positive electrode and graphite negative electrode and also found that the cell impedance rise comes mainly from the increase in the charge-transfer resistance and SEI layer resistance of the positive electrode.

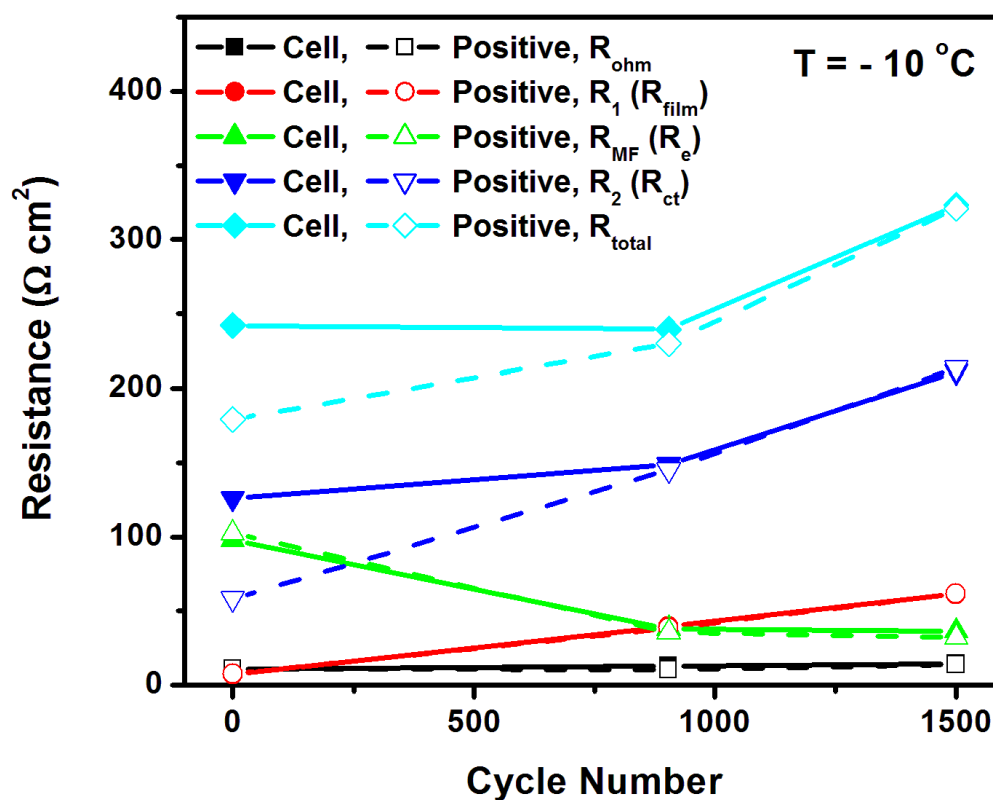


Figure 2-11. A comparison in the resistances related to different processes at -10°C between full cell (solid line + solid symbol) and positive electrode (dash line + open symbol) fitted from the impedance test data shown in Figure 2-9. (Note: impedance has been normalized based on total positive electrode area of 1055 cm^2).

Table 2-4. Fitting parameter values for the impedance spectra (excluding Warburg diffusion impedance) of a fresh and two aged cells (at 904 and 1500 cycles) measured at 80% SOC and -10 °C in a three-electrode cell shown in Figure 2-9.

Cycle No.	Fresh			Aged, 904 cycles			Aged, 1500 cycles			
	cell	positive	negative	cell	positive	negative	cell	positive	negative	
L (mH cm ²)	0.132	0.010	0.080	0.113	0.040	—	0.142	0.017	—	
R _{ohm} (Ω cm ²)	10.90	10.94	0.23	12.9	10.5	—	14.3	13.8	—	
R ₁ (Ω cm ²)	7.35	7.63	2.76	39.6	38.4	—	61.4	61.6	—	
CPE ₁	A ₁ (μF cm ⁻²)	2.06	1.00	9.73	1.83	1.89	—	1.55	1.27	—
	n ₁	1.025	1.098	0.658	0.958	0.961	—	0.963	0.977	—
R _{MF} (Ω cm ²)	97.9	102.3	—	38.1	35.7	—	36.3	32.0	—	
CPE _{MF}	A _{MF} (mF cm ⁻²)	6.01	4.48	—	2.16	1.69	—	1.95	1.31	—
	n _{MF}	0.313	0.358	—	0.571	0.609	—	0.586	0.654	—
R ₂ (Ω cm ²)	125.9	58.3	45.8	148.8	145.3	~13.7*	211.1	213.6	~15.8*	
CPE ₂	A ₂ (mF cm ⁻²)	1.85	1.48	6.17	6.63	7.85	—	6.11	6.81	—
	n ₂	0.754	0.904	1.056	0.915	0.915	—	0.920	0.939	—
R _{total} (Ω cm ²)	242.1	179.2	48.8	239.5	229.8	~18.1*	323.1	321.0	~16.9*	

* Estimated by ruler

2.3.6 A Comparison of Cell Performance Measured in Three- vs. Two-Electrode Cells

Figure 2-12 shows a comparison of the 1C charge-C/3 discharge performances of fresh and aged cells measured at room temperature ($\sim 23^\circ\text{C}$) between in two and three-electrode cells. There is almost no difference in the cell performance for a fresh cell and an aged cell at 904 cycles. However, for an aged cell at 1500 cycles, the cell shows better C/3 discharge performance when measured in the three-electrode cell than in the two-electrode cell. For the same aged cell, similar results on 1C discharge performance were observed (Figures 2-4a and 4b). In general, a lithium-ion pouch cell is sealed under vacuum during cell fabrication and thus it is compact for an as-fabricated fresh cell. For a fresh cell, the contact of cell components is very intimate to reduce the contact resistance between cell components. However, during cell aging, SEI layer at the graphite negative electrode continuously grows with cycling, leading to the loss of cyclable lithium and possible gas evolution due to the reaction of lithium and electrolyte solvents. In addition, for high energy NMC622/graphite pouch cells studied in this work, significant lithium plating during the final stage of cycle life test occurs, leading to severe capacity fade (Figure 2-3). The deposited lithium on the surface of graphite negative electrode may also react with electrolyte solvents to thicken the SEI layer on the negative electrode and produce more gases. Recently, Matasso *et al.*^{55, 56} reported that gases are produced for a commercial lithium-ion cell with LiCoO_2 /graphite electrode as products of the reduction of electrolyte solvents on the surface of negative electrode during SEI layer formation/growth and cracking formation/propagation, and identified that the gases generated during repeated cycling are CO , CO_2 , CH_4 , C_2H_6 , and C_3H_8 using gas chromatograph-mass spectrometry (GC-MS) analysis. For the aged cell at 1500 cycles, swelling of the pouch cell can be obviously observed by an eye and the gases produced inside the pouch cell can be easily detected by touch. A large amount of gas decreases the electrode stack

pressure, leading to the loss of the contact between cell components. Therefore, the aged cell at 1500 cycles shows much higher ohmic resistance than other aged cells at cycles of ≤ 1000 when measured in a two-electrode cell (Figure 2-5a). For a three-electrode cell, when the cell was assembled, the gases produced inside the pouch cell have been released and the pouch cell has been compressed by the setup. Moreover, the three-electrode pouch cells is soaked in a fresh electrolyte solution. Very interestingly, there is almost no change in the ohmic resistance among fresh and aged cells in a three-electrode cell (Figures 2-6a and 2-9a). Lowering the ohmic resistance and strengthening the contact between cell components from two- to three-electrode cell together with the use of a fresh electrolyte solution in three-electrode cell lead to an improvement in cell performance (discharge capacity and power) measured in a three-electrode cell.

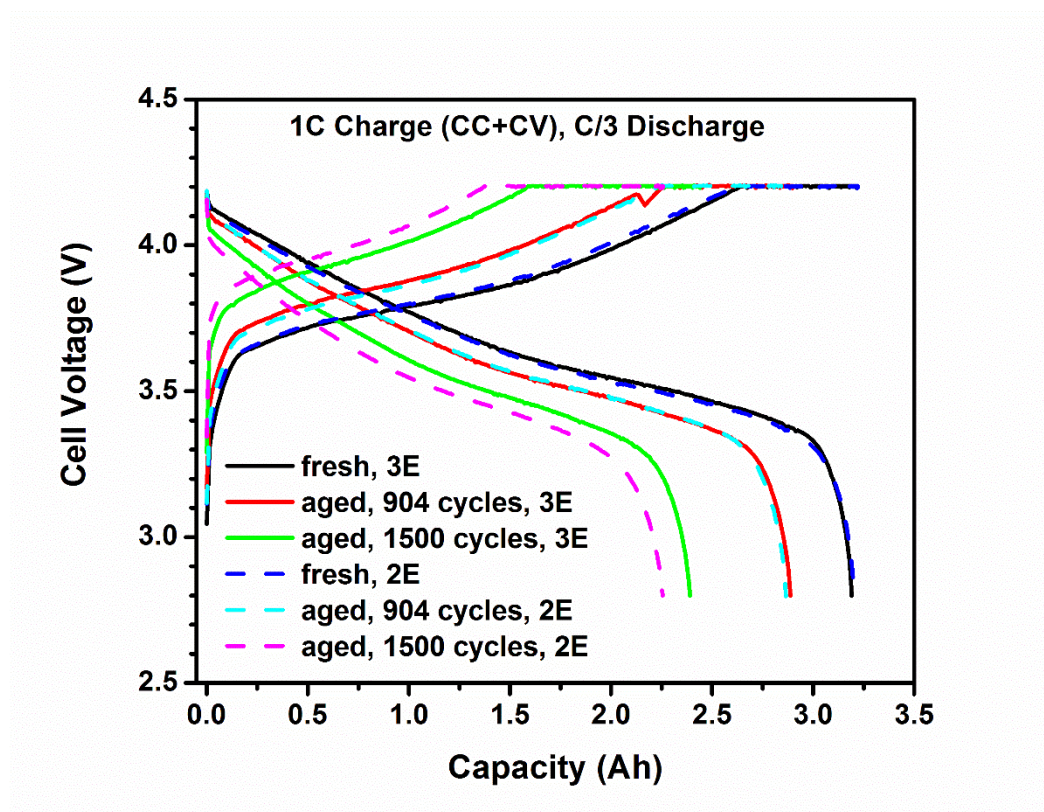


Figure 2-12. A comparison in 1C charge-C/3 discharge performance of fresh and aged cells measured at room temperature ($\sim 23^{\circ}\text{C}$) between in three-electrode (3E) (solid lines) and two-electrode (2E) (dash lines) cells.

2.4 Conclusions

Capacity and power fade during cycle-life testing at room temperature were examined for high energy lithium-ion pouch cells with thick NMC622 cathodes and thick graphite anodes. The cells experience significant capacity and power fade upon aging. The cells exhibits a cycle life of ~1419 cycles at capacity retention of ~75%. A number of factors may contribute to the capacity fade including the loss of cyclable lithium due to the growth of SEI layer, loss of active electrode materials and lithium plating. The power fade of the cell is mainly due to degradation of the positive electrode including the growth of surface film on the positive electrode active materials and the increase in charge-transfer resistance. In order to further improve cycle life of high energy NMC622/graphite lithium-ion batteries, it is necessary to avoid lithium plating and prevent rapid growth of SEI layer on graphite anode during repeated cycling, and increase stability of NMC622 electrodes and active materials.

2.5 References

1. T. H. Kim, J. S. Park, S. K. Chang, S. Choi, J. H. Ryu and H. K. Song, *Advanced Energy Materials*, **2**, 860 (2012).
2. W. Liu, P. Oh, X. Liu, M.-J. Lee, W. Cho, S. Chae, Y. Kim and J. Cho, *Angewandte Chemie-International Edition*, **54**, 4440 (2015).
3. H. J. Noh, S. Youn, C. S. Yoon and Y. K. Sun, *Journal of Power Sources*, **233**, 121 (2013).
4. C. Chae, H.-J. Noh, J. K. Lee, B. Scrosati and Y.-K. Sun, *Advanced Functional Materials*, **24**, 3036 (2014).
5. Y.-K. Sun, S.-T. Myung, B.-C. Park, J. Prakash, I. Belharouak and K. Amine, *Nature Materials*, **8**, 320 (2009).

6. A. Yamano, M. Morishita, M. Yanagida and T. Sakai, *Journal of the Electrochemical Society*, **162**, A1730 (2015).
7. P. Rozier and J. M. Tarascon, *Journal of the Electrochemical Society*, **162**, A2490 (2015).
8. J. Qian, W. A. Henderson, W. Xu, P. Bhattacharya, M. Engelhard, O. Borodin and J.-G. Zhang, *Nature Communications*, **6** (2015).
9. Z. Liang, D. Lin, J. Zhao, Z. Lu, Y. Liu, C. Liu, Y. Lu, H. Wang, K. Yan, X. Tao and Y. Cui, *Proceedings of the National Academy of Sciences of the United States of America*, **113**, 2862 (2016).
10. K. G. Gallagher, S. E. Trask, C. Bauer, T. Woehrle, S. F. Lux, M. Tschech, P. Lamp, B. J. Polzin, S. Ha, B. Long, Q. L. Wu, W. Q. Lu, D. W. Dees and A. N. Jansen, *Journal of the Electrochemical Society*, **163**, A138 (2016).
11. J. Choi, B. Son, M.-H. Ryou, S. H. Kim, J. M. Ko and Y. M. Lee, *Journal of Electrochemical Science and Technology*, **4**, 27 (2013).
12. H. Zheng, J. Li, X. Song, G. Liu and V. S. Battaglia, *Electrochimica Acta*, **71**, 258 (2012).
13. M. Broussely, P. Biensan, F. Bonhomme, P. Blanchard, S. Herreyre, K. Nechev and R. J. Staniewicz, *Journal of Power Sources*, **146**, 90 (2005).
14. J. Vetter, P. Novak, M. R. Wagner, C. Veit, K. C. Moller, J. O. Besenhard, M. Winter, M. Wohlfahrt-Mehrens, C. Vogler and A. Hammouche, *Journal of Power Sources*, **147**, 269 (2005).
15. A. Barre, B. Deguilhem, S. Grolleau, M. Gerard, F. Suard and D. Riu, *Journal of Power Sources*, **241**, 680 (2013).
16. T. Waldmann, N. Ghanbari, M. Kasper and M. Wohlfahrt-Mehrens, *Journal of the Electrochemical Society*, **162**, A1500 (2015).
17. Y. Zhang and C.-Y. Wang, *Journal of the Electrochemical Society*, **156**, A527 (2009).
18. Y. Zhang, C.-Y. Wang and X. Tang, *Journal of Power Sources*, **196**, 1513 (2011).
19. C. Snyder, C. Apblett, A. Grillet, T. Beechem and D. Duquette, *Journal of the Electrochemical Society*, **163**, A1036 (2016).
20. T. Waldmann, M. Wilka, M. Kasper, M. Fleischhammer and M. Wohlfahrt-Mehrens, *Journal of Power Sources*, **262**, 129 (2014).
21. M. Petzl, M. Kasper and M. A. Danzer, *Journal of Power Sources*, **275**, 799 (2015).
22. A. M. Grillet, T. Humplik, E. K. Stirrup, S. A. Roberts, D. A. Barringer, C. M. Snyder, M. R. Janvrin and C. A. Apblett, *Journal of the Electrochemical Society*, **163**, A1859 (2016).
23. M. Ecker, N. Nieto, S. Kaebitz, J. Schmalstieg, H. Blanke, A. Warnecke and D. U. Sauer, *Journal of Power Sources*, **248**, 839 (2014).
24. S. F. Schuster, T. Bach, E. Fleder, J. Müller, M. Brand, G. Sextl and A. Jossen, *Journal of Energy Storage*, **1**, 44 (2015).
25. K. Jalkanen, J. Karppinen, L. Skogstrom, T. Laurila, M. Nisula and K. Vuorilehto, *Applied Energy*, **154**, 160 (2015).

26. S.-H. Lee, C. S. Yoon, K. Amine and Y.-K. Sun, *Journal of Power Sources*, **234**, 201 (2013).
27. S. U. Woo, B. C. Park, C. S. Yoon, S. T. Myung, J. Prakash and Y. K. Sun, *Journal of the Electrochemical Society*, **154**, A649 (2007).
28. S.-T. Myung, H.-J. Noh, S.-J. Yoon, E.-J. Lee and Y.-K. Sun, *Journal of Physical Chemistry Letters*, **5**, 671 (2014).
29. H. Shi, X. Q. Wang, P. Y. Hou, E. L. Zhou, J. Guo, J. Zhang, D. G. Wang, F. X. Guo, D. W. Song, X. X. Shi and L. Q. Zhang, *Journal of Alloys and Compounds*, **587**, 710 (2014).
30. E. M. Erickson, H. Bouzaglo, H. Sclar, K.-J. Park, B.-B. Lim, F. Schipper, C. Ghanty, J. Grinblat, B. Markovsky, Y.-K. Sun and D. Aurbach, *Journal of the Electrochemical Society*, **163**, A1348 (2016).
31. Y.-K. Sun, Z. Chen, H.-J. Noh, D.-J. Lee, H.-G. Jung, Y. Ren, S. Wang, C. S. Yoon, S.-T. Myung and K. Amine, *Nature Materials*, **11**, 942 (2012).
32. C.-Y. Wang, G. Zhang, S. Ge, T. Xu, Y. Ji, X.-G. Yang and Y. Leng, *Nature*, **529**, 515 (2016).
33. C.-Y. Wang, T. Xu, S. Ge, G. Zhang, X.-G. Yang and Y. Ji, *Journal of the Electrochemical Society*, **163**, A1944 (2016).
34. E. Sarasketa-Zabala, F. Aguesse, I. Villarreal, L. M. Rodriguez-Martinez, C. M. Lopez and P. Kubiak, *Journal of Physical Chemistry C*, **119**, 896 (2015).
35. D. Aurbach, B. Markovsky, A. Rodkin, M. Cojocaru, E. Levi and H. J. Kim, *Electrochimica Acta*, **47**, 1899 (2002).
36. M. Klett, R. Eriksson, J. Groot, P. Svens, K. C. Hogstrom, R. W. Lindstrom, H. Berg, T. Gustafson, G. Lindbergh and K. Edstrom, *Journal of Power Sources*, **257**, 126 (2014).
37. S. S. Zhang, K. Xu and T. R. Jow, *Electrochimica Acta*, **49**, 1057 (2004).
38. Y. Ji, Y. Zhang and C.-Y. Wang, *Journal of the Electrochemical Society*, **160**, A636 (2013).
39. K. Shono, T. Kobayashi, M. Tabuchi, Y. Ohno, H. Miyashiro and Y. Kobayashi, *Journal of Power Sources*, **247**, 1026 (2014).
40. E. McTurk, C. R. Birkel, M. R. Roberts, D. A. Howey and P. G. Bruce, *Ecs Electrochemistry Letters*, **4**, A145 (2015).
41. I. Buchberger, S. Seidlmayer, A. Pokharel, M. Piana, J. Hattendorff, P. Kudejova, R. Gilles and H. A. Gasteiger, *Journal of the Electrochemical Society*, **162**, A2737 (2015).
42. J. C. Burns, A. Kassam, N. N. Sinha, L. E. Downie, L. Solnickova, B. M. Way and J. R. Dahn, *Journal of the Electrochemical Society*, **160**, A1451 (2013).
43. J. G. Xu, R. D. Deshpande, J. Pan, Y. T. Cheng and V. S. Battaglia, *Journal of the Electrochemical Society*, **162**, A2026 (2015).
44. J. A. Gilbert, J. Bareño, T. Spila, S. E. Trask, D. J. Miller, B. J. Polzin, A. N. Jansen and D. P. Abraham, *Journal of the Electrochemical Society*, **164**, A6054 (2016).
45. B. Stiaszny, J. C. Ziegler, E. E. Krauss, J. P. Schmidt and E. Ivers-Tiffée, *Journal of Power Sources*, **251**, 439 (2014).

46. R. Deshpande, M. Verbrugge, Y. T. Cheng, J. Wang and P. Liu, *Journal of the Electrochemical Society*, **159**, A1730 (2012).
47. T. Liu, A. Garsuch, F. Chesneau and B. L. Lucht, *Journal of Power Sources*, **269**, 920 (2014).
48. Y. S. Lee, K. S. Lee, Y. K. Sun, Y. M. Lee and D. W. Kim, *Journal of Power Sources*, **196**, 6997 (2011).
49. D. W. Dees, D. P. Abraham, W. Q. Lu, K. G. Gallagher, M. Bettge and A. N. Jansen, *Journal of the Electrochemical Society*, **162**, A559 (2015).
50. X. Y. Qiu, Q. C. Zhuang, Q. Q. Zhang, R. Cao, Y. H. Qiang, P. Z. Ying and S. G. Sun, *Journal of Electroanalytical Chemistry*, **688**, 393 (2013).
51. D. W. Dees, D. P. Abraham, W. Lu, K. G. Gallagher, M. Bettge and A. N. Jansen, *Journal of the Electrochemical Society*, **162**, A559 (2015).
52. Q. C. Zhuang, T. Wei, L. L. Du, Y. L. Cui, L. Fang and S. G. Sun, *Journal of Physical Chemistry C*, **114**, 8614 (2010).
53. X. Y. Qiu, Q. C. Zhuang, Q. Q. Zhang, R. Cao, Y. H. Qiang, P. Z. Ying and S. G. Sun, *Journal of Electroanalytical Chemistry*, **687**, 35 (2012).
54. M. Itagaki, N. Kobari, S. Yotsuda, K. Watanabe, S. Kinoshita and M. Ue, *Journal of Power Sources*, **135**, 255 (2004).
55. A. Matasso, D. Wong, D. Wetz and F. Liu, *Journal of the Electrochemical Society*, **161**, A2031 (2014).
56. A. Matasso, D. Wong, D. Wetz and F. Liu, *Journal of the Electrochemical Society*, **162**, A885 (2015).

Chapter 3

Utilizing Research-Type Lithium-Ion Batteries to Gain a Better Understanding of Lithium Plating

3.1 Motivation

The previous chapter elucidated some information about what degradation mechanisms can cause Li-ion batteries to die. Of particular interest is the mechanism of lithium plating on the graphite anode of these cells. This leads to a premature death of these high energy Li-ion cells and if this could be mitigated, then perhaps the cycle life of these cells could be extended. This chapter will seek to gain a better understanding of the lithium plating mechanism and what factor or factors are most critical to this issue.

3.2 Introduction

Lithium cyclability is affected by numerous aging phenomena that decrease battery performance over time. Some of the common mechanisms include side reactions, formation of interfacial layers (electrode/electrolyte reactions) leading to increased internal resistance, loss of active material in the electrodes, and loss of contact between the electrode and current collector [1]. The most commonly studied degradation mechanism, formation of the solid-electrolyte interface (SEI) layer, has been shown to grow in thickness as temperature increases [2-7]. It has also been shown that as temperature decreases, approaching 0 °C and below, a different aging mechanism becomes dominant [8]. The mechanism believed to be dominant at sub-zero

temperatures is lithium deposition on the surface of the graphite anode. This plated lithium not only consumes cyclable lithium, but can cause serious safety issues [9].

Lithium plating has been studied by various groups over the past decade including charging strategies [10], quantifying [11-13], suppression by surface modification [14], design parameters [15], material studies [16-20] and modeling [21, 22]. It is widely accepted that lithium plating can occur during high current charging, at high state-of-charge or overcharging, and charging at low temperatures [10]. Lithium plating occurs when the anode potential drops below 0 V Li/Li⁺, when the reduction of lithium ions to metallic lithium competes with the intercalation of lithium into graphite. Graphite is more susceptible to lithium plating because its operating potential when fully lithiated is around 0.1-0.2 V Li/Li⁺. During high current charging, increased overpotentials can cause the anode potential to drop into the window of favorable lithium plating, which can occur at temperatures greater than 0 °C. The same potentials can occur during charging at low temperatures due to reduction of intercalation kinetics [23]. Studies have shown that certain design considerations can be implemented to suppress any lithium plating [15, 21]. These studies show that if there is excess anode material, both in capacity and in footprint area, lithium plating is less likely to occur. Others have tried to suppress lithium plating by optimizing the charging process by using a higher C-rate until a set cutoff voltage, and then dropping to a lower current or constant voltage step [10]. This issue with this method is that it requires knowledge of the anode potential, which is not readily available except in a three-electrode setup.

When plating occurs and the cell is opened to the air, white specs are seen on the anode. The plated lithium can be partially reversible and oxidizes at potentials around 0.1 V higher than lithium deintercalation from the graphite, which results in a voltage plateau that precedes the normal discharge curve [12]. It is believed that this metallic lithium can also react with neighboring electrolyte molecules, thus forming an irreversible passivating layer around the anode particle causing both loss of cyclable lithium and an increase in overall cell resistance [10].

Lithium plating can also cause severe safety issues as well. Metallic lithium is known to form dendrites, which can grow long enough to penetrate the separator and cause a short circuit. If enough heat is generated during such an event, thermal runaway could be induced and a fire may occur. Fleischhammer *et al.* recently discovered using Accelerating Rate Calorimetry that cells that have undergone lithium plating (charging at -10 °C) exhibit significantly faster self-heating rates that start at lower temperatures. This significant increase in heat formation during thermal runaway presents a greater safety hazard than normal [9].

In this chapter we present work examining lithium plating on graphite anodes in lithium-ion batteries. We have designed and built baseline high-energy, baseline high-power and research- type 3 Ah $\text{Li}(\text{Ni}_x\text{Co}_y\text{Mn}_z)\text{O}_2$ /graphite pouch cells specifically designed to study lithium plating. These cells are cycled using an accelerated aging protocol and then characterized using a variety of experimental tests. We present results of the cycling of the research cells to determine if lithium plating is present and what effect temperature has on lithium plating and cycle life.

3.3 Experimental Methods

3.3.1 Development of Pouch Cells

In order to better study the effects that lithium deposition has on the performance and cycle life of lithium ion batteries, we first had to design and build both baseline cells and research type cells intended specifically for the study of lithium plating. Pouch cells were fabricated with a theoretical capacity around 3 Ah. Each type of cells would consist of a $\text{Li}(\text{Ni}_x\text{Co}_y\text{Mn}_z)\text{O}_2$ (Umicore) cathode on aluminum current collectors with graphite (Nippon Carbon) anodes on copper current collectors. The ratio (x:y:z) of metals used in the cathode was either 1:1:1 (NCM111) or 6:2:2 (NCM622). The electrolyte used in these cells was a 1.0 M lithium

hexafluorophosphate (LiPF₆) in an organic electrolyte of ethylene carbonate (EC) and ethyl methyl carbonate (EMC) in at 3:7 wt% ratio with +2% vinylene carbonate (VC) (BASF). A Celgard-2325 separator was used that has a thickness of 25 micrometers.

For the baseline cells, we fabricated high-energy (HE) type and high-power (HP) type cells. The HE design is based on allowing more capacity from the cell while the HP design is based on allowing more current from the cell, especially at lower SOC. The HE cells were built with thicker electrodes, ~75 micrometers for the anode with a loading of 12 mg/cm² and ~65 micrometers for the cathode with a loading of 19 mg/cm², while the HP cells were built with thinner electrodes, ~51.5 micrometers for the anode with a loading of 6 mg/cm² and ~48.3 micrometers for the cathode with a loading of 12 mg/cm². The design capacities for the HE111 and HE622 cells were both 3.3 Ah while the capacities for the HP111 and HP622 cells were 2.0 and 2.7 Ah. In each of these cells, the design N/P ratio, that is the ratio of capacity of the anode to the capacity of the cathode, was 1.2, and the anode stack lengths and widths were ~4 mm wider than the cathode stacks, which is standard manufacturing practice in order to prevent lithium deposition on the edges of the anode [24].

For the purpose of this study, we had to design and build cells that could accelerate the lithium deposition process no matter what the ambient temperature or the charging rate. The way that this was accomplished was we designed the anode to have a much smaller capacity than the standard cathode, thus promoting lithium plating in excess to intercalation in the graphite particles upon every charge cycle. For the research type cells (Res), the footprint areas of the anode and cathode stacks did not change, but the N/P ratio was lowered to 0.6. For these Res cells, the thick cathode from the HE cells was used along with the thin anode from the HP cells, causing a mismatch in design capacities. The cathode had a theoretical capacity of 4.67 Ah while the anode only had a theoretical capacity of 3.0 Ah.

The electrodes were fabricated at the Electrochemical Engine Center's battery manufacturing lab here at the Pennsylvania State University. These steps include mixing of the electrode active materials with a binder and conductive agent in a solvent. The resulting slurry is then spread on each side of the respective current collector and dried under heat and vacuum to remove the solvent. After this step, the roll of dried active material is cut into 8-10 inch sections and is then roll pressed until the desired thickness/porosity is reached.

From this point on, the sheets were sent to ECPower's fabrication facility where they were punched in the proper size and shape. These individual stacks were then placed into an automated stacker that was able to insert the separator into the correct position as well. Each stack of electrodes was then ultrasonic welded to the external tab, aluminum for cathode and nickel for anode, and placed in the pouch. The pouch was then sealed on all but 1 side and then placed in a dehumidified glove box to prepare for electrolyte filling. Once filled with the proper amount of electrolyte, the pouch was placed under vacuum so that the electrolyte could penetrate the pores of the electrodes. After this the pouch was sealed and the cells were removed from the glove box to run formation cycles. Once these cycles were complete, the pouch was sealed between a special gas collection section and the stack and was trimmed to remove such section. About 20 cells of each type were produced

3.3.2 Development of Diagnostic Tools

After the formation process, initial capacity and performance characterization tests (PCT) were performed for the fresh baseline cells at room temperature using a multi-channel Arbin system. This test consisted of a 1C (where C is the capacity of the cell) constant charge current (CC) followed by a constant voltage (CV) step. The cut-offs used for these steps were 4.2 V for CC and when the current dropped below $C/20$ for the CV step. After charging, there was a 30

minute rest period followed by a discharge and then another 30 minute rest period. For this test, five different discharge currents were used: C/3, 1C, 2C, 3C, and 5C, all at 25 °C. A Tenney environmental chamber was used to temperature control and the cut-off for discharge was 2.8 V. For the fresh Res cells, only one discharge current was used, C/3, so as not to age the cell further with lithium plating during a characterization step. These protocols were also used for aged cells to elucidate any capacity or power fade that occurred from aging. One fresh cell from each type of baseline cell was also chosen to perform a temperature-dependent rate study in which the cell was charged using the above protocol at 25 °C and then discharged using a 1C current at various temperatures (40, 0, -10, and -25 °C).

Aging tests were carried out in two phases. The first phase was for the baseline cells, in which 10 cells from each type were selected for cycling. The protocol consisted of cycling at room temperature with the following steps using either a multi-channel Arbin or multi-channel LAND system:

1. CC (1C) to 4.2 V
2. CV at 4.2 V until the current dropped below C/10
3. 5 minute rest
4. CC (2C discharge) to 2.8 V
5. 5 minute rest

This cycling protocol is a so-called accelerated aging measure, as the test time is shortened due to the 2C discharge. One cell of each type was stopped at pre-selected cycle numbers (50, 250, 500, 1000, etc.) and was then characterized using the above PCT and EIS protocols.

The second phase for the aging tests was for the Res cells. Because the anode capacity was only 60% of the cathode capacity, it would be unwise to use the full charge protocol that was used to the baseline cells, both from a time and safety perspective. Instead, the PCT data from

the fresh cells was analyzed to see at what voltage the desired charge capacity was reached, in this case 70% of the cathode capacity or 3.2 Ah. This value was chosen because it would provide sufficient excess lithium for plating upon cycling while not causing severe safety concerns. It was found that both NCM111 and NCM622 Res cells reached this value at 4.15 V. Therefore, the cycling protocol for the Res cells was modified as follows:

1. CC (1C = 3.2 A) to 4.15 V
2. 5 minute rest
3. CC (2C discharge) to 2.8 V
4. 5 minute rest

Unlike the baseline cells, where multiple cells were cycled at room temperature, here only 1 of each type of cell (NCM111/NCM622) was cycled at one of 5 °C, 15 °C or 35 °C. Each cell was stopped after a set number of cycles (5, 15, 50, etc.) and a PCT was run at room temperature, allowing ~4 hours for heat up or cool down. Once completed, the cells were placed back to continue cycling at the same temperature as before, again with a ~4 hour heat up or cool down. Cells were deemed to have reached end of life when their state-of-health (SOH), percent of aged capacity to fresh capacity, reached a predetermined value, typically 60-70%.

The last diagnostic tool that has been developed so far is use of a three-electrode diagnostic set-up. Here we have taken baseline cells, both fresh and those aged to critical points, and added a third, lithium metal electrode. This enables us to extract each electrodes contribution to both overall cell voltage and to EIS spectra. The set-up was based on a design previously developed by our group for 18650 cylindrical lithium-ion cells [25]. The cell is discharged to 2.7 V using a C/10 current and then is transferred into an argon filled glove box with water content at 0.1 ppm. One edge of the pouch is cut open, exposing the stack of electrodes wrapped in separator. The pouch cell is placed in a chamber in the bottom of the three-electrode set-up and fresh electrolyte is added until the opening is completely covered. On the top side of the set-up,

lithium metal is pressed around a flattened piece of copper wire and bent so that no electrolyte is able to touch the copper wire. There are also two terminals that protrude through the top of the set-up so that current and voltage may be measured from each electrode tab. The terminal wires are sealed with two O-rings and the main chamber is sealed with a rubber gasket so that the internal chamber of the set-up is isolated from outside air and moisture.

Three-electrode diagnostic tests were the same as with the two-electrode cells, that being 25 °C PCT, 1C performance at varying temperatures. The protocols for each of these tests were the same as the two-electrode. In order to determine if our results from the three-electrode tests were useful, we had to do a calibration of the data, that is, compare the three-electrode data to the previous two-electrode data for the same cell. The data for fresh and aged cells matched fairly well for both charge and discharge voltage versus capacity and for EIS data. The slight overage of capacity and voltage seen at high cycle number may be due to the fresh electrolyte replacing the aged electrolyte in that cell and this negating any effect that electrolyte decay would have on capacity and power fade.

3.4 Results and Discussion

We hypothesized that our Res cells would show obvious signs of lithium plating and that cells cycled at lower temperature would have a much shorter cycle life than those cycled at higher temperatures. One method to identify if lithium plating is present is to look at the subsequent discharge curve of a cell. Because lithium stripping is reversible and occurs with a near 0 V overpotential, if metallic lithium is present in the anode, there should be an upper voltage plateau at the beginning of discharge [12], as illustrated in Figure 3-1a. The Res discharge curve (C/3 at room temperature) shown is a representative curve of all fresh Res cells, no matter the cathode chemistry or temperature of cycling. The upper voltage is present for the Res cell due to lithium

dissolution back into the electrolyte during the process of lithium stripping, which occurs at a near constant voltage. Following this plateau, there is a ~ 0.15 V drop from the upper voltage plateau of metallic lithium to the expected normal operation of a baseline cell. From the three-electrode experiments performed on the baseline cells in the previous chapter, this is the approximate voltage of a fully charged graphite anode (Figure 3-2), indicating that there is an obvious transition from stripping of metallic lithium to that of lithium deintercalation from the graphite structure. Second, the width of the voltage plateau is expected to be proportionate to the amount of lithium that is deposited on the graphite [12]. As can be seen in Figure 3-1b, there is about 0.9 Ah of capacity taken up by lithium stripping. Taking the 3.7 Ah total capacity of this cell from the initial PCT, this leaves 2.8 Ah of capacity from lithium intercalated into the graphite, which is what would be expected from an anode with a 3 Ah theoretical capacity, as in our Res cells.

Figures 3-3a-c present the first 5 discharge cycles for the Res622 cells under the accelerated aging protocol at 5, 15 and 35 °C, respectively. No matter what temperature is represented, there is still the obvious upper voltage plateau at the beginning of discharge for at least the first cycle. For 5 and 15 °C, the plateau is ~ 0.6 Ah and for 35 °C it is ~ 0.4 Ah. The reason for the decrease in this as compared to Figure 3-1 is due to the higher overpotential from the increased discharge rate meaning that not all of the lithium will be able to be stripped before it becomes more favorable to remove lithium from the graphite. For 35 °C, the further shrinking of the voltage plateau is due to the metallic lithium reaction with and reducing the electrolyte due to the higher temperature thus forming more SEI and decreasing the amount of lithium available for stripping. The temperature plays a role in this as well as is seen in the disappearance of the voltage plateau as the cell increases in cycle number. This is due to faster SEI formation reaction kinetics and faster electrolyte diffusion through the SEI at increased temperatures. For 35 °C, the plateau is almost gone after 1 cycle and is completely gone after two cycles. For the colder

temperatures, the plateau is still visible through at least 4 cycles and is still visible at 5 °C through 5 cycles. As the amount of lithium being stripped is decreasing each cycle, we expect to see a drastic drop in cell capacity over the first 5 cycles at all temperatures, which will be shown later. Also, as the temperature is increased, the voltage of the deintercalation curves after lithium stripping increases. This is due to the decrease in Li diffusion resistance and increase in charge transfer kinetics, which lead to a lower cell resistance.

Another sign of lithium plating is a significantly lower coulombic efficiency for cells with lithium plating than cells without, especially at lower temperatures [8, 27]. Waldmann *et al.* report efficiencies of 0.975 for the first seven cycles at -20 °C, while achieving 0.999 efficiency at 25 °C [8]. The coulombic efficiencies for baseline and Res cells over the first five cycles are shown in Figure 3-4. There are two obvious trends seen here. The first is that lower temperatures provide lower coulombic efficiencies, as seen by the cells cycled at 5 °C (green lines) have on average a 10% lower CE than the cells cycled at 15 °C (blue lines). The second is that the Res cells have a much lower CE than the baseline cells. This is expected as the baseline cells are designed to protect against lithium plating while the Res cells are designed to promote lithium plating. It is interesting to note that the Res cells cycled at 35 °C (red lines) have nearly identical CE to the baseline cells (black lines). Because we already know from the discharge curves that these cells experience lithium plating, this must mean that most, if not all, of the plated lithium is stripped from the graphite during discharge.

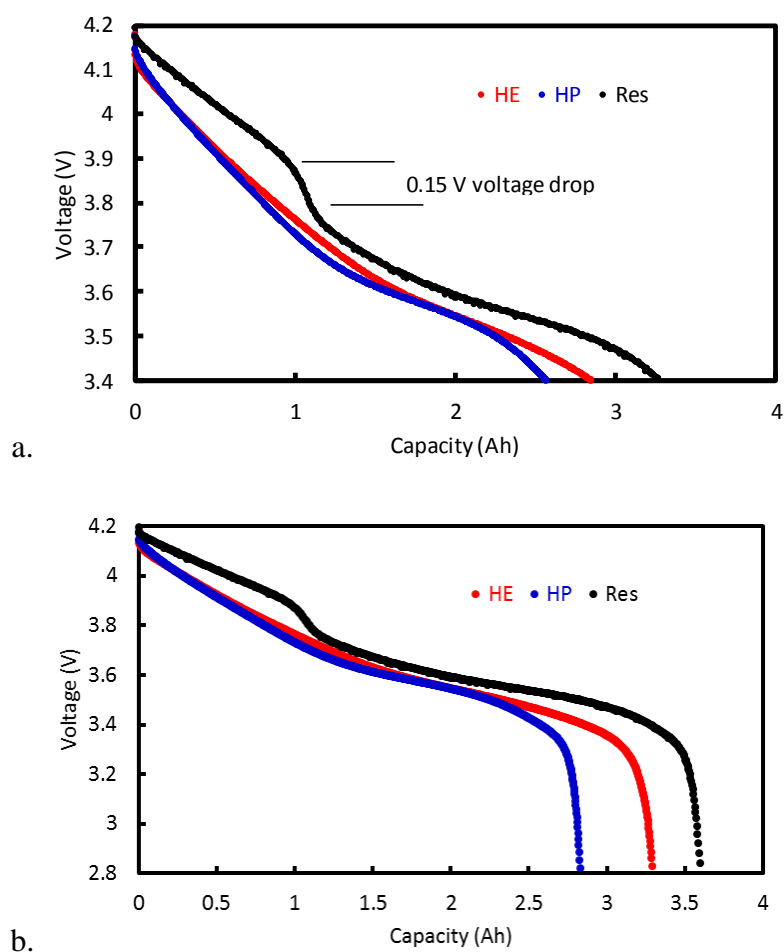


Figure 3-1. Comparison of baseline and research-type cells voltage-capacity C/3 discharge curves at RT showing (a) initial high voltage plateau and subsequent voltage drop for Res cells and (b) stripping of plated lithium allowing for "extra" capacity above nominal capacity for Res cells.

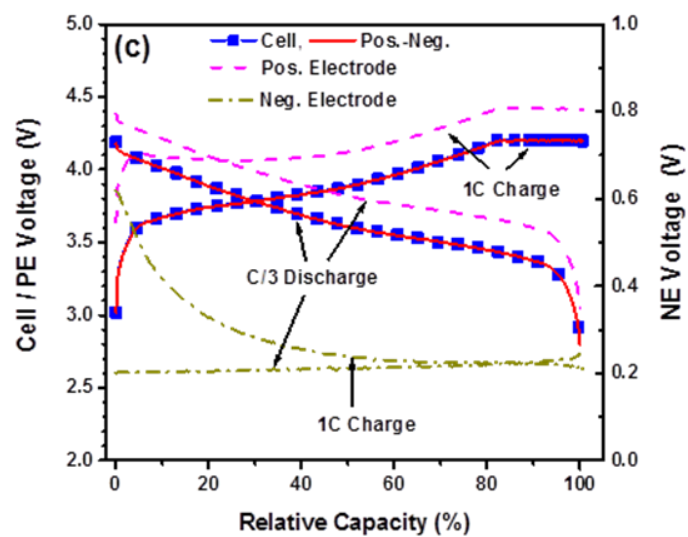
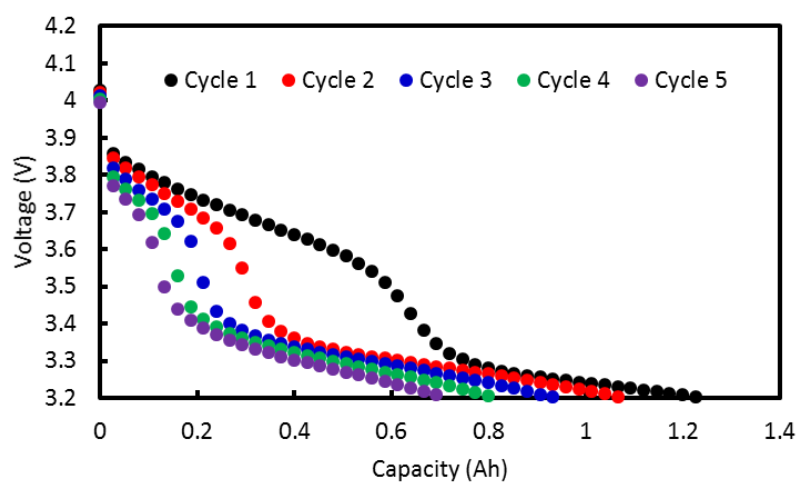


Figure 3-2. Results of three-electrode calibration for HE cells showing potentials of each electrode [26].



a.

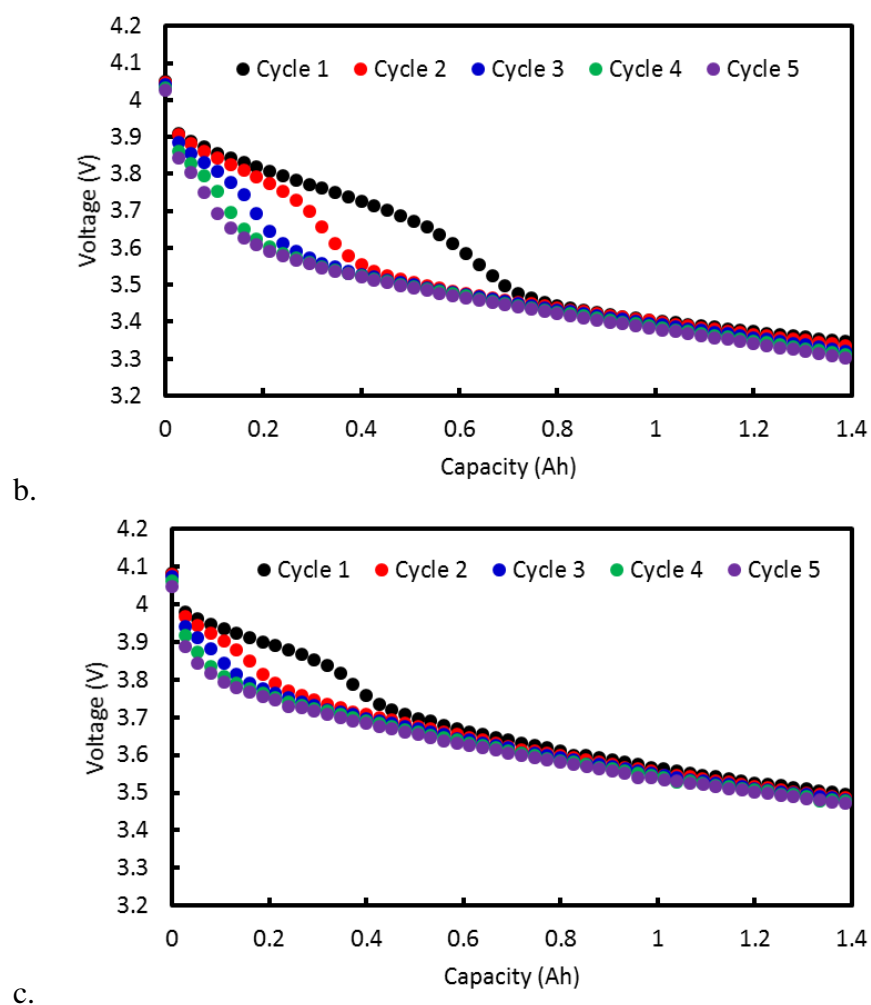


Figure 3-3. Discharge curves for first 5 cycles (2C discharge) for Res622 cells at (a) 5 °C, (b) 15 °C and (c) 35 °C.

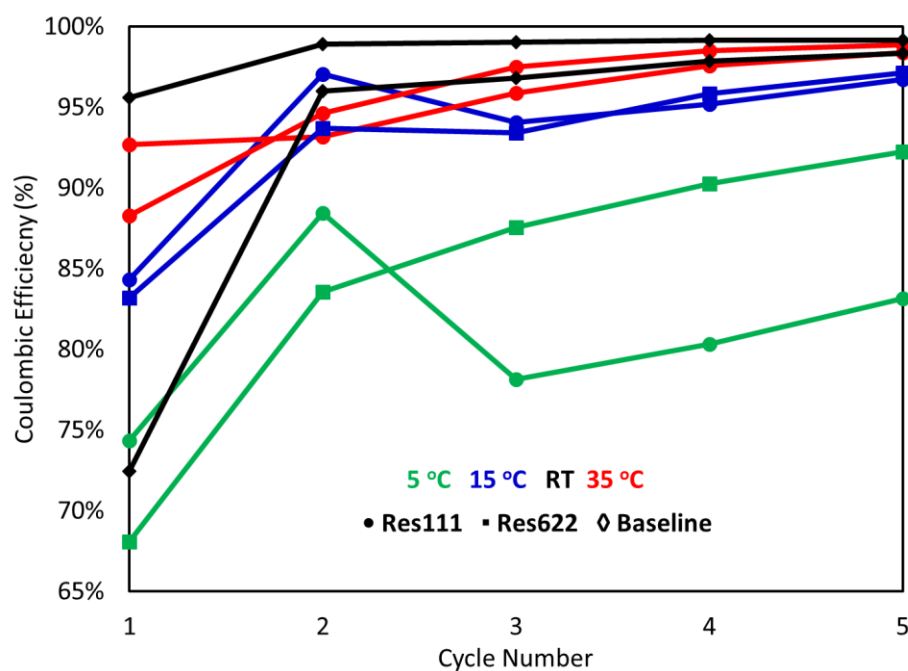


Figure 3-4. Coulombic efficiencies of baseline (RT) and Res cells for the first 5 discharge cycles during aging tests at various temperatures.

It is known that that lithium deposition on the anode consumes cyclable lithium [9], which causes capacity fade, but the plated lithium can also react with the electrolyte, which causes the SEI layer to grow and resistance to increase, leading to power fade. It is expected that the cells that are cycled at lower temperature will have a shorter cycle life, which is shown in Figure 3-5. The sharp drop initially is expected from what was seen in the first 5 cycles in Figure 3-3 as the upper voltage plateau diminishes and the amount of excess lithium is consumed. For 5 °C, lithium plating occurs so quickly and SEI formation occurs so slowly that too much lithium is consumed that the cell dies very quickly. For 15 and 35 °C, the increased formation of the SEI layer actually helps extend cycle life as it protects the surface from further lithium plating. At 15 °C, more lithium plating and slower SEI formation is expected which is shown in a larger decrease in initial SOH than at 35 °C.

Using an end-of-life criterion of 70% SOH, the cells cycled at 5 °C lasted about 4 cycles for both Res111 and Res622. In the case of the cells cycled at 15 °C, Res111 lasted about 50 cycles and Res622 lasted around 15 cycles. Finally, the cells cycled at 35 °C have not yet reached the end-of-life, having reached over 100 cycles. This goes to show that increasing a cell's operating temperature by as little as 10 °C can lead to an increase in cycle life from 4-12X, as seen in Table 3-I. And increasing a cell's operating temperature to the range expected in an electric vehicle's battery pack that is isolated from the ambient temperature can extend cycle life by well over 25X. This shows the importance of temperature control when it comes to potentially mitigating the threat of lithium deposition on graphite anodes.

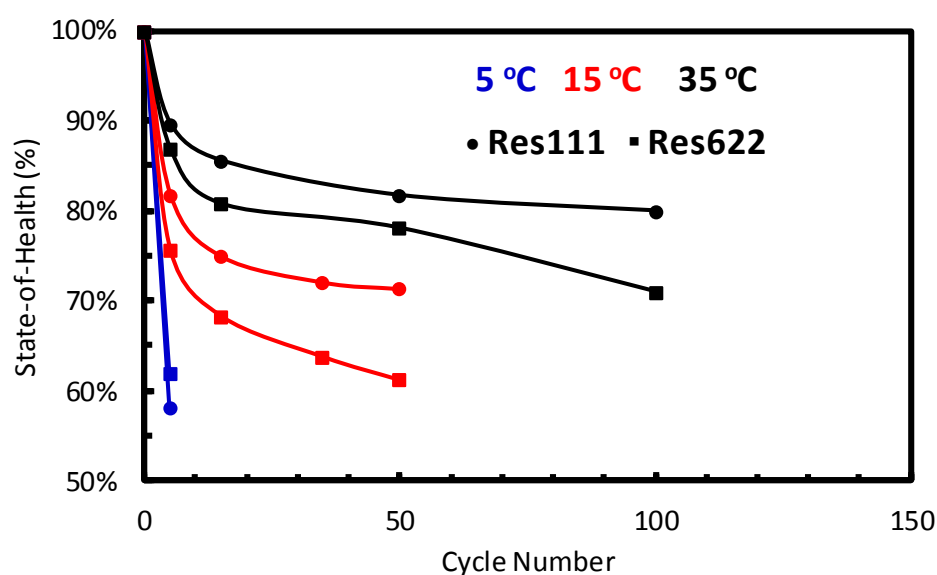


Figure 3-5. The effect of temperature on the aging of Res cells cycled at various temperatures.

Table 3-1. The temperature can have a drastic effect on the cycle life of a lithium-ion battery.

End-of-life at 70% SOH	Temperature change	Cycle life increase
Res111	5 °C – 15 °C	375%
Res622	5 °C – 15 °C	1250%
Res111	5 °C – 35 °C	2500%+
Res622	5 °C – 35 °C	2500%+

3.5 Conclusions

We have previously designed, built and tested baseline high-energy and high-power NCM111/graphite and NCM622/graphite lithium-ion pouch cells. These cells were designed with an average capacity of 3.3 Ah and 2.7 Ah, respectively, and an N/P ratio of 1.2, standard for the industry. Accelerated aging was carried out at room temperature using a CC-CV (1C-C/10) charge and 2C discharge. In order to better understand lithium plating, special research cells were designed and built to accelerate lithium deposition on the graphite anode using the same electrode materials as the baseline cells, but with an N/P ratio of 0.6. The research cells were cycled at 70% of the theoretical cathode capacity at either 5, 15, or 35 °C. We have developed a novel three-electrode setup as a tool to further investigate the aging mechanisms associated with lithium plating. In this setup, a lithium metal reference electrode is used to separate the contributions from the anode and cathode.

The results of the forced lithium plating study show that for all cells, lithium plating was present as seen in the upper voltage plateau at the beginning of discharge and by the significantly lower coulombic efficiencies over the first 5 cycles. A 0.15 V drop in cell potential during discharge was noticed for all cells, which is believed to be the transition point from lithium

stripping to lithium deintercalation from the graphite structure. For the cells cycled at 35 °C, the total capacity was 3.7 Ah and the width of the voltage plateau was ~0.9 Ah, indicating about 2.8 Ah coming from lithium in the graphite. This is the expected capacity of the anode with a theoretical capacity of 3.0 Ah. Finally, cycle life shows that cells cycled at 5 °C last no more than 5 cycles. In comparison, cells at 15 °C lasted 4-12x longer and cells at 35 °C lasted over 25x longer.

3.6 References

1. Arora, P., R.E. White, and M. Doyle, *Capacity fade mechanisms and side reactions in lithium-ion batteries*. Journal of the Electrochemical Society, 1998. **145**(10): p. 3647-3667.
2. Ploehn, H.J., P. Ramadass, and R.E. White, *Solvent diffusion model for aging of lithium-ion battery cells*. Journal of the Electrochemical Society, 2004. **151**(3): p. A456-A462.
3. Peled, E., *THE ELECTROCHEMICAL-BEHAVIOR OF ALKALI AND ALKALINE-EARTH METALS IN NON-AQUEOUS BATTERY SYSTEMS - THE SOLID ELECTROLYTE INTERPHASE MODEL*. Journal of the Electrochemical Society, 1979. **126**(12): p. 2047-2051.
4. Broussely, M., et al., *Aging mechanism in Li ion cells and calendar life predictions*. Journal of Power Sources, 2001. **97-8**: p. 13-21.
5. Peled, E., et al., *An advanced tool for the selection of electrolyte components for rechargeable lithium batteries*. Journal of the Electrochemical Society, 1998. **145**(10): p. 3482-3486.
6. Dubarry, M., et al., *Evaluation of commercial lithium-ion cells based on composite positive electrode for plug-in hybrid electric vehicle applications. Part II. Degradation mechanism under 2 C cycle aging*. Journal of Power Sources, 2011. **196**(23): p. 10336-10343.
7. Dubarry, M., et al., *Evaluation of Commercial Lithium-Ion Cells Based on Composite Positive Electrode for Plug-In Hybrid Electric Vehicle Applications III. Effect of Thermal Excursions without Prolonged Thermal Aging*. Journal of the Electrochemical Society, 2013. **160**(1): p. A191-A199.
8. Waldmann, T., et al., *Temperature dependent ageing mechanisms in Lithium-ion batteries - A Post-Mortem study*. Journal of Power Sources, 2014. **262**: p. 129-135.
9. Fleischhammer, M., et al., *Interaction of cyclic ageing at high-rate and low temperatures and safety in lithium-ion batteries*. Journal of Power Sources, 2015. **274**: p. 432-439.

10. Waldmann, T., M. Kasper, and M. Wohlfahrt-Mehrens, *Optimization of Charging Strategy by Prevention of Lithium Deposition on Anodes in high-energy Lithium-ion Batteries - Electrochemical Experiments*. Electrochimica Acta, 2015. **178**: p. 525-532.
11. Kramer, Y., et al., *A New Method for Quantitative Marking of Deposited Lithium by Chemical Treatment on Graphite Anodes in Lithium-Ion Cells*. Chemistry-a European Journal, 2015. **21**(16): p. 6062-6065.
12. Ratnakumar, B.V. and M.C. Smart, *Lithium Plating Behavior in Lithium-ion Cells*, in *Rechargeable Lithium-Ion Batteries*, M. Winter, et al., Editors. 2010, Electrochemical Soc Inc: Pennington. p. 241-252.
13. Birkenmaier, C., et al., *Lithium Plating on Graphite Negative Electrodes: Innovative Qualitative and Quantitative Investigation Methods*. Journal of the Electrochemical Society, 2015. **162**(14): p. A2646-A2650.
14. Gunawardhana, N., et al., *Suppression of lithium deposition at sub-zero temperatures on graphite by surface modification*. Electrochemistry Communications, 2011. **13**(10): p. 1116-1118.
15. Eberman, K., et al., *Material and Design Options for Avoiding Lithium-Plating during Charging*, in *Battery/Energy Technology*, Z. Ogumi, N.J. Dudney, and S.R. Narayanan, Editors. 2010, Electrochemical Soc Inc: Pennington. p. 47-58.
16. Smart, M.C. and B.V. Ratnakumar, *Effects of Electrolyte Composition on Lithium Plating in Lithium-Ion Cells*. Journal of the Electrochemical Society, 2011. **158**(4): p. A379-A389.
17. Lu, W.Q., et al., *Overcharge Effect on Morphology and Structure of Carbon Electrodes for Lithium-Ion Batteries*. Journal of the Electrochemical Society, 2012. **159**(5): p. A566-A570.
18. Park, G., et al., *The study of electrochemical properties and lithium deposition of graphite at low temperature*. Journal of Power Sources, 2012. **199**: p. 293-299.
19. Kwon, O.J.F., W.; Wang, C.Y. in *15th International Meeting on Lithium Batteries*. 2010. Montreal, Canada.
20. Schmitz, R., et al., *SEI investigations on copper electrodes after lithium plating with Raman spectroscopy and mass spectrometry*. Journal of Power Sources, 2013. **233**: p. 110-114.
21. Arora, P., M. Doyle, and R.E. White, *Mathematical modeling of the lithium deposition overcharge reaction in lithium-ion batteries using carbon-based negative electrodes*. Journal of the Electrochemical Society, 1999. **146**(10): p. 3543-3553.
22. Tang, M., P. Albertus, and J. Newman, *Two-Dimensional Modeling of Lithium Deposition during Cell Charging*. Journal of the Electrochemical Society, 2009. **156**(5): p. A390-A399.
23. Ji, Y., Y.C. Zhang, and C.Y. Wang, *Li-Ion Cell Operation at Low Temperatures*. Journal of the Electrochemical Society, 2013. **160**(4): p. A636-A649.
24. Stewart, S. and J. Newman, *Measuring the salt activity coefficient in lithium-battery electrolytes*. Journal of the Electrochemical Society, 2008. **155**(6): p. A458-A463.

25. Zhang, Y.C. and C.Y. Wang, *Cycle-Life Characterization of Automotive Lithium-Ion Batteries with LiNiO₂ Cathode*. Journal of the Electrochemical Society, 2009. **156**(7): p. A527-A535.
26. Leng, Y.J., et al., *Electrochemical Cycle-Life Characterization of High Energy Lithium-Ion Cells with Thick Li(Ni_{0.6}Mn_{0.2}Co_{0.2})O₂ and Graphite Electrodes*. Journal of the Electrochemical Society, 2017. **164**(6): p. A1037-A1049.
27. Downie, L.E., et al., *In Situ Detection of Lithium Plating on Graphite Electrodes by Electrochemical Calorimetry*. Journal of the Electrochemical Society, 2013. **160**(4): p. A588-A594.

Chapter 4

Pulse Self-Heating of a Self-Heating Lithium-Ion Battery

This chapter is submitted for publication to the Journal of Power Sources as Marple, D., Ge, S., Zhang, G., and Wang, C.Y. Pulse Self-Heating of a Self-Heating Lithium-Ion Battery.

4.1 Motivation

As seen in the previous chapter, temperature plays a vital role in the onset of lithium plating on the graphite anode of Li-ion batteries. If the temperature of the cell could be monitored and controlled prior to charging, then lithium plating could potentially be mitigated. Controlling the ambient temperature of the cell may be practical in a laboratory or indoor environment, but this is not practical for use in electric vehicles. A more practical method is to control the interior of the cell by heating the cell prior to use.

Previous efforts by our group have produced a viable way to internally heat a self-heating lithium ion battery (SHLB), also known as an All-Climate Battery (ACB), from sub-zero temperatures using a continuous heating current in which target internal cell temperatures are achieved quickly and with little energy consumed [1, 2]. A schematic of how a SHLB operates is shown in Figure 4-1 [3]. A nickel foil is embedded inside the cell with one end welded to the negative terminal and the other end extending outside of the cell to become the third, activation, terminal. A switch is placed between the positive and activation terminals and when connected, the cell self-discharges through the Ni foil which acts as a resistive heater. When the cell reaches its target temperature, usually a set value of the surface temperature, the switch is opened and the cell can be utilized normally through the standard terminals. With the entire Ni foil contained in the cell and no load flowing through an external circuit, the heat generated through this process is

very efficient at heating the cell. Although this protocol works well for heating cells from sub-zero temperatures for the purpose of utilizing the cell's energy during discharge, when heating cells to acceptable charging temperatures, some issues arise. Continuous heating to internal temperatures near room temperature tends to induce large temperatures near the Ni foil and can lead to overshooting the target temperature, wasting energy, due to lag of the heat to transfer from its generation source to the surface of the cell. This chapter looks to enhance this current method for heating a cell by pulsing the activation current which is hypothesized to lower the localized temperature by decreasing the effective activation current and minimizing overshoot by allowing rest time for heat to transfer through the cell.

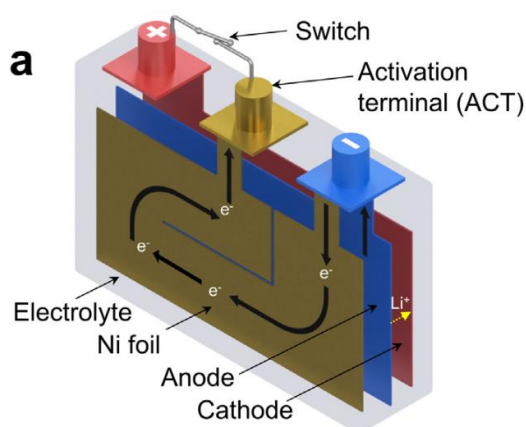


Figure 4-1. Working principle of a SHLB showing the cell structure including the embedded nickel foil and activation terminal [3].

4.2 Introduction

It is well known that electric vehicles driven in cold weather have drastically reduced driving range due to significant power loss in lithium ion batteries [4-7]. From a cell charging perspective, these temperatures do not allow for the use of regenerative braking [8-11] due to the

threat of lithium plating on the graphite anode which leads to capacity loss, cycle life decrease, and safety concerns. In order to combat these deficiencies, it is common practice to preheat the battery before use [12-18], which comes with its own set of issues including heating time, capacity consumed, and complex heating circuits [15, 17].

Our group recently developed an ACB which utilizes a SHLB structure. Here, a nickel foil is embedded in the cell and is utilized as an internal resistive heater allowing for rapid, uniform internal heating of the cell. Heating from $-20\text{ }^{\circ}\text{C}$ to $0\text{ }^{\circ}\text{C}$ consumes only 3.8% of cell capacity while taking just 20 seconds to heat the cell [2].

The heating protocol used for this heating is a continuous activation current until the cell reaches a target temperature of $0\text{ }^{\circ}\text{C}$. At this temperature, regenerative braking is still restricted so it is necessary to be able to heat the cell from temperatures above $0\text{ }^{\circ}\text{C}$ to near room temperature. Unfortunately, the previous method can lead to large spatial temperature gradients and overshoot of the target temperature. In order to mitigate this, more nickel foils can be added throughout the cell as investigated by [19], or by using pulse activation which does not add manufacturing complexities but instead requires precise control of on/off switching of the activation current. Here we examine pulse self-heating of an all climate battery in attempt to heat a battery from 0 to $20\text{ }^{\circ}\text{C}$ while lowering spatial temperature gradients, reducing energy consumption, and lowering average activation current while maintaining roughly the same heating time. We also determine the optimal length of each activation and rest time to heat the cell the most efficiently and effectively.

4.3 Experimental

Pouch cells (10 Ah) were fabricated using NMC622 ($\text{LiNi}_{0.6}\text{Mn}_{0.2}\text{Co}_{0.2}\text{O}_2$) for the cathode and Nippon Carbon graphite for the anode. The electrolyte for these cells was EC/EMC (3:7

wt%/wt%) + 2 wt% VC with 1M LiPF₆. The separator is a Celgard-2325 separator which is 25 micrometers thick. The nickel foil used had a resistance of 40 milliohms. More details can be found in our previous references [1, 3].

The ACB cell was first charged on a battery tester (BT2000, Arbin) using a CC-CV (1C-C/10) protocol to 4.2 V at room temperature (~23 °C). The cell was then placed in an environmental chamber (Tenney T10c, Thermal Product Solutions) held at 0 °C for a minimum of 6 hours to ensure thermal equilibrium within the cell. On the center of the outer surface of the cell, a T-type thermocouple (SA1-T, OMEGA Eng.) was positioned in order to obtain the surface temperature of the cell.

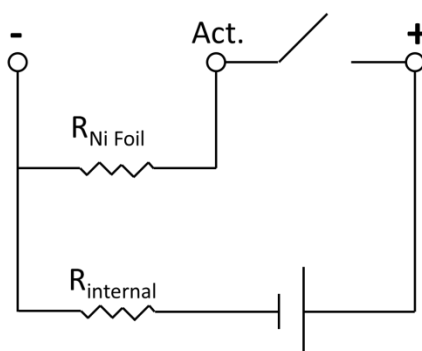


Figure 4-2. Electrical circuit showing the working principle of a self-heating lithium-ion battery.

The cell was connected to the battery tester such that it could act as the switch to engage the self-heating current by allowing the voltage between the positive and activation terminals to be 0 V, as seen in Figure 4-2. This allowed for collection of pertinent data, such as current and cell voltage, until the cell surface temperature reached 20 °C. Our current heating protocol, as discussed in our previous work [2], is a continuous activation “on” current until the cut-off temperature is reached. The pulse self-heating consists of a short on-pulse followed by a short rest off-pulse. For this study, 6 protocols were tested with the on pulse was 1 or 2 seconds and

the off pulse was 1, 2, 3 or 4 seconds. The six protocol presented in this work, given by x:y where x is the on pulse time and y is the off pulse time, are 1:1, 1:2, 2:1, 2:2, 2:3 and 2:4. After the activation was completed, a small current of 1 A was held through the nickel foil in order to monitor the foil resistance, determined by dividing the voltage measured across the activation and negative terminals by the current flowing through the foil. We then used a previous calibrated equation to extract the foil temperature, i.e. we use the foil as a resistance-temperature detector (RTD) [20].

In order to formulate the calibrated equation, the cell was soaked in an environmental chamber at one of five temperatures (-40, -20, 0, 20 and 40 °C) for at least 6 hours to ensure thermal equilibrium. A short (~5 sec), so as not to induce a temperature change from resistive heating, 1 A discharge current was run through the foil while the foil voltage was monitored. Foil resistance was obtained by dividing the foil voltage by the current at each data point and taking the average over the discharge. These 5 obtained resistance-temperature data points were linearly fit ($R^2 = 0.9983$) to obtain a calibrated equation.

The battery tester has a control accuracy of 0.02% and a voltage range of +/- 5 V, allowing for voltage measurements accurate to the nearest 1 mV. During self-heating, when the foil voltage is on the order of 3 V, this accuracy is not an issue and temperature curves are smooth. When heating stops and the 1 A current is flowing through the foil, the voltage drops to the order of 50 mV. This measurement accuracy leads a 2% noise in foil voltage measurement which then is amplified when converted to the temperature curves, hence why post-heating data presented will show fluctuations around the true value, while heating data will not.

4.4 Results and Discussion

The continuous heating protocol causes a voltage drop to below 3.4 V with a current of almost 8C as seen in Figure 4-3a. This high current produces enough heat to warm the cell, but it also causes an overshoot in temperature as seen in Figure 4-3b. The surface of the cell reaches 50.2 °C, an overshoot of 30.2 °C from the target temperature, meaning there is a large temperature gradient across the cell. These large temperature gradients raise issues of cell degradation and safety concerns due to localized hot spots. Also, the cell surface temperature rises to 26 °C, meaning that some of the cell's energy is wasted in raising the cell temperature past the target temperature.

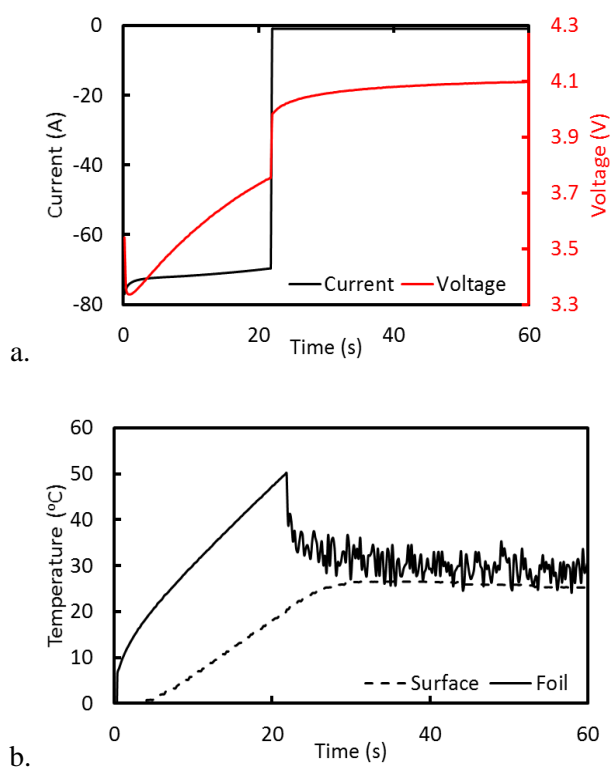


Figure 4-3. Performance of the continuous heating protocol showing (a) measured cell voltage and current (negative value means discharge) and (b) surface temperature measured by thermocouple and foil temperature measured by Ni foil as a resistance-temperature detector (RTD).

In order to mitigate these concerns, pulse heating was used to heat the cell where there was a short activation (on) pulse followed by a short rest (off) pulse. A comparison of the activation current for each pulse protocol and the continuous protocol are shown in Figures 4-4a-f. For all cases, the initial current was identical to that of the continuous case, and the activation current for each on pulse was nearly identical during the duration of the test with these currents being slightly more than the continuous protocol when the end of heating was reached. Though when the average current is calculated over the duration of heating, each of the pulse heating tests provide a lower average current than the continuous case, 2:1 ~33% lower, 2:1 ~50% lower and 2:4 ~75% lower, as shown in Figure 4-5. The trade off with the lower average current is longer heating time, though later it will be shown that this will be acceptable.

Figures 4-6a-f show the comparison of voltage from the pulse tests and the continuous test. Again, as with the current, the first pulse is nearly identical to the initial few seconds of the continuous test. As each pulsing test continues the voltage for the subsequent on pulses drops lower than that of the continuous test. This is expected due to the higher currents seen during the on pulses from the previous figures, though overall the voltage during each later pulse is higher than the previous pulse. This is due to the fact that as the cell heats up, internal cell resistance decreases causing a smaller voltage drop for the same activation current. Another interesting point is how the voltage during the off pulses recover to a lower voltage after each subsequent pulse, eventually ending at a voltage nearly identical to that of the continuous heating.

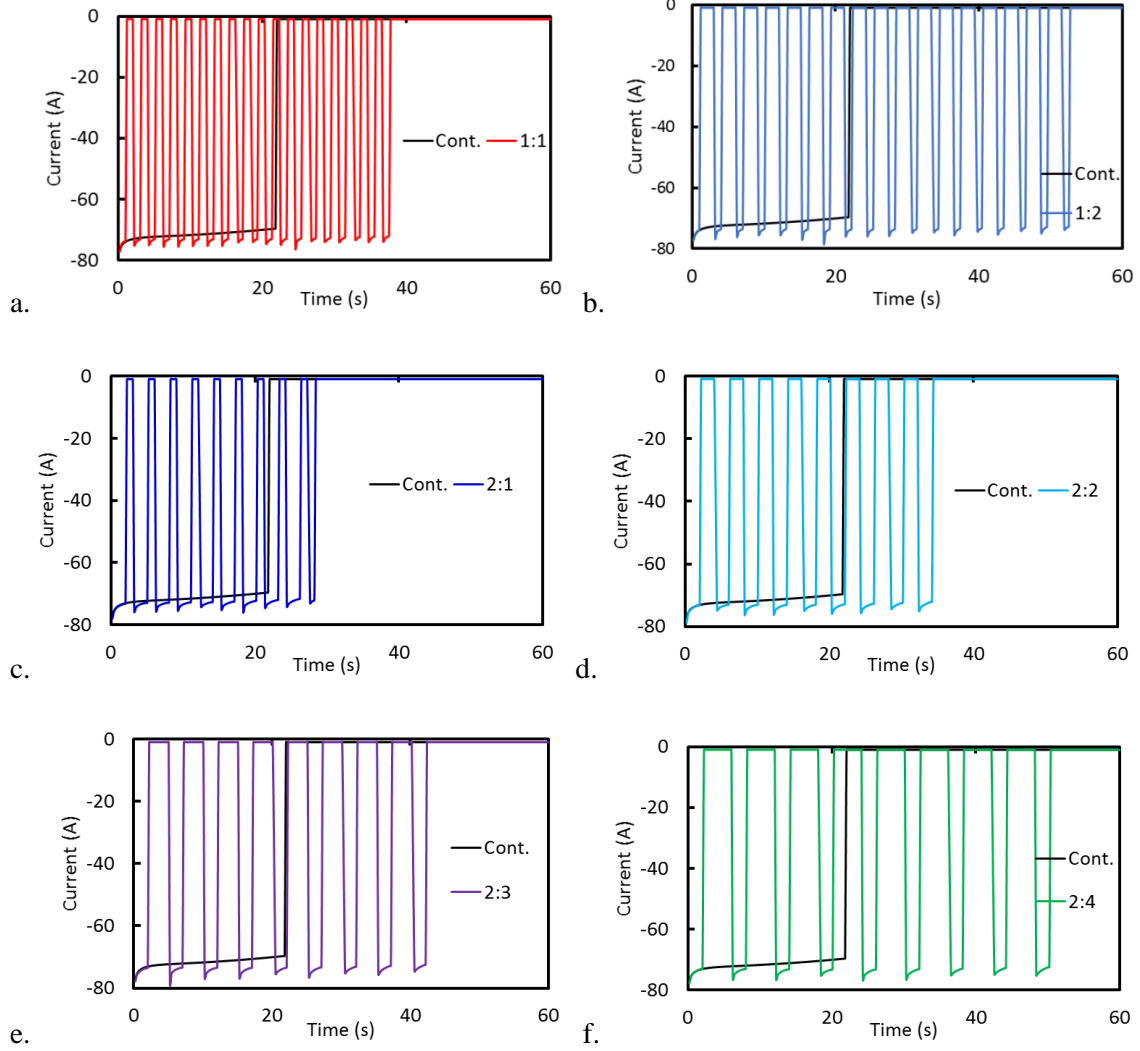


Figure 4-4. Measured activation current during self-heating comparing continuous heating and pulse heating cases (a)1:1, (b) 1:2, (c) 2:1, (d) 2:2, (e) 2:3 and (f) 2:4.

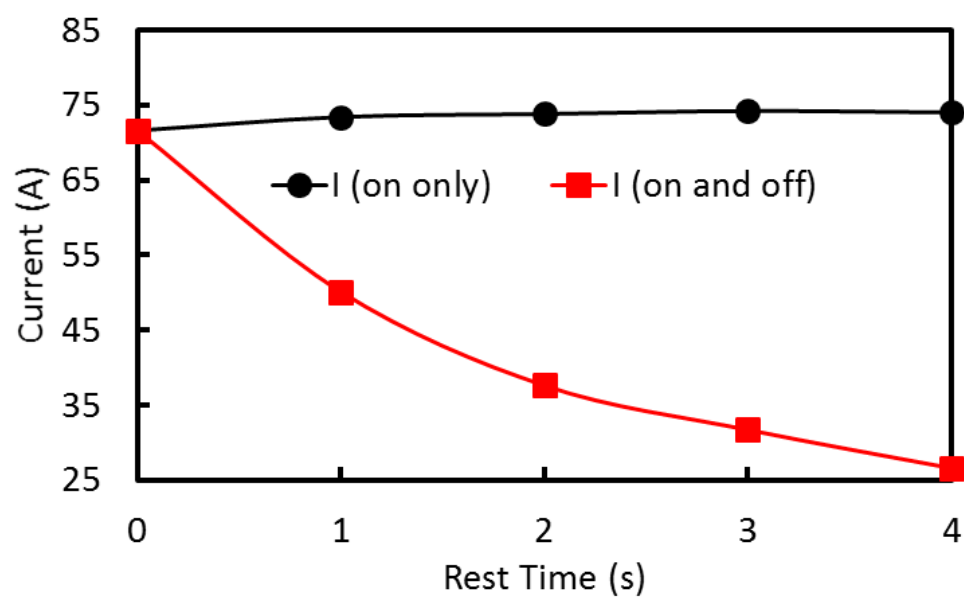


Figure 4-5. Average current measured for 2 second on time tests showing average activation current during on-pulses only (black) and over the duration of the test (red).

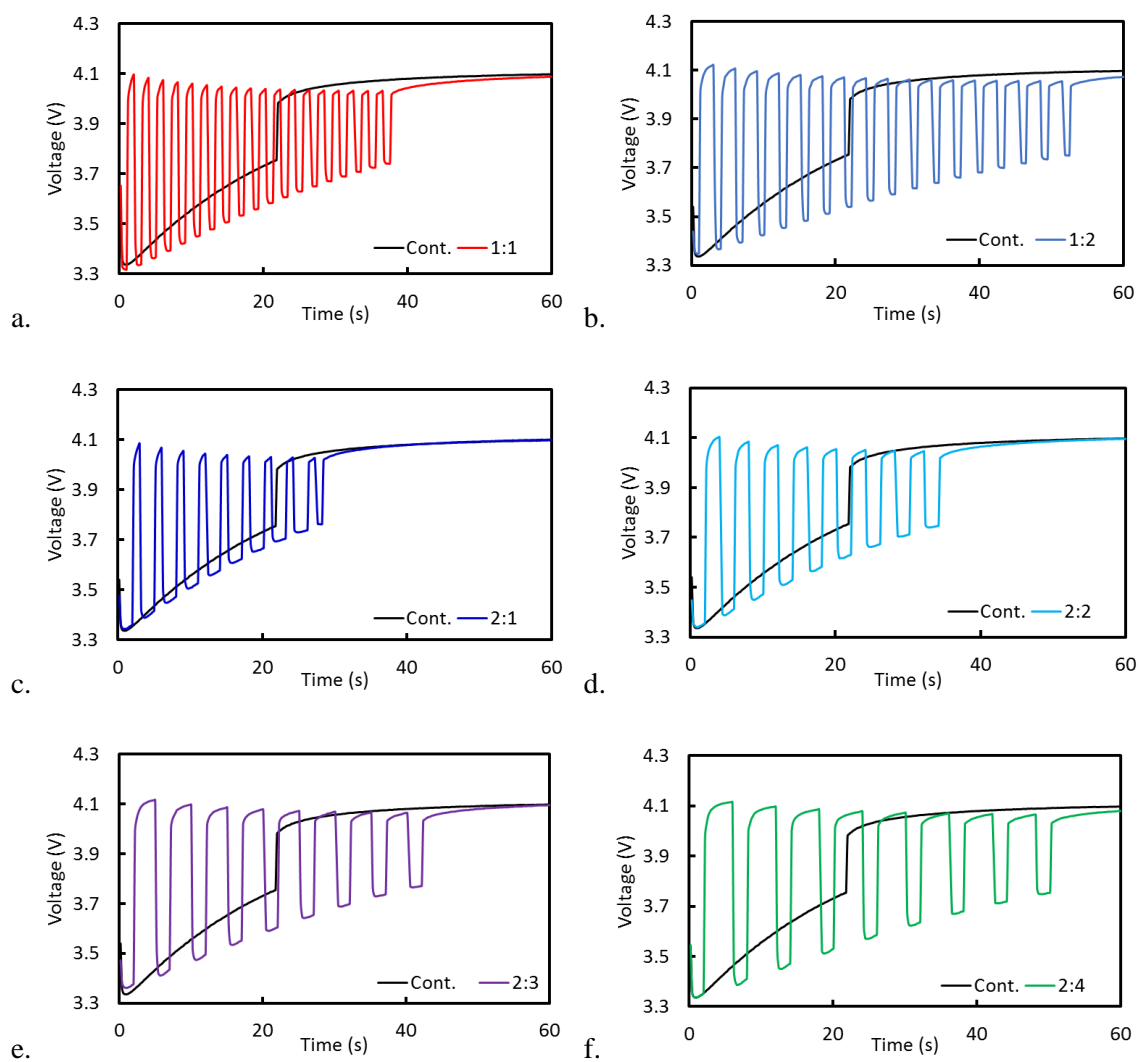


Figure 4-6. Measured cell voltage during self-heating comparing continuous heating and pulse heating cases (a) 1:1, (b) 1:2, (c) 2:1, (d) 2:2, (e) 2:3 and (f) 2:4.

With a lower average current used in each of the pulse heating cases, the effect on the temperature gradient in the cell needs to be examined. The foil and surface temperatures during the pulsing heating tests are shown in Figures 4-7a-f. Several conclusions can be gathered from these figures. First, the foil temperature shows peaks and valleys until the cell is heated. Each peak in temperature is due to the activation current generating heat while the immediate drop in temperature is due to heat conducting to the surrounding cooler material. Because the foil has such a low mass, this heat transfer is very fast. In fact, an approximate temperature of the surrounding materials during the off pulses can be gathered by looking at the temperatures of the valleys.

Second, as the rest time is increased, both the surface temperature overshoot and the off pulse temperature gradients are decreased. Looking at Figure 4-7c, with a rest time of 1 second the surface temperature overshoots by $\sim 4^{\circ}\text{C}$, while in Figure 4-7f, with a rest time of 4 seconds the overshoot is minimal meaning less energy is wasted in the 2:4 pulse test than the 2:1 test. Also, when comparing the same two figures, the difference between the surface and material near the foil (foil valley temperatures) increases from $\sim 2^{\circ}\text{C}$ to 10°C for a 1 second rest and increases from $\sim 1^{\circ}\text{C}$ to 5°C for a 4 second rest. This is because the longer rest time allows for more uniform heat distribution which minimizes temperature gradients and allows the cell to be closer to thermal equilibrium after each on pulse.

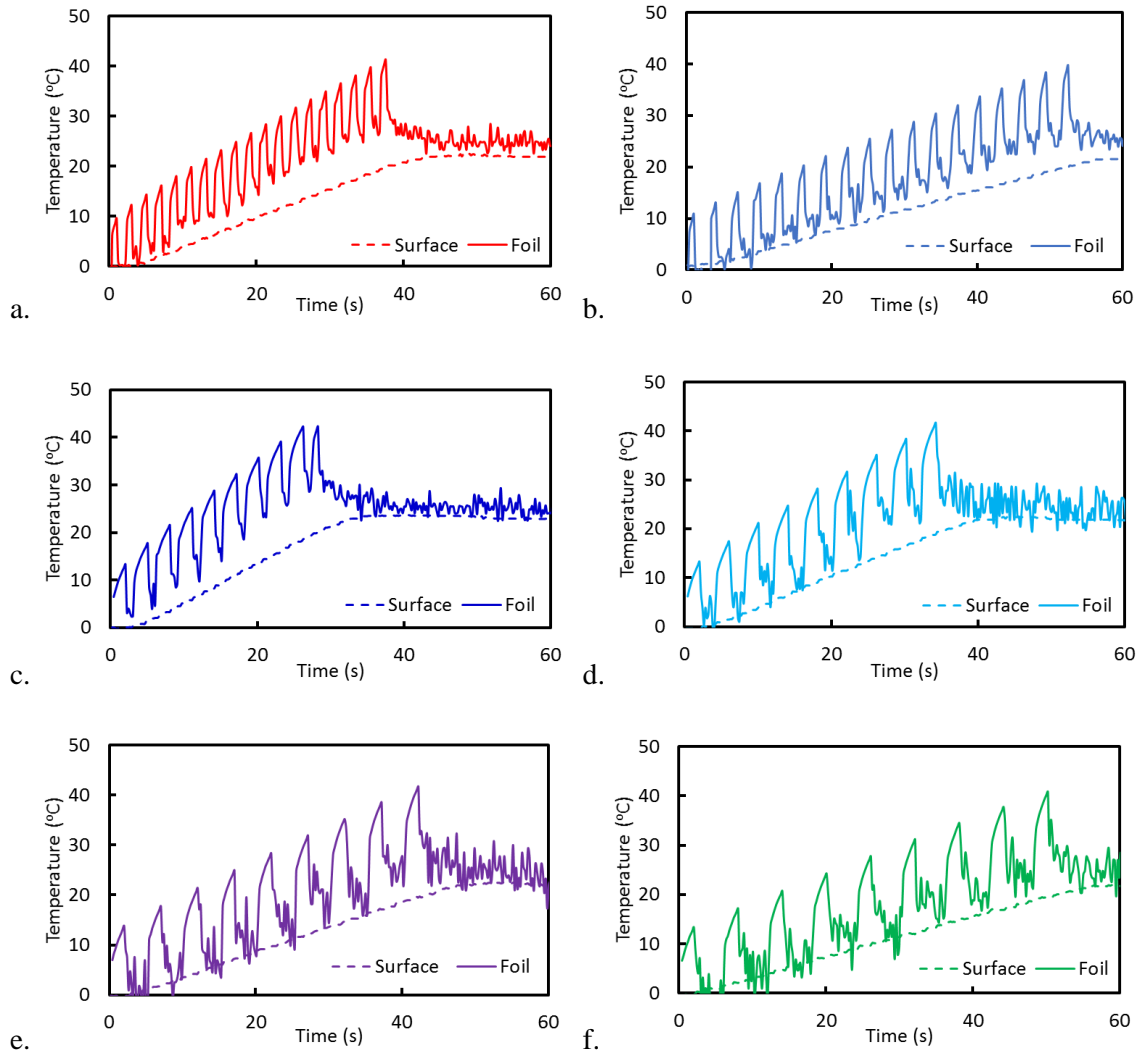


Figure 4-7. Evolution of surface and foil temperature during pulse self-heating cases (a)1:1, (b) 1:2, (c) 2:1, (d) 2:2, (e) 2:3 and (f) 2:4.

Last, when comparing pulse heating to continuous heating, the total temperature gradient is lower in all cases. The maximum temperature gradient occurs during the on peak of the last pulse. This occurs because the heat generated in the foil does not have sufficient time to conduct through the cell, so as each pulse produces excess heat, the foil temperature will rise at a slightly faster rate than the surface temperature. For all pulse heating cases, the maximum foil temperature was $\sim 42^{\circ}\text{C}$, indicating a total temperature gradient of 22°C , which is superior to that of the continuous heating.

Figure 4-8 compares the cell surface temperature evolution for each of the heating cases studied. Each heating protocol produced some surface temperature overshoot, though the continuous heating protocol produced the greatest overshoot. This means that the continuous heating wasted the most energy during the heating process. The pulse heating tests were able to heat the cell to the target temperature with less wasted energy than the continuous heating. It is interesting to note that both 1:1 and 2:2 produced the same surface temperature profile as well as 1:2 and 2:4. This implies that energy consumed depends on the ratio of the on and off pulses and not the length of each pulse.

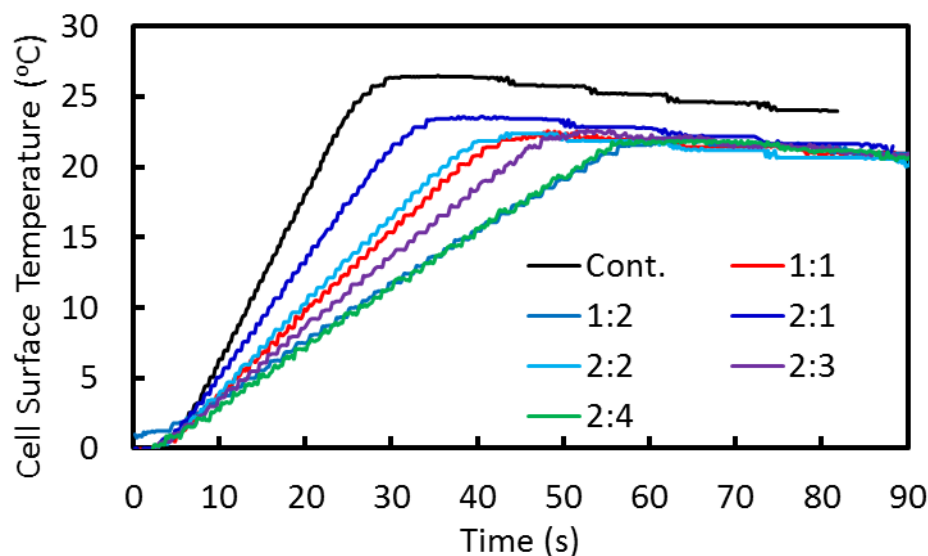


Figure 4-8. Evolution of surface temperature comparing continuous heating and pulse self-heating protocols.

It has been shown that pulse heating is able to lower the spatial temperature gradient, average activation current, and energy consumption, so the next step is to determine the optimal pulse heating protocol to utilize. Figures 4-9 look at determining the optimal rest time. When looking at the effect of rest time on maximum foil temperature, Figure 4-9a shows that all pulse heating cases show significantly lower values than continuous heating, but no further benefit is gained increasing the rest time past 2 seconds. The spatial temperature gradient in Figure 4-9b on the other hand shows there is some benefit to increasing rest time, ~ 0.5 °C/second of rest.

To further optimize the pulsing protocol, capacity consumed and heating time need to be examined. In Figure 4-10, these are compared for different off pulse times and on pulse times. When looking at the energy consumed, there is a minimum value of 3.8% reached for a 2 second off time for both the 1 second and 2 second on times. Combining this, with the results from above, a 2 second off time is optimal.

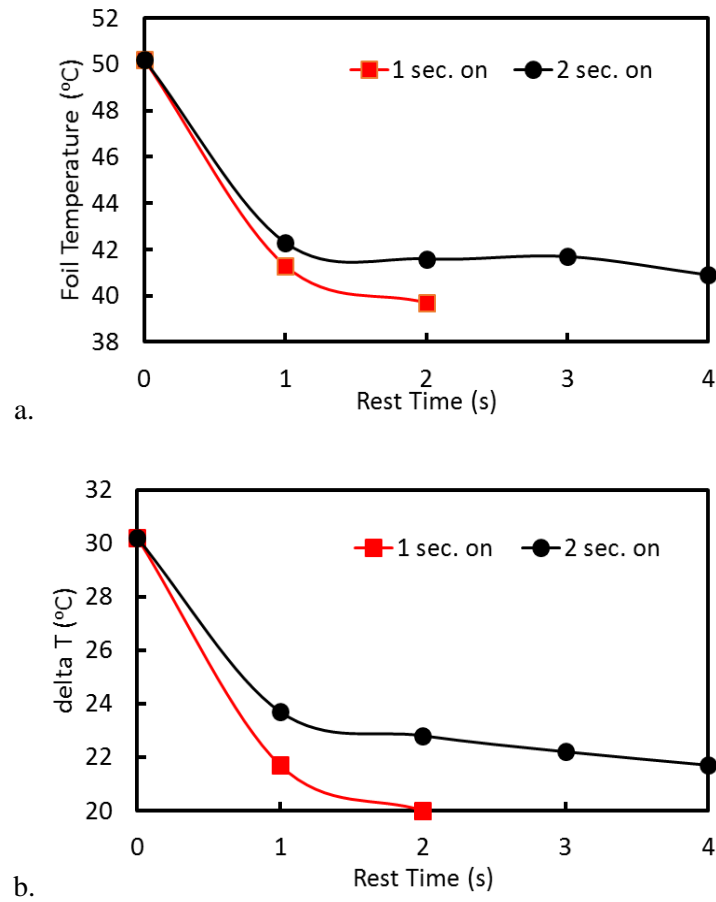


Figure 4-9. Effect of pulse rest time on (a) maximum foil temperature and (b) maximum spatial temperature gradient.

To determine the on pulse time, the total heating time has a major effect on this. As mentioned previously, because the average activation current is lowered for pulse heating, it is expected to have a longer heating time than continuous heating. For a 2 second rest time, an on pulse of 1 second yields a heating time of 52 seconds, an increase of 136%, while a 2 second on pulse yields a heating time of 36 seconds, an increase of only 63%. From this, a 2 second on pulse time will minimize the amount of extra time needed to heat the cell. Therefore, the optimal

heating strategy to lower spatial temperature gradients, lower energy consumed, and lower average activation currents while doing so in relatively the same time is a 2 second on, 2 second off pulse heating protocol.

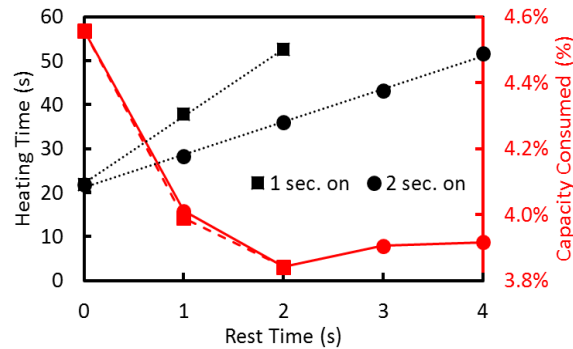


Figure 4-10. Self-heating time and capacity consumption for continuous and pulse self-heating.

4.5 Conclusions

Pulse heating of an all-weather battery was examined in order to minimize spatial temperature gradients, average activation current, and energy consumed when compared to the current heating protocol of continuous heating. Pulsing protocols consisted of an activation pulse of 1 or 2 seconds followed by a rest pulse of 1, 2, 3, or 4 seconds for heating a cell from 0 °C to 20 °C. The continuous heating showed a maximum foil temperature of 50 °C, comparing to the highest pulse heating of 42 °C. This leads to the maximum temperature gradient (foil to surface) for continuous heating to be 30 °C while the highest of any pulse heating was less than 24 °C. Not only was the spatial temperature gradient lowered by pulse heating, but so was the surface temperature overshoot, meaning continuous heating of the cell leads to wasted energy used to heat the cell above the target temperature.

The optimal pulse heating protocol is 2 seconds activations followed by 2 seconds rest.

The optimal rest time was determined by looking at the maximum foil temperature, maximum temperature gradient, and total energy consumed. The activation time was determined by minimizing the increase in heating time due to the lowering of the average activation current.

4.6 References

1. Wang, C.Y., et al., *A Fast Rechargeable Lithium-Ion Battery at Subfreezing Temperatures*. Journal of the Electrochemical Society, 2016. **163**(9): p. A1944-A1950.
2. Wang, C.Y., et al., *Lithium-ion battery structure that self-heats at low temperatures*. Nature, 2016. **529**(7587): p. 515-8.
3. Zhang, G.S., et al., *Rapid self-heating and internal temperature sensing of lithium-ion batteries at low temperatures*. Electrochimica Acta, 2016. **218**: p. 149-155.
4. Valoen, L.O. and J.N. Reimers, *Transport properties of LiPF₆-based Li-ion battery electrolytes*. Journal of the Electrochemical Society, 2005. **152**(5): p. A882-A891.
5. Lin, H.P., et al., *Low-temperature behavior of Li-ion cells*. Electrochemical and Solid State Letters, 2001. **4**(6): p. A71-A73.
6. Ji, Y., Y.C. Zhang, and C.Y. Wang, *Li-Ion Cell Operation at Low Temperatures*. Journal of the Electrochemical Society, 2013. **160**(4): p. A636-A649.
7. Huang, C.K., et al., *The limits of low-temperature performance of Li-ion cells*. Journal of the Electrochemical Society, 2000. **147**(8): p. 2893-2896.
8. Zhang, S.S., K. Xu, and T.R. Jow, *The low temperature performance of Li-ion batteries*. Journal of Power Sources, 2003. **115**(1): p. 137-140.
9. Waldmann, T., et al., *Interplay of Operational Parameters on Lithium Deposition in Lithium-Ion Cells: Systematic Measurements with Reconstructed 3-Electrode Pouch Full Cells*. Journal of the Electrochemical Society, 2016. **163**(7): p. A1232-A1238.
10. Ouyang, M.G., et al., *Low temperature aging mechanism identification and lithium deposition in a large format lithium iron phosphate battery for different charge profiles*. Journal of Power Sources, 2015. **286**: p. 309-320.
11. Petzl, M., M. Kasper, and M.A. Danzer, *Lithium plating in a commercial lithium-ion battery A low-temperature aging study*. Journal of Power Sources, 2015. **275**: p. 799-807.
12. Zuniga, M., et al., *Heating Lithium-ion Batteries with Bidirectional Current Pulses*. 2015 Ieee Vehicle Power and Propulsion Conference (Vppc), 2015.

13. Ge, H., et al., *Temperature-Adaptive Alternating Current Preheating of Lithium-Ion Batteries with Lithium Deposition Prevention*. Journal of the Electrochemical Society, 2016. **163**(2): p. A290-A299.
14. Zhang, J.B., et al., *Internal heating of lithium-ion batteries using alternating current based on the heat generation model in frequency domain*. Journal of Power Sources, 2015. **273**: p. 1030-1037.
15. Ji, Y. and C.Y. Wang, *Heating strategies for Li-ion batteries operated from subzero temperatures*. Electrochimica Acta, 2013. **107**: p. 664-674.
16. Song, H.S., et al., *Experimental Study on the Effects of Pre-Heating a Battery in a Low-Temperature Environment*. 2012 Ieee Vehicle Power and Propulsion Conference (Vppc), 2012: p. 1198-1201.
17. Stuart, T.A. and A. Hande, *HEV battery heating using AC currents*. Journal of Power Sources, 2004. **129**(2): p. 368-378.
18. Zhu, J.G., et al., *An alternating current heating method for lithium-ion batteries from subzero temperatures*. International Journal of Energy Research, 2016. **40**(13): p. 1869-1883.
19. Yang, X.G., T. Liu, and C.Y. Wang, *Innovative heating of large-size automotive Li-ion cells*. Journal of Power Sources, 2017. **342**: p. 598-604.
20. Figliola, R.S.B., D.E., *Theory and Design for Mechanical Measurements*. 1995, Wiley and Sons. p. 328.

Chapter 5

External vs. Internal Heating for Large-Format Automotive Lithium-Ion Batteries

This chapter is submitted for publication to the Journal of Power Sources as Marple, D., Zhang, G., Ge, S., and Wang, C.Y. External vs. Internal Heating for Large-Format Automotive Lithium-Ion Batteries.

5.1 Motivation

Until now, the cells we have examined have been on the laboratory scale and not the industrial electric vehicle scale. Mitigating lithium plating on this large scale is of extreme interest because automotive manufacturers are looking for ways to improve the energy density of their cells while also extending the life of their cells, leading to more attractive warranty options for consumers. In order to achieve this goal, the temperature of the battery pack in the vehicle must be able to be manipulated.

Until this point, the current industry practice for heating electric vehicle batteries is to utilize external heaters to heat the cell from the outside-in. This method can work for small-format cells, but will run into issues of large temperature gradients, slow heating times, and possible non-uniform degradation across the thickness of a large-format cell. We propose that use of the SHLB technology for this application will remedy these deficiencies while being able to heat the cell quickly and efficiently. This chapter examines the use of internal self-heating for heating large-format automotive lithium ion batteries that will become a cure for mitigating lithium plating in industrial electric vehicle cells.

5.2 Introduction

Lithium-ion batteries are a prevailing source of energy storage perfectly suited for many electronic devices because of their high power densities and high energy densities [1, 2]. They have also become the battery of choice to be employed in many electric vehicles. Several issues need to be resolved, including attaining a long lifetime (minimum 10 years [3]), being able to undergo fast charging [4], and improving performance at low temperatures [5], in order for this industry to really take off..

Aiming for increased energy density and reliability and decreasing cost, the automotive industry is shifting towards using a small number of larger capacity cells [6]. The trade-off to this comes in the thermal management side, where the cell needs heated in sub-zero environments due to the poor performance of Li-ion batteries in this temperature range [7-9]. Current heating methods allow for heating externally through the cell, relying on heat conduction to warm the interior of the cell. This can lead to non-uniform heating of the cell which in turn can cause non-uniform aging across the cell.

While there are many other heating options that can be utilized [10], one method recently discovered by our group is a self-heating lithium ion battery (SHLB), in which nickel foils are placed internally in the cell and act as resistive heaters [11, 12]. This technology has shown that the heating is rapid, efficient, and uniform. In the present work, we aim to show that for large-format automotive batteries (~40 Ah), internal heating using the SHLB technology is not only more energy-efficient, but also more effective, in terms of heating time, than external heating strategies. Moreover, we will show that heating a cell this large externally can lead to safety issues.

5.3 Experimental

5.3.1 Fabrication of Pouch Cells

Self-heating lithium ion pouch cells were fabricated with a graphite (Nippon Carbon) anode and $\text{LiNi}_{0.6}\text{Co}_{0.2}\text{Mn}_{0.2}\text{O}_2$ cathode. The electrolyte was 1 M LiPF_6 in 3:7 (wt%/wt%) ethylene carbonate/ethyl methyl carbonate with a 2% wt addition of vinylene carbonate, and the separator used was Celgard-2325 with a thickness of 25 microns. The N/P ratio for these cells was 1.2 and the theoretical capacity of each cell is 10 Ah. Each cell has the 2-sheet design about which more information can be found in our previous publication by Zhang et al. [13].

5.3.2 Experimental Set-up

The working principles of the SHLB are not discussed in this publication as they can be found in detail in [11]. Figures 5-1a and 1b show the schematics of the location of the nickel foils for the external and internal heating strategies, respectively. It can be seen that heat generated externally must flow across the thickness of the cell while heat generated internally is expected to be uniform across the cell thickness.

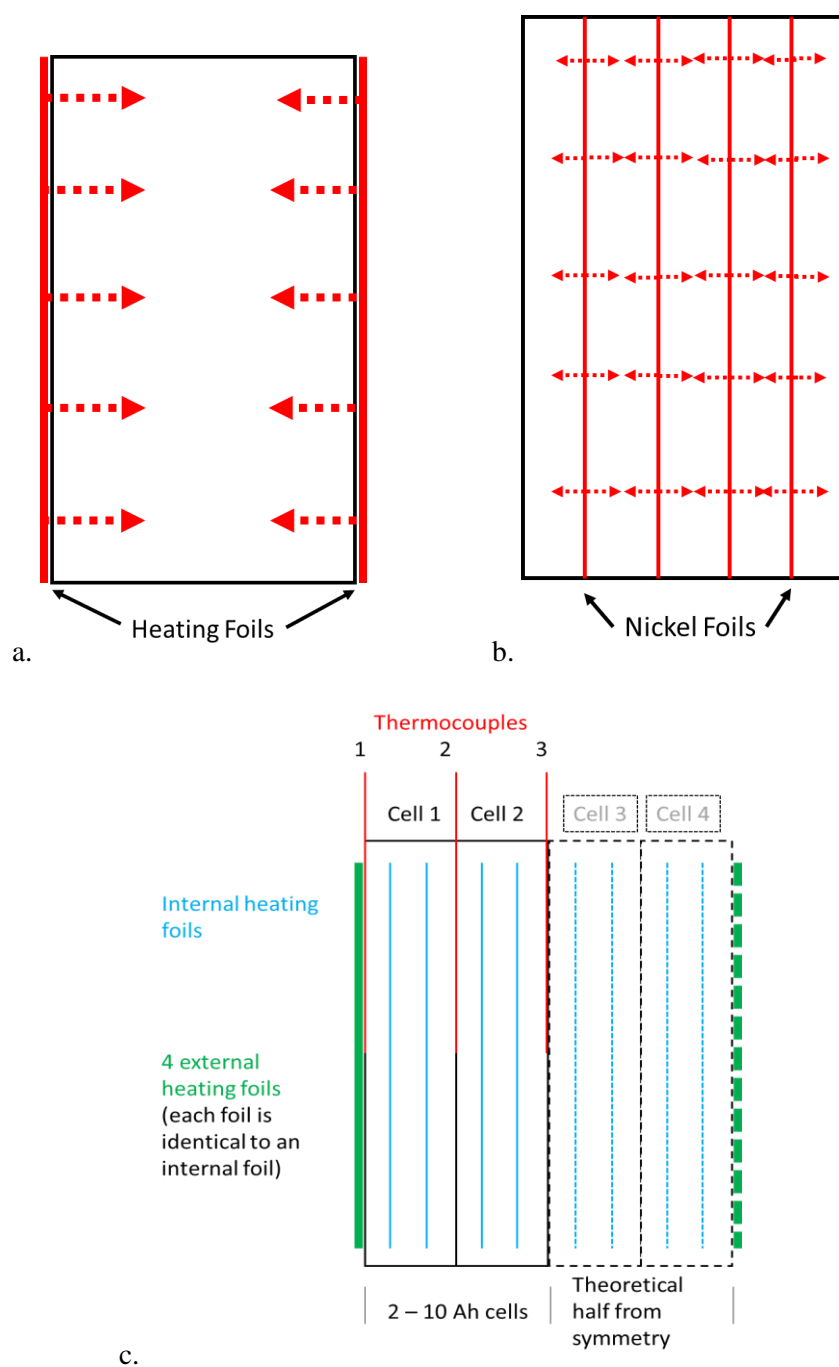


Figure 5-1. Working principle of external and internal heating of a Li-ion battery. (a) Schematic of Ni foil location for external heating (arrows indicate heat flow), (b) Schematic of Ni foil location for internal heating using a self-heating Li-ion battery (arrows indicate heat flow) (c) Schematic of the experimental set-up using two 10 Ah Li-ion cells and symmetry to model a 40 Ah automotive cell.

The schematic of the experimental set-up used can be found in Figure 5-1c. Using symmetry to our aid, a 40 Ah automotive cell is approximated by placing two 10 Ah SHLB cells in parallel with the bottom face of cell 1 touching the top face of cell 2. Cells 3 and 4 are theoretical from the symmetry of a 40 Ah cell, as a reflection of the set-up over the bottom face of cell 2 yields the second half of the 40 Ah cell. T-type thermocouples were placed on the top face of cell 1 (TC 1), in between the two cells (TC 2) and on the bottom face of cell 2 (TC 3). Thermocouples were centered on each face. For our purposes, TC 1 is the surface temperature and will be constrained to a safety cut-off limit and TC 3 is the internal temperature in the middle of the theoretical 40 Ah cell in which a desired temperature after heating will be obtained.

In order to produce the same resistive heating set-up for external heating as the SHLBs, four nickel foils, identical to those inside the SHLB, were placed in parallel on the top face of cell 1 with two tabs available for connecting wires. In between the foils and cell 1 and in between cell 1 and cell 2, a thin layer Omegatherm “201” high thermal conductivity paste was used to ensure uniform contact and efficient heat transfer at these boundaries.

5.3.3 Experimental Testing Protocol

Self-heating tests were performed using an Arbin BT2000 battery tester with temperature controlled by a Tenney T10c environmental chamber. The cell was first fully charged at room temperature and then was cooled to a desired ambient temperature. The ambient temperatures included in this study for both external and internal heating are -10, -20, -30 and -40 °C. To initiate the self-heating process for internal heating, the battery tester was used as the switch between the ACT terminals and positive terminals, setting the voltage to 0 V. To perform external heating, one tab from the external foils was connected to the negative terminals of the cells via an external wire. The other tab on the foils then became the new ACT terminal and the

same self-heating test protocol was followed as stated above. Tests were concluded when either the cell internal temperature (TC 3) reached 0 °C or when the surface temperature (TC 1) reached the safety cut-off limit of 70 °C. In order to measure the amount of current produced by each cell, a high current shunt resistor (Ohmite) was placed before the positive terminal for cell 1 and cell 2. The battery tester monitored overall cell voltage and current, though for detailed analysis of internal heating, voltages across each foil and each cell were obtained during and after each self-heating. For external heating, voltages across the external foils and each cell were obtained as well as using a high-frequency resistance measurement across each internal foil, as it is not possible to have current flow through these foils with this set-up.

5.4 Results and Discussion

Figures 5-2a-d show the temperature profiles from the external heating experiments from -10, -20, -30 and -40 °C, respectively. The results from the internal heating using the SHLB are shown in Figures 5-2e-h. It can be seen that for all temperatures, the external heating strategy failed to heat the entire cell sufficiently before the safety surface temperature limit was reached ($TC\ 1 > 70\ ^\circ C$). Moreover, the external heating failed to even heat one of the cells completely as can be seen in the fact that TC 2 never reached the target temperature of 0 °C, even after the heating current is shut off and the cell is allowed to reach thermal equilibrium. In contrast, the internal heating strategy was able to successfully heat the entire cell at all temperatures. It can also be seen that the heating was very uniform with minimal overshoot at the boundary of the two cells. This overshoot increases as the temperature decreases, reaching a maximum of only 7 °C for the heating from -40 °C, well below the safety temperature limit.

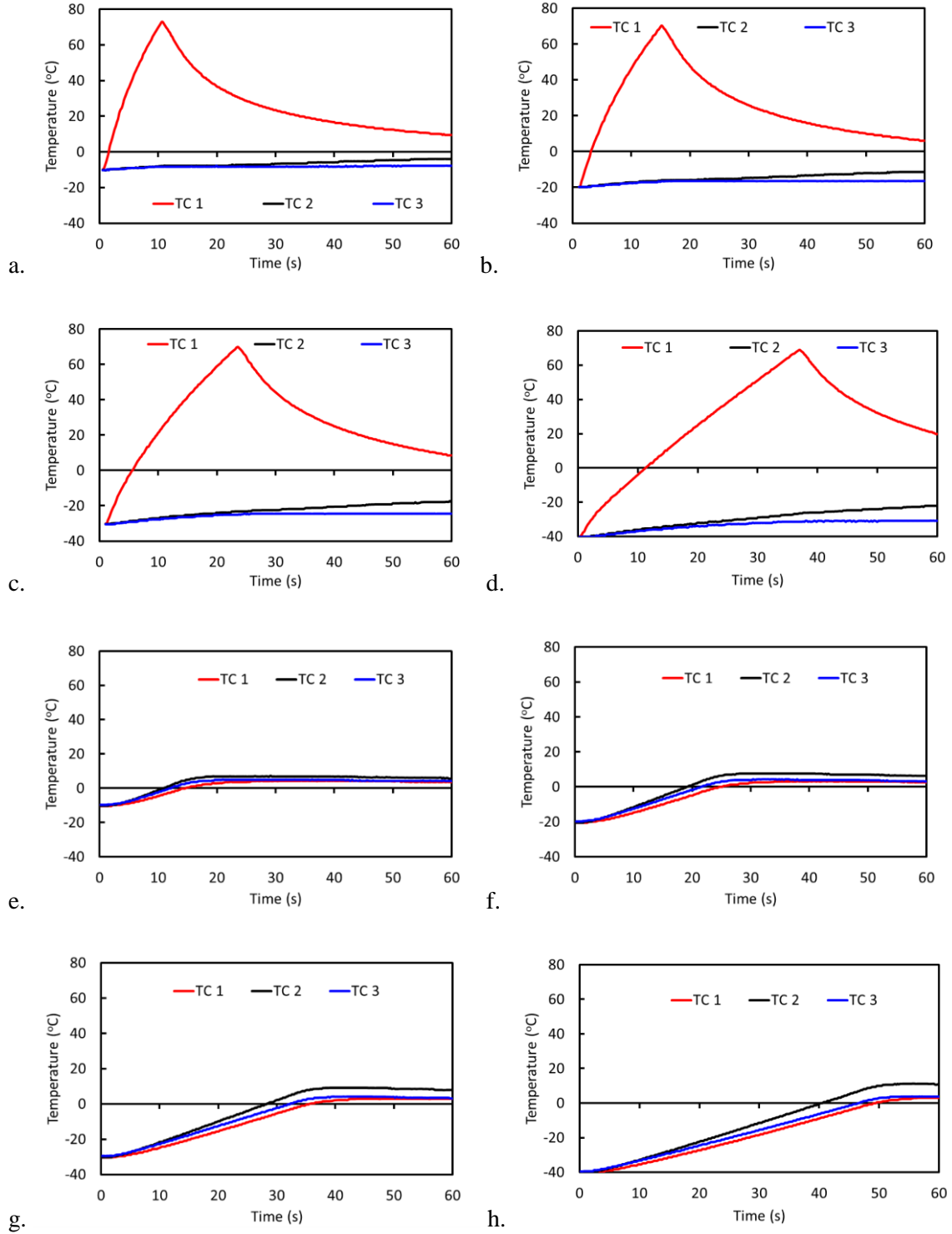
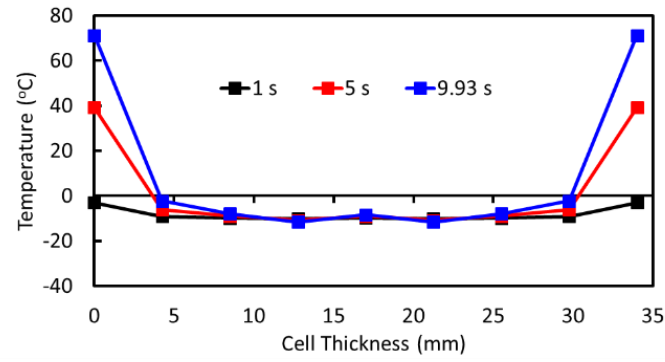


Figure 5-2. Temperature evolution using thermocouples during heating for external heating from (a) -10 °C, (b) -20 °C, (c) -30 °C (d) -40 °C and internal heating from (e) -10 °C, (f) -20 °C, (g) -30 °C (h) -40 °C.

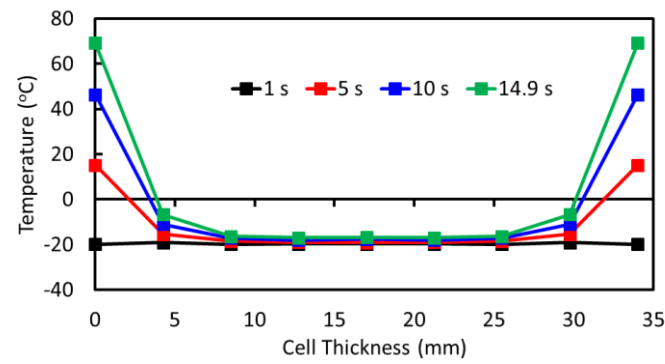
Figures 5-3a-h shows the spatial temperature distribution for each of the previous cases, now using the internal foils as temperature sensors in the external heating cases. Figures 5-3a-d clearly show that external heating produces large temperature gradients across the entire cell, which can lead to accelerated degradation to the cell. The surface temperature for all external heating cases increased rapidly until the safety limit was reached, leaving the cell with a highly non-uniform temperature distribution. The U-shapes of these distributions match well to the expected modeling results predicted by Yang *et al.* [14] where there is a thin layer near the surface that reaches the desired temperature while the rest of the cell remains well below this level. Figures 5-3e-h again show uniform heating if using the internal strategy. In each case there is minimal temperature gradient across the cell and the surface temperature is the minimum value due to heat transfer to the sub-zero ambient environment.

A summary of the previous two figures is shown in Figure 5-4a. Here the temperatures at the end of heating are shown for each of the thermocouples for both heating strategies at each ambient temperature. This shows very clearly how for internal heating was successful at heating the entire cell to the desired temperature at the end of heating, while external heating was not only unsuccessful at this feat, but also caused temperature gradients in excess of 70 °C across the outer half of the cell.

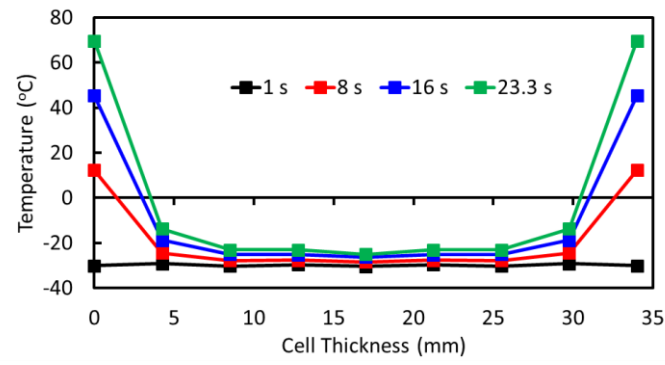
Internal heating was not only successful at heating the cell, but was effective and efficient at the same time, in terms of heating time and energy consumed, respectively, as shown in Figure 5-4b. Heating times were 12.3, 21.5, 32.3 and 46.8 s for internal heating from -10, -20, -30 and -40 °C, respectively. The total capacity used was also low, ranging from 2.3% at -10 °C to only 6.9% at -40 °C.



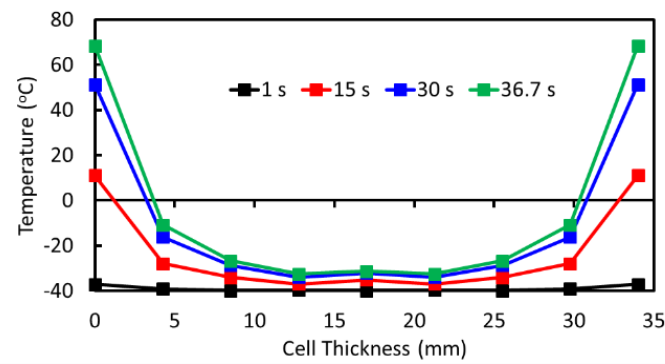
a.



b.



c.



d.

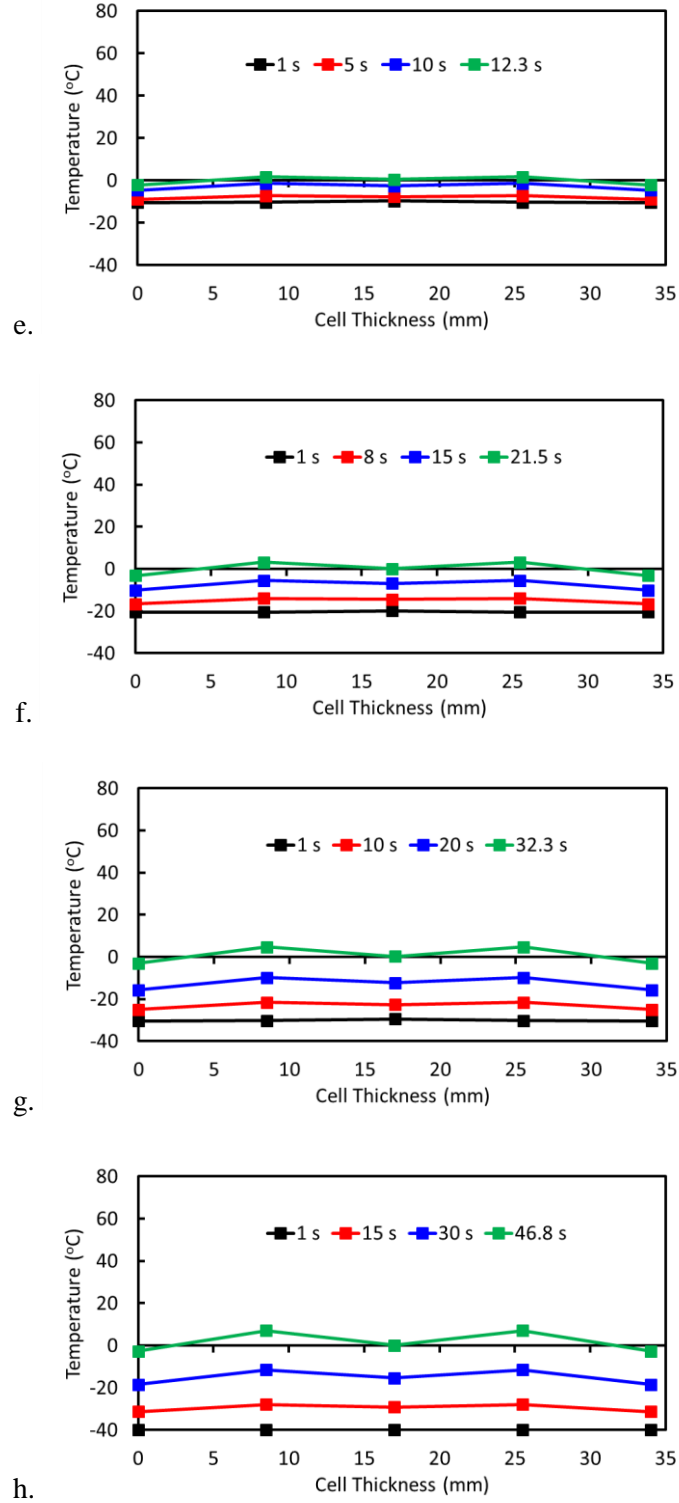


Figure 5-3. Spatial temperature evolution during external heating from (a) -10°C , (b) -20°C , (c) -30°C and (d) -40°C and internal heating from (e) -10°C , (f) -20°C , (g) -30°C and (h) -40°C .

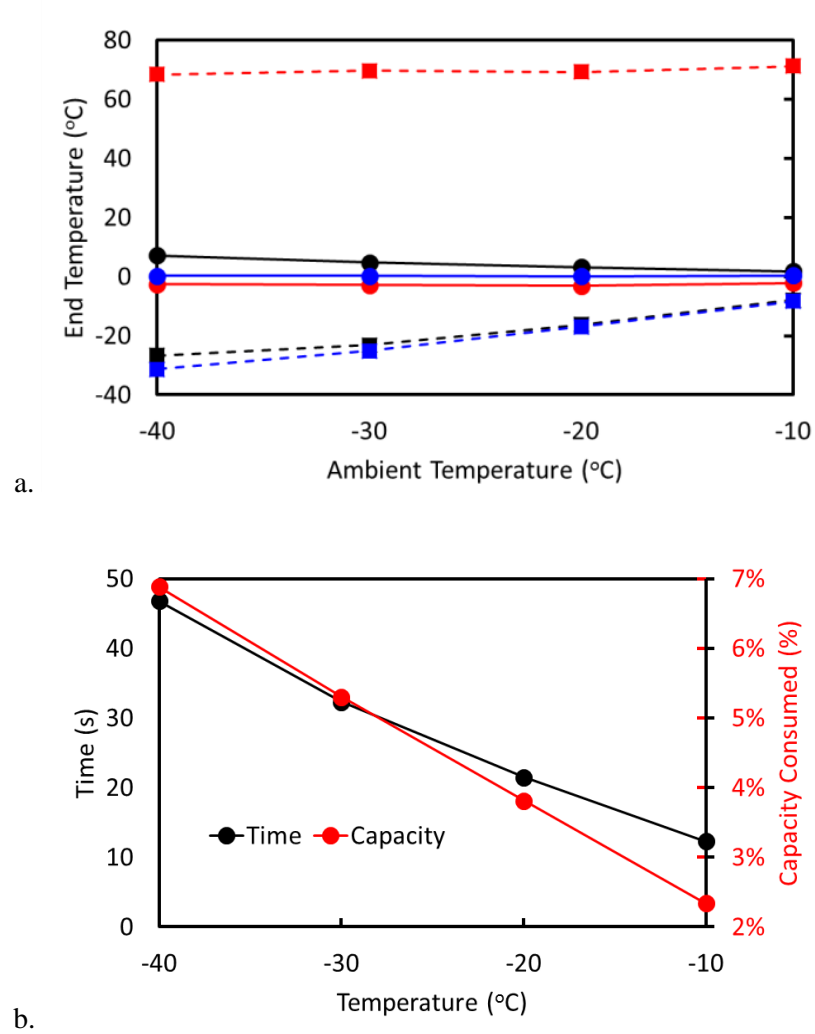


Figure 5-4. . Effect of ambient temperature on (a) Temperatures at the end of heating for TC1 (red), TC2 (black) and TC3 (blue) for external (square data points) and internal (circle data points) heating and (b) Heating time and percentage of capacity consumed (in red).

Looking further into why external heating did not work while internal did work leads to examining the current produced from each of the two 10 Ah cells during the heating process, shown in Figures 5-5a-h. In all cases, the internal heating produced a higher total cell current than external heating. At each temperature, the initial currents from the two strategies are similar, though as heating progress, the difference between the two becomes more pronounced. This difference can be seen when looking at the currents from each of the individual cells (Figures 5-5b, d, f and h). Internal heating produces a uniform current from cell 1 and cell 2. However, for external heating it can be seen that while cell 1 produces a current nearly identical to internal heating, cell 2 current drops off drastically, indicating a large current gradient across the cell. This explains the large temperature gradient seen in Figures 5-2, 5-3 and 5-4, as ohmic (I^2R) heating will cause cell 1 to have a larger temperature increase than cell 2.

To examine the cause of this current gradient across the cell, cell and foil resistances need to be determined. In order to do this, one needs to first examine the voltage of the cells during the heating process, as seen in Figure 5-6. While cell voltages for both heating strategies are nearly identical at each temperature, it can be seen that a lower ambient temperature causes a drastic decrease in the overall cell voltage. For each temperature, the open circuit voltage was estimated as a linear line between initial equilibrium voltage and final equilibrium voltage, which is necessary to calculate heating power and internal cell resistance.

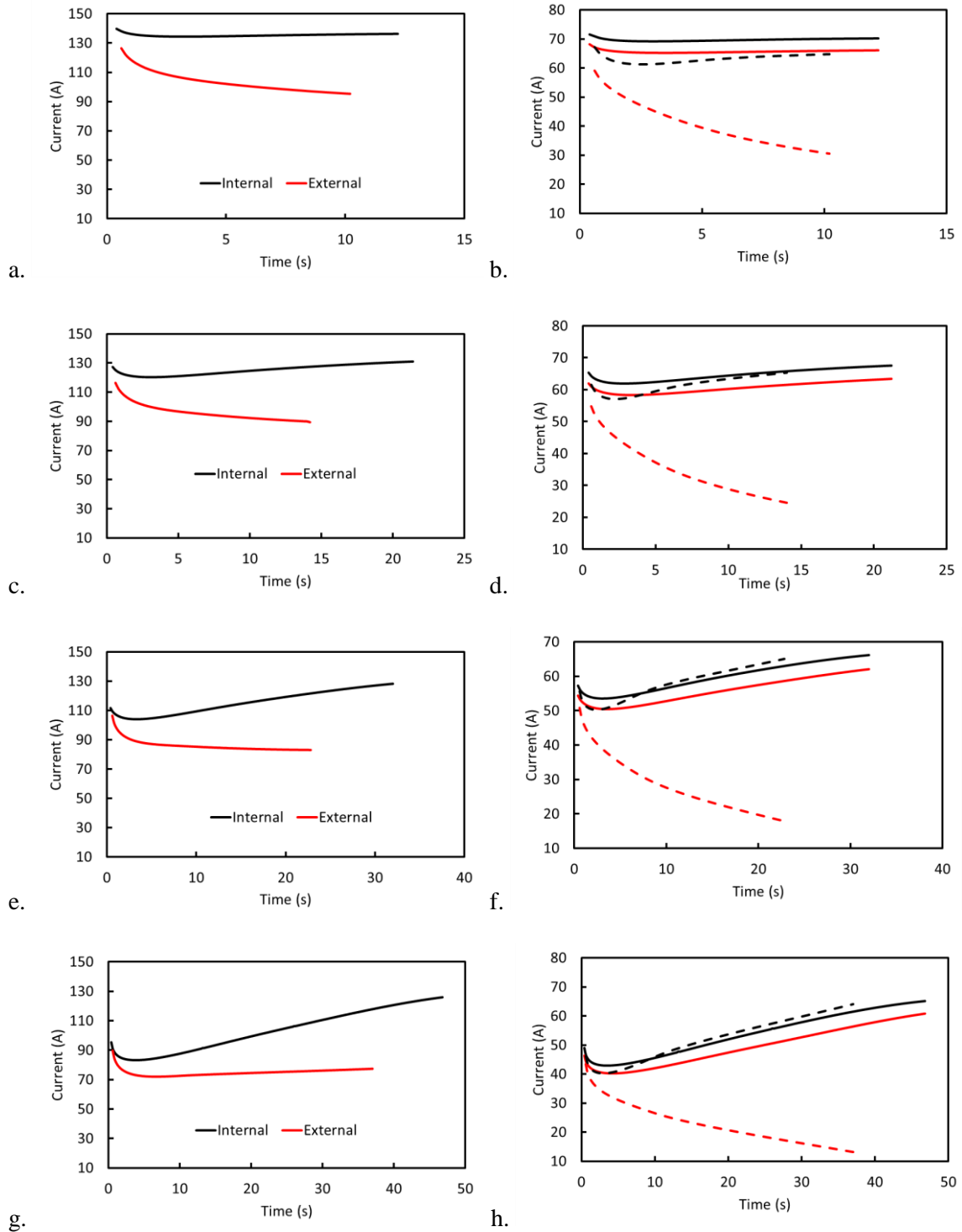


Figure 5-5. Activation current during heating for (a) -10 °C, (c) -20 °C, (e) -30 °C and (g) -40 °C and individual cell activation currents(internal heating in black, external heating in red, cell 1 solid line, cell 2 dashed line) for (b) -10 °C, (d) -20 °C, (f) -30 °C and (h) -40 °C.

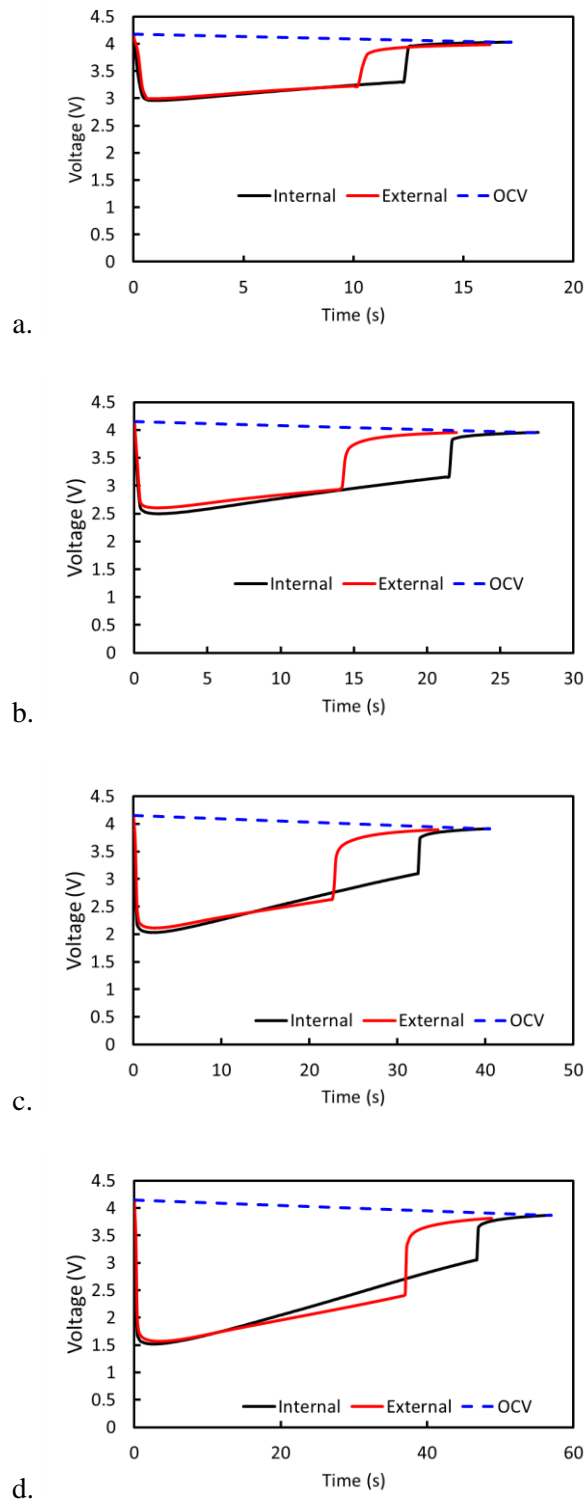


Figure 5-6. Measured cell voltage (V_{cell}) and estimated open circuit voltage (V_{oc}) for heating from (a) $-10\text{ }^{\circ}\text{C}$ and (b) $-40\text{ }^{\circ}\text{C}$.

Ohmic heating power from the nickel foil can be calculated by $V_{\text{cell}} * I_i$, where $I = 1, 2$, or t for current from cell 1, cell 2 or total current. The electrochemical reaction's contribution to heating power can be calculated using $(V_{\text{oc}} - V_{\text{cell}}) * I_i$, where V_{oc} is the open circuit voltage estimated in Figure 5-6. At -10 and -20 °C, the foils produce a majority of the heating power for both internal and external heating, as seen in Figures 5-7a-d. For internal heating at -10 °C, each foil provides 35% increasing to 40% of the heating power (70% increasing to 80% in total), while the reaction heating in each cell is uniform and decreases by the end of heating. External foils provide a similar percentage of heating power as in the internal heating, 71% increasing to 79%, however the actual heating power provided by the external foils is about 75 W less than the internal foils at the beginning of heating and increases to about 150 W differences at the end of heating. It can be seen that the electrochemical reaction in each cell starts off nearly identical, though for external heating, cell 2's reaction heating power drops to about half of cell 1's by the end of the heating process, which is due to the lower current produced by cell 2 as seen above.

At -40 °C, a different trend is seen for internal heating as seen in Figure 5-7g. For the first 19 seconds, the electrochemical reaction produces more heat than the nickel foils. Initially, the foils only provide 40% of the heating power overall, but that nearly doubles to 79% by the end of heating. This is attributed to the fact that both the current through and resistance of the metal foil increase with temperature, while the internal cell resistance drops with increasing temperature due to improved transport properties and reaction kinetics [9, 15, 16]. For external heating at this temperature, Figure 5-7h shows the foil provides 38% of the heating power initially and increases to 60% at the end of heating. For this case, it is interesting to look at how each cell's reaction heating power evolves. For cell 1, there is a slight increase in heating power followed by a slight decrease. This is attributed to the fact that initially the current increases drastically but as the cell heats up, the decrease in internal cell resistance causes the power to

decrease through the end of heating. Cell 2 shows a constant decrease in heating power for the duration of the heating process, which is due to the current decreasing and minimal decrease in cell resistance due to heating. At the end of heating, cell 1 is producing nearly 5 times more heat than cell 2.

To verify the previous results, foil and cell reaction resistances are determined for all cases as seen in Figures 5-8a-h. The nickel foil resistance increases in the same manner as the temperature evolves, which is expected because the resistance of nickel is linearly proportional to temperature. For the internal heating cases, cell reaction resistances decrease over the duration of the heating, confirming the conclusion seen from the heating power data, that is, as the cells heat up, a decrease in internal cell resistance decreases the heating power obtained from the reaction. For the -40°C internal heating case, the foil resistance becomes larger than the cell internal resistance at 19 seconds, which is when the heating power from the foil begins to dominate as seen above.

Again, for external heating the individual cell resistances are noteworthy. In both cases an obvious resistance gradient is present across the entire cell as the resistance in cell 2 increases while the resistance in cell 1 decreases as heating progresses. This explains the current gradients seen above as both cells are at the same voltage, the evolution of the resistance will drive the evolution of the current. This creates a positive feedback loop which leads to external heating being unsuccessful. External heating failed due to large temperature gradients found in the cell causing the safety temperature limit to be reached before the cell is completely heated. These temperature gradients are due to current gradients across the cell which in turn are caused by large internal resistance differences across the cell. However, the internal resistance is dependent upon the temperature of the cell. Thus, as the heating progresses, the gradients for each variable increases until the shutoff limit. For internal heating, the lack of these gradients across the cell allow for cell to be completely heated without reaching any safety concerns.

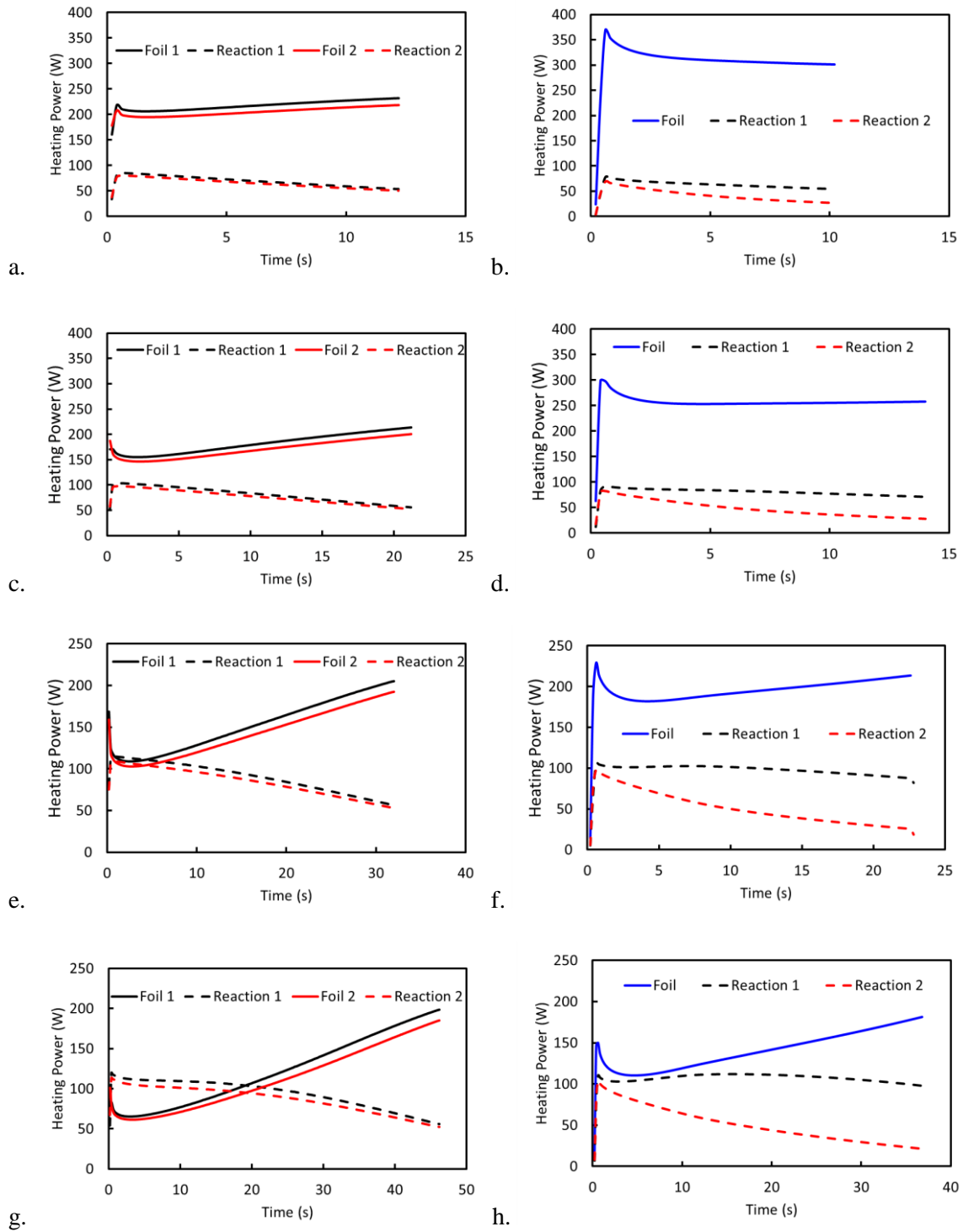


Figure 5-7. Breakdown of heating power from the nickel foil and electrochemical reactions during internal heating from (a) -10 °C, (c) -20 °C, (e) -30 °C and (g) -40 °C and external heating from (b) -10 °C, (d) -20 °C, (f) -30 °C and (h) -40 °C.

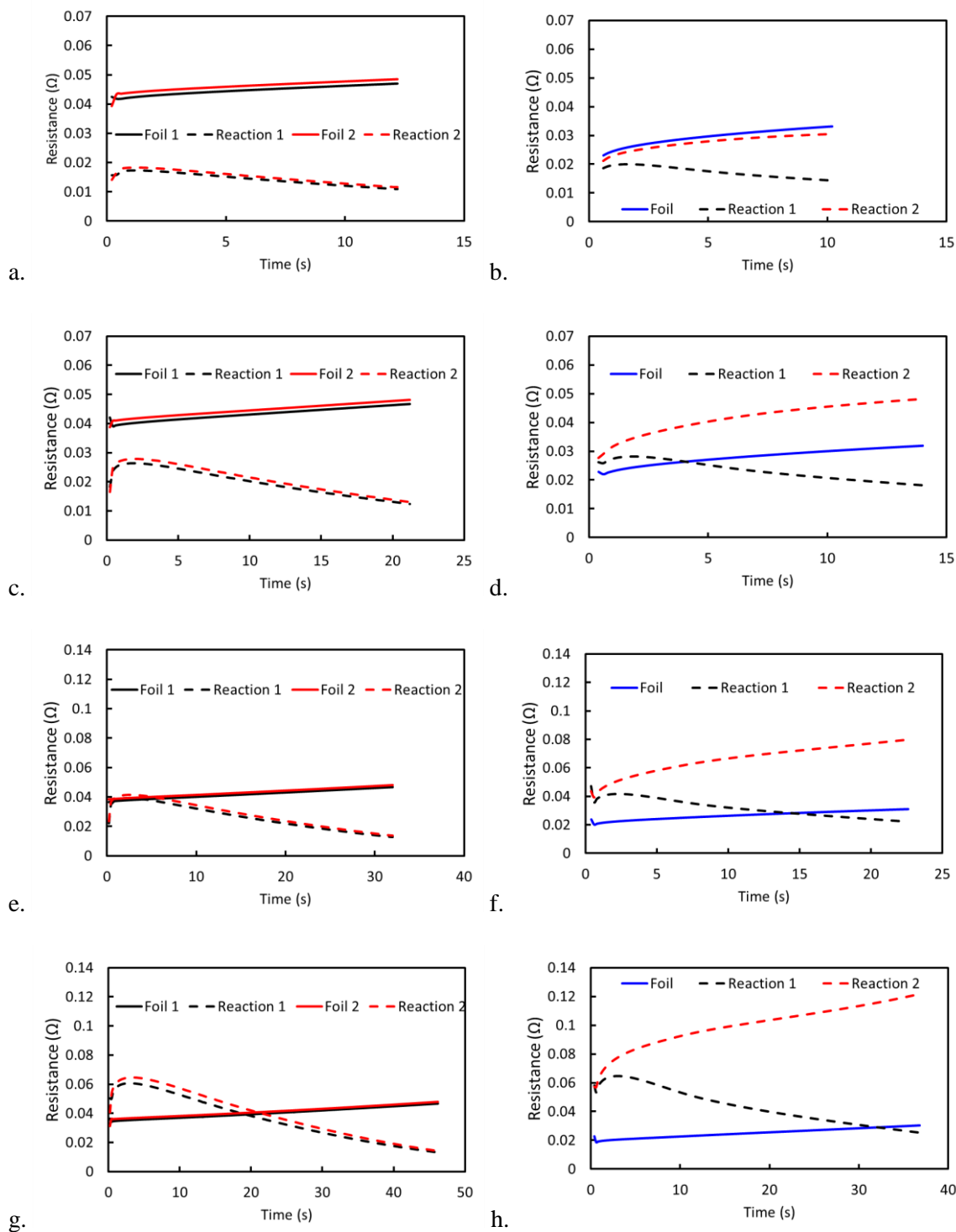


Figure 5-8. Breakdown of resistance from the nickel foil and electrochemical reactions during internal heating from (a) -10 °C, (c) -20 °C, (e) -30 °C and (g) -40 °C and external heating from (b) -10 °C, (d) -20 °C, (f) -30 °C and (h) -40 °C.

5.5 Conclusions

Two different heating strategies for large-format automotive Li-ion batteries were examined: internal heating using the recently developed SHLB technology and external heating using the same number of foils as the internal heating placed on one surface of the cell set-up. It was found that external heating failed to completely heat the cell to 0 °C from ambient temperatures of -10, -20, -30 and -40 °C; while internal heating was not only successful, but did so in an efficient and effective manner in terms of energy consumption and heating time. Heating times ranged from 12.3 to 46.8 seconds and capacity consumed ranged from 2.3% to 6.9% from -10 to -40 °C, respectively. Internal heating provided uniform heating across the cell, while external heating showed large temperature, current and resistance gradients across the cell. These gradients were intensified by a positive feedback loop created in which large temperature gradients are caused by large current gradients which are caused by large resistance gradients which are caused by temperature gradients. These gradients can cause degradation issues as well as safety concerns, as the surface temperature reached the safety limit in which the tests were ended.

5.6 References

1. Kang, K.S., et al., *Electrodes with high power and high capacity for rechargeable lithium batteries*. Science, 2006. **311**(5763): p. 977-980.
2. Armand, M. and J.M. Tarascon, *Building better batteries*. Nature, 2008. **451**(7179): p. 652-657.
3. Smith, A.J., et al., *Precision Measurements of the Coulombic Efficiency of Lithium-Ion Batteries and of Electrode Materials for Lithium-Ion Batteries*. Journal of the Electrochemical Society, 2010. **157**(2): p. A196-A202.

4. Waldmann, T., et al., *Interplay of Operational Parameters on Lithium Deposition in Lithium-Ion Cells: Systematic Measurements with Reconstructed 3-Electrode Pouch Full Cells*. Journal of the Electrochemical Society, 2016. **163**(7): p. A1232-A1238.
5. Ein-Eli, Y.T., S.R.; Chadha, R.; Blakley, T.J.; Koch, V.R., *Li-Ion Battery Electrolyte Formulated for Low-Temperature Applications*. Journal of the Electrochemical Society, 1997. **144**: p. 823-829.
6. Zhang, J.B., et al., *Simultaneous estimation of thermal parameters for large-format laminated lithium-ion batteries*. Journal of Power Sources, 2014. **259**: p. 106-116.
7. Zhang, S.S., K. Xu, and T.R. Jow, *The low temperature performance of Li-ion batteries*. Journal of Power Sources, 2003. **115**(1): p. 137-140.
8. Zhang, S.S., K. Xu, and T.R. Jow, *Low temperature performance of graphite electrode in Li-ion cells*. Electrochimica Acta, 2002. **48**(3): p. 241-246.
9. Ji, Y., Y.C. Zhang, and C.Y. Wang, *Li-Ion Cell Operation at Low Temperatures*. Journal of the Electrochemical Society, 2013. **160**(4): p. A636-A649.
10. Ji, Y. and C.Y. Wang, *Heating strategies for Li-ion batteries operated from subzero temperatures*. Electrochimica Acta, 2013. **107**: p. 664-674.
11. Wang, C.Y., et al., *Lithium-ion battery structure that self-heats at low temperatures*. Nature, 2016. **529**(7587): p. 515-8.
12. Wang, C.Y., et al., *A Fast Rechargeable Lithium-Ion Battery at Subfreezing Temperatures*. Journal of the Electrochemical Society, 2016. **163**(9): p. A1944-A1950.
13. Zhang, G.S., et al., *Rapid self-heating and internal temperature sensing of lithium-ion batteries at low temperatures*. Electrochimica Acta, 2016. **218**: p. 149-155.
14. Yang, X.G., T. Liu, and C.Y. Wang, *Innovative heating of large-size automotive Li-ion cells*. Journal of Power Sources, 2017. **342**: p. 598-604.
15. Senyshyn, A., et al., *Low-temperature performance of Li-ion batteries: The behavior of lithiated graphite*. Journal of Power Sources, 2015. **282**: p. 235-240.
16. Zhang, S.S., K. Xu, and T.R. Jow, *Electrochemical impedance study on the low temperature of Li-ion batteries*. Electrochimica Acta, 2004. **49**(7): p. 1057-1061.

Chapter 6

Conclusions and Future Work

6.1 Conclusions

Lithium-ion batteries have the potential to be utilized as the next generation energy source in the ever-growing and highly demanded electric vehicle application. In order for this to occur, the issues that are prohibiting this must be confronted. These issues include cost, reliability, cycle life, low temperature performance and fast charging capabilities. This dissertation looks at examining two of these issues, namely cycle life and low temperature performance.

In chapter 2, capacity and power fade during cycle-life testing at room temperature were examined for high energy lithium-ion pouch cells with thick NMC622 cathodes and thick graphite anodes. In order to perform cycle-life testing, an aging protocol was developed along with performance characterization tests and EIS tests. Included in this work was the development of a novel three-electrode set-up utilizing a lithium metal reference electrode. The set-up was then calibrated to ensure that the data obtained from this new set-up was unchanged from the same tests using the standard two-electrode set-up. Once this was confirmed to be the case, the three-electrode set-up was used to determine the contributions from each electrode to aging utilizing the same characterization and EIS tests.

From the cycle-life testing, it was determined that these high energy cells were able to last ~1400 cycles when using an end-of-life criterion of 75% capacity retention. The cells experience significant capacity and power fade upon aging. The power fade of the cell is mainly due to degradation of the positive electrode including the growth of surface film on the positive

electrode active materials and the increase in charge-transfer resistance. A number of factors may contribute to the capacity fade including the loss of cyclable lithium due to the growth of SEI layer, loss of active electrode materials and lithium plating.

In order to further improve cycle life of high energy NMC622/graphite lithium-ion batteries, it is necessary to avoid lithium plating and prevent rapid growth of SEI layer on graphite anode. In order to better understand this degradation phenomenon, a better understanding of lithium plating needed to be obtained, as discussed in Chapter 3. Here, the high energy cells from Chapter 2 and other high power cells were designed, built and tested utilizing the previous aging protocol. The high energy cells were designed with an average capacity of 3.3 Ah and the high power cells were designed with an average capacity of 2.7 Ah with each possessing an N/P ratio of 1.2, standard for the industry.

In order to better understand the lithium plating mechanism, research-type cells were designed and built to accelerate lithium deposition on the graphite anode using the same electrode materials as the baseline cells, but with an N/P ratio of 0.6. The research cells were cycled at 70% of the theoretical cathode capacity at 5, 15, or 35 °C in order to not induce a safety issue with extreme overcharging. The results of the forced lithium plating study show that for all cells, lithium plating was present as seen in the upper voltage plateau at the beginning of discharge and by the significantly lower coulombic efficiencies over the first 5 cycles. A 0.15 V drop in cell potential during discharge was noticed for all cells, which is believed to be the transition point from lithium stripping to lithium deintercalation from the graphite structure. For the cells cycled at 35 °C, the total capacity was 3.7 Ah and the width of the voltage plateau was ~0.9 Ah, indicating about 2.8 Ah coming from lithium in the graphite. This is the expected capacity of the anode with a theoretical capacity of 3.0 Ah. The cells cycled at 15 and 35 °C each exhibited some level of conversion from metallic lithium to SEI by reaction with the electrolyte. This new and thick SEI layer was able to protect the cell surface from further plating and thus extended the

cycle life of the cell, although there was a large initial drop in cell capacity over the first few cycles. Finally, cycle life shows that cells cycled at 5 °C last no more than 5 cycles. In comparison, cells at 15 °C lasted 4-12X longer and cells at 35 °C lasted over 25X longer, indicating that temperature is an important variable to control in the attempt to mitigate lithium plating.

If the temperature of the cell could be monitored and controlled during the charging process, then lithium plating could potentially be mitigated. Controlling the ambient temperature of the cell may be practical in a laboratory or indoor environment, but this is not practical for use in electric vehicles. A more practical method is to control the interior of the cell by heating the cell prior to use. Previous efforts by our group have produced a viable way to internally heat an All-Climate Battery from sub-zero temperatures using a continuous heating current in which acceptable internal cell temperatures are achieved quickly and with little energy consumed.

Pulse heating of an all-climate battery was examined in Chapter 4 in order to minimize spatial temperature gradients, average activation current, and energy consumed when compared to the current heating protocol of continuous heating. Pulsing protocols consisted of an activation pulse of 1 or 2 seconds followed by a rest pulse of 1, 2, 3, or 4 seconds for heating a cell from 0 °C to 20 °C. The continuous heating showed a maximum foil temperature of 50 °C, comparing to the highest pulse heating of 42 °C. This leads to the maximum temperature gradient (foil to surface) for continuous heating to be 30 °C while the highest of any pulse heating was less than 24 °C. Not only was the spatial temperature gradient lowered by pulse heating, but so was the surface temperature overshoot, meaning continuous heating of the cell leads to wasted energy used to heat the cell above the target temperature.

The optimal pulse heating protocol is 2 seconds activations followed by 2 seconds rest. The optimal rest time was determined by looking at the maximum foil temperature, maximum

temperature gradient, and total energy consumed. The activation time was determined by minimizing the increase in heating time due to the lowering of the average activation current.

Until now, the cells we have examined have been on the laboratory scale and not the industrial electric vehicle scale. Mitigating lithium plating on this large scale is of extreme interest because automotive manufacturers are looking for ways to improve the energy density of their cells while also extending the life of their cells, leading to more attractive warranty options for consumers. In order to achieve this goal, the temperature of the battery pack in the vehicle must be able to be manipulated.

Until this point, the current practice for heating industrial scale batteries is to utilize external heaters to heat the cell from the outside-in. This method can work for small-format cells, but will run into issues of temperature gradients, slow heating times, and possible non-uniform degradation across the thickness of a large-format cell. Two different heating strategies for large-format automotive Li-ion batteries were examined in Chapter 5: internal heating using the recently developed SHLB technology and external heating using the same number of foils as the internal heating placed on one surface of the cell set-up. It was found that external heating failed to completely heat the cell to 0 °C from ambient temperatures of -10, -20, -30 and -40 °C; while internal heating was not only successful, but did so in an efficient and effective manner in terms of energy consumption and heating time. Heating times ranged from 12.3 to 46.8 seconds and capacity consumed ranged from 2.3% to 6.9% from -10 to -40 °C, respectively. Internal heating provided uniform heating across the cell, while external heating showed large temperature, current and resistance gradients across the cell. These gradients were intensified by a positive feedback loop created in which large temperature gradients are caused by large current gradients which are caused by large resistance gradients which are caused by temperature gradients. These gradients can cause degradation issues as well as safety concerns, as the surface temperature reached the safety limit in which the tests were ended. The result of this work suggests that

internal heating using the SHLB technology is a viable way to mitigate the potential threat of lithium plating in lithium-ion batteries, thus vastly expanding the range of ambient temperatures in which operation of an electric vehicle can be accomplished without the fear of range anxiety.

6.2 Future Work

6.2.1 Further Diagnostic Studies for Understanding Lithium Plating

In order to better understand the variables that control lithium plating, more diagnostic studies need to be performed. To start, more Res cells need to be cycled at the aforementioned temperatures in order to acquire more data points for the study. Right now, we only have fresh and end-of-life cells in which to perform diagnostics, though it is imperative that we obtain cells that are only partially aged, in order to determine if there is some intermediate state of lithium plating that may be detectable. Currently, two-electrode EIS has only been performed on fresh and aged baseline cells and fresh Res cells. Once we obtain more aged Res cells, we can perform EIS on them to obtain a resistance evolution for these cells. It may also be possible to perform a mechanistic study and model the EIS data as an equivalent circuit, and thus determine a breakdown of the overall cell resistance into resistances like charge-transfer, ohmic, and surface film.

Using the previously developed three-electrode setup, a calibration needs to be performed for both fresh and aged Res cells. This calibration will include the rate capability tests, the temperature dependent tests, and EIS. We will determine if the data obtained for a specific cell from the three-electrode setup matches the previously obtained two-electrode data. Once the calibration is satisfied, we can then obtain an anode potential evolution using the three-electrode setup. Because lithium plating is preferential when the anode potential drops below 0 V Li/Li^+ ,

determining how the anode potential evolves with aging will give us better insight into the effect of lithium plating.

Another diagnostic tool available is to create coin half-cells using fresh and aged electrode materials from both the baseline and Res cells. The pouch cells will be disassembled in a glove box and the stacks separated. Coin cells sized discs will be punched from select sheets and placed in a coin cell with a lithium metal counter electrode. Using this method will allow us to determine the exact capacity of the fresh and aged cathode and anode materials since the lithium metal will provide an excess of lithium.

6.2.2 Mitigating Lithium Deposition

As shown in the self-heating cells previously developed by our group, it is possible to heat lithium ion batteries in a relatively short time with minimal capacity consumed to improve performance at sub-zero ambient temperatures. Studies so far have only been performed at sub-zero temperature, though we have shown that lithium plating can occur at temperatures near, yet above 0 °C. If we can show that using the self-heating battery technology allows us to effectively and efficiently produce 25-30 °C cycle life data in a low temperature environment, even for a worst-case scenario as is such with our research cells designed to accelerate lithium deposition, then lithium ion batteries would be that much more useful in electric vehicle, space, and robotic applications. We would design new research cells with the same cathode and anode design as before, but this time with self-heating elements distributed throughout the cell to promote uniform and efficient heating. These cells would then be cycled at various temperatures, ranging from -10 °C to 35 °C, with cycling occurring only after the cell surface temperature has reached a specified value.

Similarly, because excess anode material is added to protect against lithium plating when charging at temperatures below room temperature, cells could be constructed with a lower N/P ratio, perhaps in the 1.05-1.1 range. Some cells would contain the self-heating technology and some cell would be baseline batteries. This decrease in excess anode material would allow for an increase in energy density. Both types of batteries would then undergo aging tests at varying temperatures, utilizing the self-heating technology to maintain an internal temperature of 20-30 °C and comparing the cycle life obtained from each type of cell. The goal of this work would be for the cells with the self-heating technology to have a longer cycle life than those without the technology, showing that self-heating technology is an effective tool to mitigate lithium plating.

VITA
Daniel R. Marple

Education

The Pennsylvania State University, University Park, PA
Doctor of Philosophy in Chemical Engineering, 2017

The Pennsylvania State University, University Park, PA
Bachelor of Science in Chemical Engineering with distinction, 2010
with honors in Chemical Engineering
Bachelor of Science in Mathematics with distinction, 2010

Publications

- Leng, Y., Ge, S., **Marple, D.**, *et al.* Electrochemical Cycle-life Characterization of High Energy Lithium-ion Cells with Thick $\text{Li}(\text{Ni}_{0.6}\text{Mn}_{0.2}\text{Co}_{0.2})\text{O}_2$ and Graphite Electrodes. *J. Electrochem. Soc.* 164 (2017) A1037-1049.
- Marple, D.**, *et al.* Electrochemical Cycle-life Characterization of High Power Lithium-ion Cells with Thin $\text{Li}(\text{Ni}_{0.6}\text{Mn}_{0.2}\text{Co}_{0.2})\text{O}_2$ Electrodes. – in draft
- Marple, D.**, *et al.* Pulse Self-Heating of Self-Heating Lithium-ion Battery – submitted for publication, *J. of Power Sources*
- Marple, D.**, *et al.* External vs. Internal Heating for Large-format Automotive Li-ion Batteries – submitted for publication, *J. of Power Sources*
- Zhang, G., Ge, S., Yang, X-G., **Marple, D.** *et al.* Rapid Restoration of Electric Vehicle Battery Performance While Driving at Cold Temperatures – submitted for publication, *J. of Power Sources*
- Zhang, G., Tian, H., Ge, S., **Marple, D.**, *et al.* Visualization of a Li-ion Battery Self-heating by Infrared Thermography – submitted for publication, *J. of Power Sources*